

1. Title: Fabrication of layer-by-layer assembly-based 2D carbon backbone decorated surface plasmon resonance biosensor for label-free prognosis of Alzheimer's disease

2. Introduction

Alzheimer's disease (AD) is a long-term, severe, irreversible, and progressing neurodegenerative health concern [1]. Since its inception, there is a tremendous demand for sensitive and specific assessment of biomarkers of particular ailments to reach an earlier diagnosis [2]. Therefore, numerous strategies for the prognosis and diagnosis of AD have been presented to date [3]. Herein, several AD biomarkers have been documented for diagnosis of AD in clinical samples mainly beta-amyloid ($A\beta$), tau protein, β -Site amyloid precursor protein-cleaving enzyme 1 (BACE1), etc [1]. In recent times, it has been detected using fluorescence-based biosensors [4], electrochemical biosensors [5], quantitative proteomics [6], enzyme-linked immunosorbent assay (ELISA)[5], etc. Notwithstanding these reports on BACE-1 and other AD biomarkers, the rapid and direct assessment of AD biomarkers in supplied clinical samples at clinically meaningful amounts remains the key rate-restricting hurdle for AD and other neurodegenerative illnesses. Since its inception, the plasmonic biosensor has offered remarkable characteristics as diagnostics for biomarker detection [7]. In the case of plasmonic biosensors, surface plasmon resonance (SPR) is a cutting-edge optical biosensor technique that detects analytes with high speed, higher sensitivity, selectivity, label free, etc. [8]. Importantly, the SPR-based technique permits the label-free identification of extremely minute amounts of a target with great accuracy and efficiency [9]. Unfortunately, to the best of our knowledge reports on the detection of $A\beta$ 1-42, tau protein, and BACE-1 using SPR-based biosensors are less explored.

Graphene-based carbon backbone nanostructures such as 2D non-plasmonic graphene oxide (GO) have been disclosed for the construction of upgraded SPR biosensors. Herein, SPR shifts are made possible by their optical properties [10]. Moreover, it has a large surface area, adequate mechanical strength, great conductivity [11], hydrophilic nature, good stability, biocompatibility [12], etc. Besides, the surface functional groups of GO are advantageous for the immobilization of bioconjugates on their surface [13]. Here, biomolecules can be immobilized on the surface and edges of GO via electrostatic interactions, non-covalent interactions, and covalent bonding [12]. It has been discovered that modifying GO with oxygen functionality into amine-reactive groups permits the customization of bandgap and dielectric constant. Therefore, it provides enhanced SPR characteristics [14]. As a result, we

propose to employ GO nanosheets to decorate a large number of antibodies immobilized metal nanoparticles in an SPR biosensor.

The choice of metal nanoparticles on the top of a gold (Au)-coated sensor chip plays an essential role in strengthening sensor sensitivity [15]. The employment of gold nanoparticles (AuNPs) in SPR biosensor development has been broadly claimed owing to their unique and utmost optical characteristics [16]. Moreover, the successful application of bare metal nanoparticles for the formation of bioconjugates has been reported currently that offers a superior presentation of SPR biosensors such as specificity and sensitivity [10, 16, 17]. The synthesized nanoparticles were mostly unstable and were transformed into aggregates that needed the stabilizer [18]. Overall, the minimal and heterogeneous surface chemical functional groups and stability of AuNPs influence the loading of required bioreceptors, limiting the biosensor's sensitivity and selectivity. In addition, proper immobilization with specific orientation is a critical challenge that influences biosensor performance that needs to be overcome. The utilization of plasmonic materials in SPR-based biosensors releases a fresh avenue for sensitivity improvement. The tunable optical attributes of silver nanoparticles (AgNPs) help to improve the SPR signal [19]. In this connection, AgNPs are indeed becoming included in SPR biosensor diagnostic techniques to fabricate extremely precise and reliable nanosized biosensor frameworks. Moreover, such monitoring devices have been strengthened with the emergence of numerous nanomaterials and associated unique features [10, 20]. Platinum nanoparticles (Pt-NPs) are metal-based plasmonic particles that are non-toxic. As well, it has long-term stability, excellent performance [21], and high reflectivity [15]. These mentioned properties are comparable to other metal nanoparticles such as silver (Ag) and 'Au' nanoparticles. Crucially, platinum-containing complicated dielectric constant provides the dynamic SPR [15]. As a corollary, we anticipate that the inclination for Pt-NPs will surmount the stability issue of metal nanoparticles, such as 'Ag' nanoparticle oxidation [10]. Because of the good optical features of MNPs and the high biomolecule loading capacity of GO, the conjunction of MNPs and GO may open up new possibilities for the construction of SPR biosensors.

The cationic and anionic polymers-based layer-by-layer (LbL) assembly technique gives a homogenous and large number of surface functionality to immobilize bioreceptors with specified orientations. It offers good stability and specific targeting potential [22]. Moreover, the development of LbL assembly on the surface of metal nanoparticles offers boosted electrical conductivity as well as electroactive high surface area [18]. In addition, the LbL assemblies provide the softer attachment of biomolecules on the surface of solid metal

nanoparticles that may offer a specific orientation [23, 24]. Therefore, it resulted in a high binding affinity for interest analyte. Amusingly, it also retains its biological properties, which are beneficial for biosensor performance [24]. The use of chitosan (CS), chitin [25], sodium alginate (SA) [26], etc. has been widely studied in biosensor construction and biomarker detection applications [25]. Here, the preference of 'CS' provides high mechanical stability, locations for biomolecule immobilization, improved conductivity, and sensitivity due to their unique properties such as biocompatibility, surface tunability, and functional groups. As a result, cationic 'CS' has been used to detect glucose, antigens, hydrogen peroxide, and other substances [27]. Similarly, the application of 'SA' in biosensors has received a lot of attention because of its non-toxicity, inexpensiveness, biocompatibility, and chemical modification adaptability [26]. Importantly, because of unique qualities such as biocompatibility and surface modification ability, Poly(allylamine hydrochloride (PAH) is an amino terminated chemical (cationic nature) and Poly (sodium 4 styrene sulphonate (PSS) is an anionic compound that is commonly employed in the creation of LbL assemblies. Furthermore, the usage of PAH and PSS allows for the production of LbL assemblies based only on their electrostatic interaction. As well, the usage of PAH and PSS can provide a softer attachment surface for bioreceptor immobilization on the surface of AuNPs. Therefore, in this work, we aim to coat the exterior layer of the LbL assembly with an amine-terminated polyelectrolyte, which will give a site for the immobilization of a carboxylic terminal having antibodies in a specified direction [18, 28, 29]. In essence, it is essential in biosensor development to assure the bioreceptor's stability and performance. A reliable biosensor must have characteristics such as strong binding between the immobilization surface and the bioreceptors, directed immobilization, high bioreceptor density, minimal non-specific binding, and other desired qualities. To meet these requirements, we plan to design 'CS', PAH, PSS and 'SA' based LbL assemblies on the surface MNPs.

In this work, for the first time, we have employed CS, PAH, PSS, and SA for the design of an LbL assembly-based SPR biosensor. In brief, the LbL nanobioconjugate decorated GO layered affinity Anti-body-LbL@MNPs-GO-SPR biosensor was designed for exceptionally sensitive and selective sensing of AD biomarkers. In this, the CS/PAH coating provides ample amine sites for the immobilization of antibodies, ensuring their orientation in a specific direction. As well, it allows for the formation of a soft attachment surface for the immobilization of the bioreceptor (Anti-body) on the surface of MNPs. Therefore, it facilitated the direct immobilization of bioreceptors whereas avoiding denaturation and maintaining bio-functionality. In addition, the GO nanosheets provided a large surface area

with abundant carboxylic groups for the immobilization of Anti-body-LbL@MNPs. As a result, the synergetic merits of LbL assembly, GO backbone, and MNPs in SPR biosensors provided a low detection limit (LOD), a wide linear range, and clinical practicability for the detection of AD biomarkers. Overall, the CS, PAH, PSS, and SA-coated MNPs bioconjugate decorated with GO-layered SPR biosensors offered highly sensitive, selective, rapid, and label-free detection of AD biomarkers.

3. Objectives

1. To design the Layer-by-Layer (LbL) assembly-based bioconjugate for the fabrication of surface plasmon resonance (SPR) biosensor
2. To develop a bioconjugate decorated graphene oxide nanosheet-based SPR biosensor
3. To provide the highly sensitive and selective SPR-based affinity biosensor for the detection of beta-amyloid
4. To provide the rapid, cost-effective, and label-free recognition of beta-amyloid for the prognosis of Alzheimer's disease

4. Materials and methods

4.1. Materials

Amyloid β protein Fragment $_{1-42}$ (>95 % HPLC, $A\beta_{1-42}$) and monoclonal anti- β -Amyloid ($A\beta$) antibody (Produced in mouse, purified from hybridoma cell culture) were purchased from Sigma Aldrich, St. Louis, USA. Amine modified sensor chip (sensor kit) was purchased from Nicoya Life Sciences, Canada. Graphite flakes (> 99 %) were obtained as a gift sample from Asbury Carbons, New Jersey (NJ), USA. Silver nitrate (99 %) was purchased from Titan Biotech Ltd. Rajasthan, India. Chitosan (CS) was obtained from HiMedia Laboratories Pvt. Ltd. Poly (sodium 4 styrene sulphonate) [PSS, MW:~70,000], bovine serum albumin (>98 %, BSA), N-hydroxysuccinimide (NHS), and 1-[3-(di-methylamino)-propyl]-3-ethyl carbodiimide hydrochloride (EDC) were purchased from Sigma Aldrich, St. Louis, USA. *Terminalia catappa* L. ripe fruit was collected from the local area of Shirpur (Maharashtra). Potassium permanganate (99 %, $KMnO_4$) was purchased from Research Lab Fine Chem Industries, Mumbai, India. Hydrogen peroxide solution (30 % w/v, H_2O_2) was purchased from Loba Chemie Pvt. Ltd. Streptozocin was purchased from EMD Millipore Corp., Billerica MA, USA. Nuclease-free water was obtained by Invitrogen Bioservices India Pvt. Ltd. Double distilled water (HPLC grade) was purchased from Avantor Performance Materials India Limited, Thane, India. Tau-441 human (>95 % SDS-PAGE, recombinant

lyophilized powder, expressed in HEK 293 cells), gold (III) chloride hydrate (HAuCl_4 ·aqueous, 99.995 %), cationic Poly(allylamine hydrochloride (PAH, Avg. MW: 50,000), and anionic Poly (sodium 4 styrene sulphonate) [PSS, MW:~70,000] was procured from Sigma Aldrich, CO., St., Louis, USA. *Colocasia esculenta* stem was collected from the Shirpur area. Recombinant human β -Site amyloid precursor protein-cleaving enzyme 1 (BACE-1 Protein) and BACE-1 rabbit monoclonal antibody (Anti-BACE-1) was purchased from Sino Biological Inc. Beijing, China. Platinum chloride (H_2PtCl_6 , $6\text{H}_2\text{O}$; Pt: 40%) was procured from Research-Lab Fine Chem., Industries Mumbai, India. Sodium alginate (SA, viscosity: min 45 cps) was obtained from Loba Chemie Pvt. Ltd. Mumbai. Leaves of *Terminalia catappa* L. were collected from the local area of Shirpur.

4.2. Methods

4.2.1. Approach I

4.2.1.1. Synthesis of GO via modified Hummers method

In this step, GO was synthesized using a modified Hummers method followed by slight modification [30]. Briefly, H_2SO_4 and H_3PO_4 in the ratio of 54 mL: 6 mL were mixed properly followed by stirring for 15 min using a magnetic stirrer at 200 rpm. Subsequently, 0.45 g of graphite flakes powder was added to the above-prepared mixture with constant stirring. After that, 2.64 g of KMnO_4 was added slowly followed by stirring for up to 6 h until the color of the mixture became dark green. Then, H_2O_2 (1.35 mL) was dropped slowly followed by stirring for 10 min to eliminate the excess KMnO_4 . After completion of the reaction, the obtained mixture was cooled at room temperature. Furthermore, this mixture was purified three times by using hydrochloric acid (HCl) and double distilled water (DDW, 1:3 ratio) and centrifuged using a cold centrifuge at 12,000 rpm (for 30 min at 25 °C). Finally, the obtained product was dried at 55 °C for 24 h. Then, it was subjected to numerous spectral characterizations.

4.2.1.2. One-pot green synthesis of AgNPs

Initially, 100 g of *Terminalia catappa* L. ripe fruit was collected from the local area of Shirpur. Then, the fruit was cleaned using DDW and checked for stuck dirty materials. The outer soft epicarp was decanted and the shell was used for extract preparation. Afterward, the shell was dried at 60 °C, in a hot air oven for 8 h. Then, the 50 g of dried part was then boiled at 60 °C in distilled water for up to 1 h. After that, the extract was cooled at room temperature, and centrifuged at 7000 rpm for 30 min. Next, the supernatant was collected and filtered using a 0.22 μm membrane filter. This purified extract was stored at 24 °C and used for further processing. In brief, the AgNPs were synthesized using a constant volume of

extracts (5 mL) under optimized experimental conditions such as temperature (50 °C), with a 10 mL constant volume of AgNO₃ solution (7 mM). Finally, the formation of deep reddish-brown color was observed after 24 h, which revealed the development of AgNPs. The reaction was monitored by checking the absorbance of the reaction mixture for up to 24 h using UV visible spectroscopy. The obtained green synthesized AgNPs were freeze-dried using a laboratory freeze dryer (Freezone12, Labconco, MO, USA).

4.2.1.3. Characterization of synthesized GO and AgNPs

To validate successful synthesis, the green synthesized GO and AgNPs were examined using multiple spectroscopic techniques. The UV-visible (UV-Vis) spectra of GO and green synthesized AgNPs have been recorded between 800 nm to 400 nm using a UV 1800 spectrophotometer (Shimadzu, Japan). The Attenuated total reflection Fourier-transform infrared spectroscopy (ATR FT-IR, Bruker Alpha II) was preferred to characterize the functional group present in the GO and AgNPs. The particle size analysis, polydispersity index (PDI), and zeta potential of synthesized GO and AgNPs were measured using Nanoplus 3 Particulate System (Micromeritics, USA). After that, elemental analysis of GO and AgNPs was done using energy dispersive spectroscopy using FESEM/EDAX (OXFORD XMX N). Scanning electron microscopy (SEM, JEOL Model JSM - 6390LV) was employed to characterize the morphology. As well, the morphology, size, and electron diffraction pattern (SAED) of the GO and AgNPs were imaged using High-resolution transmission electron microscopy (HR-TEM, Jeol/JEM 2100, and Source: LaB6). Afterward, X-ray photoelectron spectroscopy (XPS) was acquired with a high-performance 0–5 keV Ar⁺ ion gun (physical electronics, IIT Roorkee, India). In Bruker D8 development, Powder X-ray diffraction (PXRD) of synthesized GO and AgNPs was recorded using Bruker D8 Advance (STIC Cochin, India). Raman analysis of GO was done using Horiba (HR800-UV) confocal micro-Raman spectrometer at 532 nm laser.

4.2.1.4. Development of layer-by-layer (LbL) assembly

To design the LbL assembly, an accurately weighed 10 mg/mL of AgNPs solution was prepared using deionized (DI) water. Then, 50 mL of this solution was added to the CS solution (4 mg/mL, cationic polymer). The obtained AgNPs@CS suspension was subjected to sonication for 45 min followed by centrifugation at 20,000 rpm for 30 min for separation of LbL assembled AgNPs (AgNPs-CS) from the remaining positive polyelectrolyte. At last, the supernatant was then discarded and washed timely using DI water to remove any unbound polyelectrolyte. Afterward, AgNPs-CS was dried using freeze-drying and subjected to the zeta potential analysis to confirm the

successful layering of cationic polymer (AgNPs-CS). After the confirmation of surface charge, the dried powder of AgNPs-CS was suspended in the anionic polymer 1 % PSS for 10 min to form a second LbL assembly (AgNPs-CS-PSS). In this step, cold centrifugation and washing were repeated as per the abovementioned process to eliminate the unbound anionic polyelectrolyte, and then it was dried using a freeze-drying process. The same process was repeated for the third layer (AgNPs-CS-PSS-CS) by using a CS solution. Simultaneously, zeta potential analysis was employed to monitor the surface charge of the LbL assembly at each stage. Freeze-drying was used for drying AgNPs-CS-PSS-CS [22].

4.2.1.5 Fabrication of AgNPs-CS-PSS-CS@Anti- $A\beta$ antibody (AgNPs@Anti- $A\beta$) conjugates

In this part, monoclonal anti- $A\beta$ antibody (form: buffered aqueous solution concentration: 1.5 mg/mL) was preferred for fabrication of AgNPs-CS-PSS-CS@Anti- $A\beta$ antibody conjugate. Firstly, 1 mg/mL of 5 mL solution was prepared using AgNPs-CS-PSS-CS in nuclease-free water at 20 °C. Then, this prepared solution was degassed using sonication for 5 min. After that, the EDC/NHS (1:1, 50 μ L) solution was prepared to activate the C-terminal carboxylic functional group. Finally, the C-terminal carboxylic functions of the monoclonal anti- $A\beta$ antibody were activated by the EDC /NHS mediated carbodiimide chemistry and then condensed on the amine moiety of the external cationic layer (CS) of the AgNPs-CS-PSS-CS assembly. The conjugate was subjected to aside for 5 min to accomplish complete immobilization of the antibody at 8 °C. The immobilized AgNPs-CS-PSS-CS@Anti- $A\beta$ antibody was characterized using a particle size analyzer to confirm the surface potential and particle size of the AgNPs-CS-PSS-CS@Anti- $A\beta$ antibody conjugate.

4.2.1.6. Fabrication of GO@AgNPs-Anti- $A\beta$ based SPR biosensor

Initially, the amine-modified gold (Au) coated (thickness: 50 nm) glass chip was fixed in an openSPR (excitation wavelength: 632.8 nm, 5 mW), containing a sensor cavity. The surface of the amine-modified SPR sensor chip was washed using phosphate buffer saline (PBS, 150 μ L) whereas the air bubbles were removed by injecting isopropyl alcohol (150 μ L, 80 %v/v) into the channel using a sample injection port. Then, a prepared 1 μ g/mL (100 μ L) of GO nanosheet solution was injected (flow rate: 10 μ L/min) to assemble it on amine-modified Au film by electrostatic interaction. The stability of the immobilized GO nanosheet on the surface of the sensor chip was measured through repeated washing using PBS. After that, the carboxyl groups of GO nanosheets were activated with 50 μ L of a mixture of 0.4 M EDC (70 μ L) and 0.1 M NHS (70 μ L) for 5 min offering many possible sites available at the GO

surface for antibody binding. After that, 200 μ L PBS was injected to wash excessive EDC/NHS from the surface of the biosensor [31, 32]. Different concentrations of AgNPs-CS-PSS-CS@Anti- $A\beta$ were evaluated to optimize the saturation concentration for the SPR biosensor. The optimized concentration of AgNPs-Anti- $A\beta$ solution (25 μ g/mL) was prepared using PBS (pH 7.4) and immobilized on a surface of GO nanosheets with a flow rate of 10 μ L/min. It facilitates the covalent bonding with amino groups of the Anti- $A\beta$ antibody which was immobilized on the surface of conjugates of AgNPs-CS-PSS-CS@Anti- $A\beta$ antibody. Finally, 200 μ g/mL of BSA solution was prepared in nuclease-free water at 20 $^{\circ}$ C and then injected via an SPR sample channel with a flow rate of 10 μ L/min. Interestingly, it assists to block the non-bonded carboxy functional group of GO nanosheet that helps to restrict the untargeted proteins.

4.2.1.7. Detection of $A\beta_{1-42}$ using GO@AgNPs-Anti- $A\beta$ SPR

The key principle of the SPR biosensor for $A\beta_{1-42}$ identification was based on the capture of the $A\beta_{1-42}$ peptide with a monoclonal Anti- $A\beta$ antibody. Initially, 0.5 mg of $A\beta_{1-42}$ antigen was diluted using 2 mL PBS (pH 7.4) at 20 $^{\circ}$ C. After that, different concentrations of $A\beta_{1-42}$ antigen were prepared from a range of 2 fg/mL to 1000 ng/mL (final volume: 1000 μ L) using pH 7.4 PBS. For the estimation of $A\beta_{1-42}$, the prepared lower concentration of $A\beta_{1-42}$ antigens was injected via a sampling port with a flow rate of 10 μ L/min at a programmed temperature of 25 $^{\circ}$ C. After equilibrium, glycine hydrochloride (pH 1.2) was used as a washing buffer to regenerate the GO@AgNPs-Anti- $A\beta$ SPR biosensor by detaching the $A\beta_{1-42}$ antigens from the sensor surface[31].

4.2.1.8. Detection of $A\beta_{1-42}$ in AD-induced animals CSF and blood plasma

Initially, a real-time analysis of $A\beta_{1-42}$ in adult male Wistar rats (300–350 g) animal blood and saliva was performed (Animal ethical committee reference letter no: IAEC/RCPIPER/2016-17/37). In this study, the $A\beta_{1-42}$ antigen was individually spiked (40 ng/mL) in saliva and blood samples collected from healthy animals. Then, the prepared spiked samples of $A\beta_{1-42}$ were injected into fresh GO@AgNPs-Anti- $A\beta$ SPR biosensor via a sampling port with a 10 μ L/min flow rate. The change in the response unit was measured to evaluate the real-time applicability of the GO@AgNPs-Anti- $A\beta$ SPR biosensor. Detection of $A\beta$ antigen in AD-induced animals was completed through the following process. At first, adult male Wistar rats (300–350 g) were used for induction of AD. Initially, rats were injected with intracerebroventricular (icv) streptozocin (STZ, 3 mg/kg) twice on day 1 and day 3 under anesthesia using chloral hydrate (240 mg/kg, intraperitoneal route, in 4% solution). Then, it was analyzed the learning and memory behavior. Simultaneously, blood and saliva samples

were collected from AD-induced animals and analyzed for the occurrence of $A\beta$ antigen. For 21 days, AD-induced wistar rats were sacrificed under anesthesia and the collected CSF brains of AD-induced rats were stored at $-40\text{ }^{\circ}\text{C}$. Finally, samples were analyzed for identification of $A\beta$ antigen using GO@AgNPs-Anti- $A\beta$ SPR biosensor at $25\text{ }^{\circ}\text{C}$.

4.2.1.9. Anti-interference study and other features of the biosensor

Selectivity testing is a key aspect of evaluating the built biosensor[31, 33]. In this shade, the anti-interference potential of GO@AgNPs-Anti- $A\beta$ SPR biosensor was performed by utilizing a variety of molecules including hemoglobin, BSA, cholesterol, glucose, albumin, lactoferrin, protease, citric acid, etc to ensure that the constructed biosensor could test precisely. In brief, selected interfering agents and $A\beta$ antigen were individually spiked (40 ng/mL) pH 7.4 PBS buffer (0.1 mol/L) at $20\text{ }^{\circ}\text{C}$. Then, the prepared concentrations were injected into fresh GO@AgNPs-Anti- $A\beta$ SPR biosensor via a sampling port with a $10\text{ }\mu\text{L}/\text{min}$ flow rate. The change in response unit was measured to evaluate the high selectivity potential of GO@AgNPs-Anti- $A\beta$ SPR biosensor towards $A\beta_{1-42}$ in the existence of numerous interfering substances. Furthermore, other important parameters including reproducibility and stability of fabricated SPR biosensors were also executed. As per the literature, repeatability is also important for determining the biosensor's usefulness. In this, six GO@AgNPs-Anti- $A\beta$ SPR biosensors were created. Then, biosensors were characterized under identical sensing circumstances with 4 ng/mL of $A\beta_{1-42}$ peptide in triplicates. Another significant element of a biosensor is its stability. In the present work, stability of the fabricated GO@AgNPs-Anti- $A\beta$ SPR biosensor was performed using the same concentration of $A\beta_{1-42}$ peptide for continuously 48 h. In a similar experimental condition, 400 fg/mL of $A\beta_{1-42}$ peptide was evaluated in triplicate for different time intervals.

4.2.2. Approach II

4.2.2.1. Synthesis of GO nanosheets

Synthesis of GO from graphite powder was accomplished utilizing the previously described modified Hummers technique [30, 34] supplemented by slight alterations.

4.2.2.2. Green synthesis of AuNPs

Firstly, 100 g of *Colocasia esculenta* stem waste was collected from the shirpur local market. After that, collected stem waste was subjected to cleaning using DDW, and then it was converted into small pieces. The drying of stem pieces (0.2 mm to 0.5 mm) was achieved using a laboratory hot air oven wherein the drying temperature was fixed initially at $60\text{ }^{\circ}\text{C}$ while the temperature condition was decreased to $40\text{ }^{\circ}\text{C}$ with $0.14\text{ }^{\circ}\text{C}/\text{min}$ for the next 12 h. The powder of dry stems was obtained using a laboratory grinder and then the final power

was sifted using a #20 sieve. For extraction, *Colocasia esculenta* stem powder (5 g) was mixed using DDW 100 mL. Then, the mixture was heated at 70 °C for 30 min to separate phytoconstituents that exist in the *Colocasia esculenta* stem. The ending extract was centrifuged (10000 rpm for 15 min) at 25 °C. Then, the clear supernatant of the extract was filtered using laboratory 0.22 µm sized membrane filters. The final filtrate was transferred to a refrigerator at 20 °C until further utilization for the synthesis of AuNPs. As a final point, one pot and facile green synthesis of AuNPs was accomplished using 7 mL of *Colocasia esculenta* and 100 mL of 5 mM of HAuCl₄. Then, this prepared mixture was transferred to constant stirring at 500 rpm at 50 °C[35, 36].

4.2.2.3. Characterization of GO and AuNPs

The same as I mentioned in section 4.2.1.3.

4.2.2.4. Design of polyelectrolyte-based LbL assembly

Despite the numerous benefits of AuNPs, their aggregation has a negative influence on the performance of SPR-based biosensors. It can be overcome by utilizing an LbL assembly, in which the charge on the exterior layer can help to repel the AuNPs and retain the stability in the solvent system. In this work, we intend to develop the LbL assembly using PAH (cationic) and PSS (anionic) polyelectrolytes on the face of AuNPs, wherein the external layer of PAH in LbL presents the homogeneous huge amine functionality. Importantly, it can provide the particular orientation, strong bonding, and maximum site for immobilization of carboxylic terminal containing Anti-Tau rabbit monoclonal antibody. As a result, it can contribute to the high sensitivity and selectivity towards analyte. Furthermore, the employment of PAH and PSS allows for the production of LbL assemblies based on electrostatic forces with no major modifications. In this step, accurately 200 mg of lyophilized AuNPs was incorporated into 50 mL of DI water. Next, 5 mL of 1 % (w/v) cationic PAH polyelectrolyte was added into AuNPs dispersion for initial coating (AuNPs-PAH) and then transferred to sonication for 30 min. Then, obtained AuNPs-PAH assembly was separated at 25000 rpm for 30 min at 25 °C and then it was washed with deionized water to eliminate the free form of PAH. The final obtained residue of AuNPs-PAH assembly was then processed for freeze-drying by preferring the abovementioned procedure. For the second anionic layer, 1 % PSS was prepared in a 10 mL volumetric flask using deionized water. Next, 150 mg of AuNPs-PAH was mixed with 10 mL of PSS solution with 10 min sonication at 25 °C and then ultra-cold centrifugation at 25000 rpm for 30 min at 20 °C. The separated supernatant was then discarded and remained a residue of AuNPs-PAH-PSS was washed twice using

deionized water to remove unbounded PSS from the LbL assembly. Herein, the drying of the second AuNPs-PAH-PSS assembly was performed using a laboratory freeze dryer. Finally, the third layer of cationic PAH on the exterior of dried AuNPs-PAH-PSS-PAH assembly was prepared using 1 % (w/v) PAH on the surface of AuNPs-PAH-PSS followed by the same procedure of initial PAH coating

4.2.2.5. Design of AuNPs-PAH-PSS-PAH@-Anti-Tau nanoconjugate

The preference of LbL assembly to design bioconjugate can provide a softer attachment surface for Anti-Tau rabbit monoclonal antibody immobilization on the face AuNPs. Therefore, it can aid in avoiding the denaturation of bioreceptors and other biomolecules such as BSA, Tau-441, lactoferrin, etc. As a result, the LbL assembly assists in preserving the functionality of the bioreceptors, which can result in superior SPR biosensor operation in terms of responsiveness and selectivity. In brief, the design of AuNPs-PAH-PSS-PAH@-Anti-Tau conjugate was engineered using AuNPs-PAH-PSS-PAH and Anti-Tau rabbit monoclonal antibody. Briefly, 10 mg of AuNPs-PAH-PSS-PAH was added into 100 mL of nuclease-free water at 20 °C followed by bath sonication for 3 min to remove air bubbles from dispersion. Then, 25 μ L of anti-Tau rabbit monoclonal antibody (50 μ g/mL) in pH 7.4 PBS was incorporated to immobilize on the surface of fabricated LbL assembly at 15 °C through active loading owing to interaction among the amine group of PAH and carboxylic functionality of antibody (carbodiimide chemistry). Herein, the carboxylic functionality of the Anti-Tau rabbit monoclonal antibody was activated by 100 μ L of 0.4 mM EDC/0.1 mM NHS (1:1) and then attached to the amine (NH₂) exterior moiety of PAH that was outside the cationic layer of AuNPs-PAH-PSS-PAH LbL assembly. For immobilization of activated Anti-Tau rabbit monoclonal antibody on the surface of AuNPs-PAH-PSS-PAH LbL, the obtained mixture was incubated 30 min at 15 °C. At this, the surface potential plus particle size of AuNPs-PAH-PSS-PAH@-Anti-Tau conjugate was verified using a particle size analyzer. Finally, prepared AuNPs-PAH-PSS-PAH@-Anti-Tau conjugate was further utilized for sensing of Tau 441 antigen.

4.2.2.6. Experimental setup

An experimental setup of GO@LbL-AuNPs-Anti-Tau SPR biosensor (LbL-AuNPs: AuNPs-PAH-PSS-PAH@-Anti-Tau conjugate) was prepared using amine-functionalized gold (Au)-coated glass slide (Au: 50 nm thickness), GO nanosheets, and AuNPs-PAH-PSS-PAH@-Anti-Tau conjugate.[37] At first, the NH₂-modified gold-coated sensor chip was incorporated into laboratory semiautomated OpenSPR (Nicoya Lifesciences, Canada). After this, the outside of the NH₂ functionalized surface of the sensor chip was cleaned with 150 μ L of pH

7.4 PBS and DI nuclease-free water in triplicates. In addition, the sample channel of OpenSPR was cleaned by injecting 200 μL of IPA via the sample port for the removal of air bubbles from the channel. Simultaneously, GO nanosheets (100, 200, 300, 400, and 600 $\mu\text{g/mL}$) were dispersed in nuclease-free water. Here, a 1:1 ratio of 0.4 mM EDC/0.1 mM NHS (100 μL) was used to activate GO-containing carboxylic functionality. The activated 150 μL of GO dispersion was then injected through a sample port (flow rate: 15 $\mu\text{L/min}$). After 600 sec, the biosensor surface was washed twice with 150 μL of PBS to remove any leftover EDC/NHS and GO sheets from the channel port and biosensor surface. After optimization of GO concentration, this procedure was repeated to ensure that the GO nanosheets were completely immobilized on the amine-functionalized sites present on the chip surface of the SPR sensor. Here, carbodiimide chemistry was used to adhere the nanosheets to an amine-modified biosensor surface. After next, dispersion of AuNPs-PAH-PSS-PAH@-Anti-Tau conjugate (10, 15, 20, 25, and 30 $\mu\text{g/mL}$) was injected (Flow rate: 10 $\mu\text{L/min}$). It was immobilized on the surface of activated GO-containing activated surface that offers the covalent association among antibody-containing amine functional groups and nanosized GO-containing carboxyl groups. After 400 seconds, the biosensor surface was washed twice with 150 μL of PBS to remove any leftover AuNPs-PAH-PSS-PAH@-Anti-Tau conjugate from the activated GO nanosheet surface and channel port. After this optimization, masking of a free surface group of activated GO was accomplished through masking agent BSA (flow rate: 10 $\mu\text{L/min}$, concentrations: 50, 100, 150, 200, and 250 $\mu\text{g/mL}$ in nuclease-free water). After that washing was performed using 150 μL of PBS twice to remove any leftover BSA from the activated GO nanosheet surface and channel port. Finally, a similar process was repeated using optimized BSA concentration to confirm the complete masking of the activated free surface group of immobilized GO nanosheets on the surface of the SPR biosensor. As a result, the masking using BSA prohibits the interaction with different interfering substances that existed in analytical samples.

4.2.2.7. Biosensing of Tau-441 antigen

Biosensing of Tau-441 antigen was achieved using the anticipated GO@LbL-AuNPs-Anti-Tau SPR biosensor. In brief, the stock concentration of Tau-441 antigen (0.5 $\mu\text{g/mL}$) was prepared using pH 7.4 PBS at 20 $^{\circ}\text{C}$, and then a diverse range of concentrations was prepared from 150 ng/mL to 5 fg/mL (Final volume: 5000 μL) using freshly prepared PBS (pH 7.4). Biosensing of Tau-441 antigen was achieved by injecting 50 μL of lower concentration using a syringe via sample port (flow rate: 10 $\mu\text{L/min}$) and waiting for 120 sec to complete the binding of Tau-441 and Anti-Tau rabbit monoclonal antibody. Then, pH 1.2-glycine

hydrochloride was preferred as a cleaning agent (or regenerating agent) to remove bound Tau-441 antigen from the surface of the Anti-Tau rabbit monoclonal antibody. Similarly, the remaining concentrations of Tau-441 antigen were injected to validate the wide linear concentration range using the anticipated affinity GO@LbL-AuNPs-Anti-Tau SPR biosensor. Finally, the limit of detection (LOD: $3.3 \times \text{standard deviation (SD)} / \text{Slope}$) was assessed using an obtained slope from the calibration curve of Tau-441 antigens and the SD of their SPR responses. Overall, the designed GO@LbL-AuNPs-Anti-Tau SPR biosensor was validated for the capability to sense a low concentration of Tau-441 antigen as an AD biomarker through a shift of the SPR reflectance curve[8, 38].

4.2.2.8. Selectivity, stability, and reproducibility analysis

The same as I mentioned in the first part 4.2.1.9.

4.2.2.9. Spiked sample analysis of Tau-441 antigen

The same as I mentioned in the first part.

4.2.2.10. Tau-441 antigen biosensing in AD-induced animals using GO@LbL-AuNPs-Anti-Tau SPR biosensor

The same as I mentioned in 4.2.1.8.

4.2.3. Approach III

4.2.3.1. Synthesis of GO nanosheets from graphite flakes

In this study, the earlier authored modified Hummers approach with subtle changes was implemented to synthesize the 2D non-plasmonic carbon backbone, namely GO nanosheets [39].

4.2.3.2. Green synthesis of Pt-NPs

In this work, the 5 g of dried leaves of *Terminalia catappa* L. powder was loaded into a conical flask (250 mL capacity) and well mixed with 100 mL DDW. The resulting mixture was heated for 20 min at 50 °C before being processed using Whatman filter paper. To remove the solid debris, the obtained filtrate was centrifuged at 14,000 rpm for 30 min at a prescribed process temperature (15 °C). Lastly, the filtered leaf extract was kept in a refrigerator at 20 °C to reduce decomposition. After 24 h, the extract was employed for the green production of Pt-NPs. Concisely; the stable Pt-NPs were produced utilizing optimal synthesis conditions [40]. First, 4 mL of *Terminalia catappa* L. leaves extract was dropped into 100 mL of 5 mM of $\text{H}_2\text{PtCl}_6 \cdot 6\text{H}_2\text{O}$ solution in a 250 mL conical flask at a monitored 25 °C with continual stirring at 500 rpm. The reaction mixture was then heated for 1 h at $40 \pm 3^\circ\text{C}$ then stirred for 3 h at 25 °C. After 4 h, the production of a strong reddish-brown color was seen, revealing the green synthesis of Pt-NPs. For the duration of 12 h, the Pt-NPs were

incubated at a regulated temperature (4 °C). Lastly, lyophilization of green-formed Pt-NPs was performed utilizing a previously published freeze dryer procedure (Freezone12, Labconco, MO, USA) [41].

4.2.3.3. *In vitro* characterizations of GO nanosheets and green-made Pt-NPs

The same as I mentioned in section 4.2.1.3

4.2.3.4. Development of CS-SA-CS@Pt-NPs LbL assembly

In this study, 300 mg of Pt-NPs (3000 µg/mL) were distributed in 100 mL of DDW water in a volumetric flask and stirred for 2 h at 250 rpm at a controlled temperature (25 °C). Before further use, the Pt-NPs were filtered using filter paper (0.2 µm). Concurrently, 0.4 %w/v of 'CS' solution was formed by dissolving 'CS' in 2% acetic acid and agitating at 250 rpm for 20 h (25 °C). On the contrary, the 1% w/v of 'SA' solution was formed by dissolving 'SA' in DDW water in a volumetric flask with continuous stirring at 250 rpm for 1 h. Herein, both prepared solutions were centrifuged at 15000 rpm to separate the un-dissolved part of 'CS' and 'SA' from the respective 'SA' and 'CS' solutions. Here, the LbL assembly was designed using both polymeric solutions.[42] In brief, the obtained Pt-NPs (95 mL) were combined with 10 mL of 0.4 %w/v of CS solution for the initial layer of 'CS' on the exterior of Pt-NPs (CS@Pt-NPs). Following that, the mixture was agitated at 150 rpm for 2 h before being processed at 40000 rpm and 20 °C to separate the unbound 'CS' from the LbL assembly. In this case, the obtained residual LbL assembly was cleaned three times with DDW water. Following that, the CS@Pt-NPs were lyophilized using the previously described process. This derived dry powder CS@Pt-NPs was then employed to coat the SA layer in the second LbL stage. In this study, 100 mg of CS@Pt-NPs were placed in 5 mL of 1% w/v of 'SA' solution and stirred for 2 h at 250 rpm. After this procedure, SA-CS@Pt-NPs were lyophilized. Thereafter, cationic 'CS' was deposited utilizing the initial 'CS' deposition procedure, in which 50 mg of SA-CS@Pt-NPs were mixed with 5 mL of 0.4 %w/v CS solution. Subsequently, washing and lyophilization were conducted.

4.2.3.5. Fabrication of Anti-BACE-1@CS-SA-CS@Pt-NPs bioconjugates

Initially, 5 mg of lyophilized CS-SA-CS@Pt-NPs was dispersed in 10 mL of nuclease-free water with stirring for 15 min. The obtained CS-SA-CS@Pt-NPs dispersion (500 µg/mL) was filtered using a membrane filter (0.45 µm). After this, the Anti-BACE-1 was fixed on the surface of the fabricated CS-SA-CS@Pt-NPs assembly using EDC/NHS chemistry.[43] In brief, 10 µL of Anti-BACE-1 was added into 500 µL of freshly prepared pH 7.4 PBS and the solution was kept at 10 °C. Then, the 100 mM EDC was added into the 25 mM NHS (1:1). This mixture was added into the dispersion of CS-SA-CS@Pt-NPs assembly and Anti-

BACE-1 solution at 20 °C with constant stirring at 50 rpm. In this step, the activated carboxylic functionality of Anti-BACE-1 forms amide bonding with the activated amine of CS from CS-SA-CS@Pt-NPs assembly. Finally, the Anti-BACE-1@CS-SA-CS@Pt-NPs bioconjugates were used for biosensing of the BACE-1 antigen.

4.2.3.6. BACE-1 protein detection using Anti-BACE-1-LbL@Pt-NPs-GO-SPR biosensor

In the first step of the experimental setup, Trace Drawer software connected with the OpenSPR™ instrument to assess the change in response unit of SPR sensogram after injection of BACE-1 antigen. In brief, the NH₂ decorated 'Au' thin layered glass sensor chip was locked into the OpenSPR™. Then, the sensor chip surface and sample channel were washed with 150 µL of isopropyl alcohol, pH 7.4 PBS, and DI water in triplicates (Flow rate: 100 µL/min). The airdrops were removed from the sampling channel using via injecting 150 µL of isopropyl alcohol. After this, the 150 µL of 0.4 M EDC and 0.1 M NHS solutions (1:1) were mixed with GO dispersion (1 mg/mL) at 15 °C and kept for activation of the surface COOH functional groups. Then, 100 µL of GO dispersion (50 µg/mL) was injected from the sample port (Flow rate: 50 µL/min) in duplicates wherein activated COOH-GO forms the amide bonding with NH₂ of the modified sensor chip. Then, 150 µL of pH 7.4 PBS and nuclease-free deionized water was injected from the sample port with a flow rate of 100 µL/min to remove the unbound excess GO nanosheets from the sensor surface. After this, the freshly prepared 100 µL of Anti-BACE-1@CS-SA-CS@Pt-NPs bioconjugate was incorporated to immobilize the activated surface of GO nanosheets. The 150 µL of pH 7.4 PBS and nuclease-free deionized water was injected from the sample port with a flow rate of 100 µL/min to remove the unbound Anti-BACE-1@CS-SA-CS@Pt-NPs bioconjugate from the surface. After this step, the free-activated COOH surface groups of GO were blocked using a making agent (BSA). Herein, 100 µg/mL of BSA was injected with a flow rate of 100 µL/min in duplicates. Afterward, the washing was completed using the abovementioned process. Here, the fabricated Anti-BACE-1-LbL@Pt-NPs-GO-SPR biosensor was then used for assessment of the different concentrations of BACE-1 from the range 5 fg/mL to 200 ng/mL. In brief, for linearity measurement, several BACE-1 antigen concentrations from fg to ng were prepared in pH 7.4 PBS. At first, the 5 fg/mL BACE-1 antigen was injected via a sample port with a flow rate of 50 µL/min at 15 °C. Simultaneously, the response of binding of BACE-1 with Anti-BACE-1 was monitored on a sensogram. After this step, 150 µL of 10 mM of pH 2.5 glycine hydrochloride as a regenerating buffer was injected (flow rate: 150 µL/min) to separate the bound BACE-1 antigen from the Anti-BACE-1 surface. After this, 200 µL of pH 7.4 PBS as a running buffer was injected to clean the sample channel. The

second concentration of BACE-1 was injected via the sample port using the abovementioned process. Likewise, all prepared concentrations of BACE-1 were assessed at programmed conditions and their response was noted on the SPR sensogram. Finally, the linearity range was measured by the plot of the response unit of Anti-BACE-1-LbL@Pt-NPs-GO-SPR biosensor vs concentrations of BACE-1 in PBS (pH 7.4)[8].

4.2.3.7. Selectivity study of Anti-BACE-1-LbL@Pt-NPs-GO-SPR biosensor

The same as I mentioned in the first part **4.2.1.9**.

4.2.3.8. BACE-1 protein spiked sample analysis

The same as I mentioned in the first part.

5. Results and discussion

5.1. Approach I

5.1.1. Characterization of GO

Figure 5.1.A demonstrates the UV Vis spectra of GO. In brief, the GO exhibited a characteristic absorption peak at 234 nm and a slightly low intense shoulder peak at 300 nm, which corresponds to π - π^* transitions of aromatic C=C bonds and n- π transitions of C-O bonds, respectively. Hence, it confirmed the synthesis of GO from graphite flakes. **Figure 5.1.B** showed the ATR FT-IR spectra for the GO nanosheet. Briefly, the occurrence of diverse types of oxygen functionalities in ATR FT-IR confirmed the complete oxidation of graphite flakes. The existence of a broad and wide peak at 3438.12 cm^{-1} can be attributed to the O-H stretching vibrations. The carbonyl (C=O) group stretching was observed at 1631.86 cm^{-1} , whereas OH bending (deformation) vibration and C-O stretching were obtained at 1383.78 cm^{-1} , and 1216.54 cm^{-1} , respectively. In a nutshell, it confirmed the occurrence of oxygen-containing functionality such as hydroxyl, carboxyl, and epoxy groups. The presence of oxygen functionality can provide the binding site for the immobilization of biomolecules.

Figure 5.1.C and **Figure 5.1.D** demonstrated the particle size and zeta potential of GO. Herein, particle size and zeta potential analysis was performed to confirm the distribution (or average diameters) and stability of GO nanocomposite, respectively. The particle size of the synthesized GO nanosheet was found to be 88.7 nm whereas, the PDI of GO nanosheet dispersion was found to be 0.285. It confirmed the prepared GO available in nanosize with uniform distribution in water. In the case of the zeta potential of GO, it was found to be -21.48 mV . In conclusion, zeta potential analyses of prepared GO nanosheets confirmed the stability of GO dispersion at working conditions.

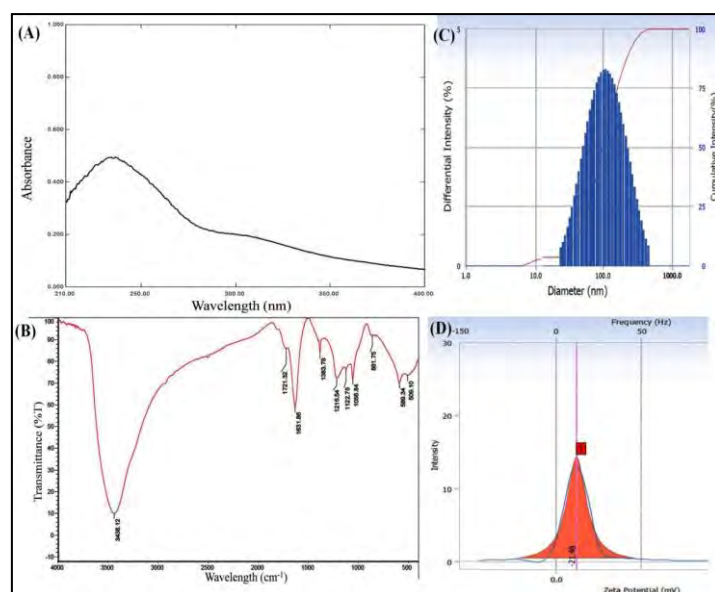


Figure 5.1: (A) UV absorption spectra of GO; (B) ATR FT-IR spectra for the GO; (C) particle size of and (D) zeta potential of GO.

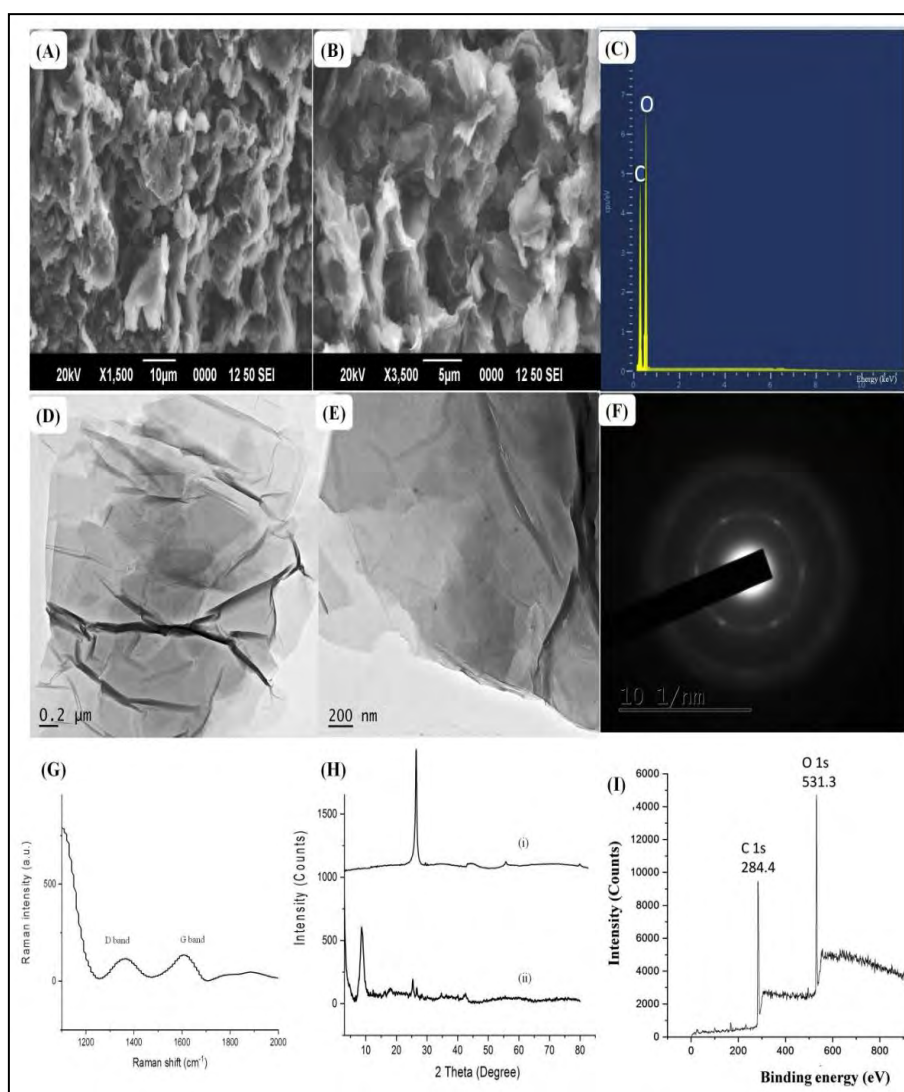


Figure 5.2: A and B SEM image of GO nanosheet; (C) EDAX spectra of GO; (D, E) HR-TEM images of GO and (F) selected area electron diffraction (SAED) pattern of GO; (G) Raman spectra of GO (H) PXRD spectra of graphite flakes (i), and GO (ii); (I) XPS survey scan spectrum of GO.

Figure 5.2.A and **Figure 5.2.B** depict the surface morphology of the GO nanosheet. The conversion of graphite flakes to GO nanosheets was exhibited in randomly aggregated and crumpled thin sheets. Moreover, it showed wrinkles and folds on the surface of GO nanosheets. It has been mentioned that the insertion of oxygen in flakes of graphite resulted in the separation of flakes into a thin nanosize sheet. Therefore, it confirmed the successful exfoliation of nanosheets and the formation of GO[44]. The EDAX investigation of the synthesized GO showed 48.89 wt% of carbon content and 40.32 wt% of oxygen assured the presence of carbon and oxygen only (**Figure 5.2.C**). In a nutshell, the elemental composition was confirmed by the purified form of the GO nanosheet. The HR-TEM analysis as shown in **Figures 5.2.D** and **5.2.E** investigated the surface morphology and structure of the synthesized GO. It revealed the graphite flakes successfully oxidized into the GO nanosheet. The morphology of multilayer GOs was found to be a rough surface, flake-like shape, not crumpled, and corrugated together with non-uniform particle size. Moreover, the apparent spherical rings in the SAED pattern also revealed the crystalline property of GO (**Figure 5.2.F**). Raman spectra of GO exhibited two bands mainly the ‘D’ band and the ‘G’ band. In brief, the breathing mode of j-points of A_{1g} symmetry was obtained at 1360 cm^{-1} (D band) whereas first-order scattering of E_{2g} photos by SP^2 carbon was found at 1590 cm^{-1} (G band). Herein, the $I(D)/I(G)$ of GO was found to be 0.85 indicating the hydrophilic nature of GO (**Figure 5.2.G**). Mainly, the ratio of the $I(D)/I(G)$ provides the graphitic composite containing defect levels. A literature survey revealed that the intensity ratio is less than 1 confirmed the formation of GO whereas more than 1 confirmed the formation of the reduced form of GO (rGO, hydrophobic) nanomaterial. Diffractograms of dry powder of separated graphite flakes (**Figure 5.2.H-i**), and GO nanosheets (**Figure 5.2.H-ii**) were investigated to study the material structure. In the case of graphene, a high intense diffraction peak was observed at $2\theta = 26.34^\circ$, which reveals the high crystallinity nature of graphene. In the case of GO, a prominent peak was observed at a lower angle ($2\theta = 10.10^\circ$, interlayer spacing: 0.29 nm) signifies the complete synthesis of nanosize GO from graphite flakes. The diffraction peak was found at $2\theta = 26^\circ$ (interlayer spacing: 0.85 nm), which may be because of the intercalation of oxygen functionalities as well as water molecules into carbon nanolayers. **Figure 5.2.I** demonstrated the XPS wide scan spectrum of GO. Herein, the survey spectrum

shows the two intense peaks for carbon and oxygen at 283.6 eV (sp^2 carbon) and 531.3 eV (C-OH, -C=O) binding energy, respectively. In this spectrum, no addition peak was obtained that assured the purity of GO. In conclusion, XPS analysis confirmed the existence of oxygen functionalities mainly carboxy, and epoxy on the surface of the GO nanosheet [45].

5.1.2. Characterization of green synthesized AgNPs

Figure 5.3.A. displayed UV Vis absorption spectra of silver nitrate (i), *Terminalia catappa* L. ripe fruit shell extract (ii), and green synthesized AgNPs (iii). In this study, after the addition of the prepared extract of *Terminalia catappa* L. ripe fruit shell, the color of silver nitrate solution converted into an amber color that confirmed the reduction of Ag^+ to Ag^0 , and finally a green synthesis of AgNPs [46]. In addition, the UV visible spectra of synthesized AgNPs displayed the surface plasmon absorption band at 416.5 nm confirming the existence of smaller-size AgNPs. Herein, the generation of AgNPs at different time intervals showed a boost in absorption band intensity when the reaction time improved. After 24 h, no changes in peak intensity were obtained that assured the completion of the reaction. Taken as a whole, *Terminalia catappa* L. ripe fruit shell extract acted as a reducing and stabilizing agent for silver ions that provide the smaller size AgNPs. **Figure 5.3.B** shows the ATR FT-IR spectra of ripe fruit shell extract of *Terminalia Catappa* (i) and green synthesized AgNPs (ii). Briefly, ATR FT-IR spectra of shell extract showed bands at 3328 cm^{-1} which were assigned to OH stretching, C=O stretching at 1619 cm^{-1} , and C-O stretching at 1038.06 cm^{-1} (**Figure 5.3.B-i**). Hence, it confirmed the presence of polyphenolic compounds in the extract [47]. On the other hand, ATR FT-IR spectra of green synthesized AgNPs showed bands at 3346 cm^{-1} which were assigned to OH stretching, C=O stretching at 1627 cm^{-1} , and C-O stretching at 1028.06 cm^{-1} (**Figure 5.3.B-ii**). To summarize, the shifting of band wavelength in ATR FT-IR of AgNPs confirmed the capping of AgNPs by different functional groups present in the extract. The particle size of green manufactured AgNPs was investigated using Nanoplus3 (DLS research), which affords details on particle size diversity and PDI of the AgNPs solution. The optimization of extract volume was performed for the synthesis of nanosized AgNPs. **Figure 5.3.C** depicts the particle size distribution of green synthesized AgNPs in solution. Notably, the size of green synthesized AgNPs was monitored upto the completion of the reaction. As a result, it showed 55.60 nm of average hydrodynamic particle size whereas the PDI of AgNPs was found to be 0.279 assuring the monodispersity of nanoparticles. Overall, it confirmed the green synthesis of monodispersed AgNPs within the range of nanometer. As per the literature, zeta

potential provides information about the stability of green synthesized metal nanoparticles in provided dispersion. Herein, the zeta potential of AgNPs has been reported to illustrate the surface charge, which appeared to be negative for green synthesized AgNPs (-27.01 mV, **Figure 5.3.D**). The high negative values indicate particle repulsion, which results in higher stability of AgNPs and avoidance of agglomeration. In conclusion, it assured the synthesis of stable and nanosized AgNPs by the green synthesis method.

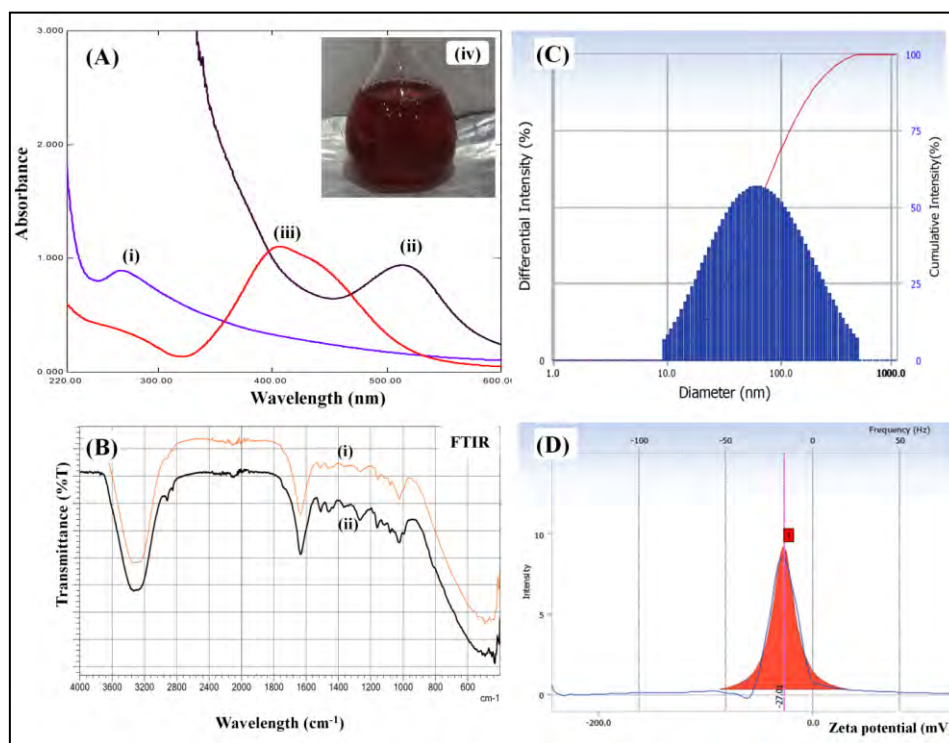


Figure 5.3: (A) UV Vis absorption spectra of silver nitrate (i), *Terminalia catappa* L. ripe fruit shell extract (ii), green synthesized AgNPs (iii), and image of AgNPs (iv). (B) ATR FT-IR spectra of *Terminalia catappa* L. ripe fruit shell extract (i), green synthesized AgNPs (ii). (C) Particle size analysis and (D) Zeta potential of green synthesized AgNPs.

The elemental composition of AgNPs was measured using EDAX analysis which provides the absolute composition and purity of the prepared AgNPs. **Figure 5.4.A** demonstrated that the 35.68 wt% compositions of silver ‘Ag’ along with that 35.67 wt% oxygen (O) and 19.94 wt% of carbon (C) were observed in green made AgNPs. The strong signal in the ‘Ag’ region gives the authentication of ‘Ag’ without other contaminants. The diffractogram of green synthesized AgNPs is depicted in **Figure 5.4.B**. Principally, the diffractogram of AgNPs revealed the exact nature of AgNPs. Herein, Bragg’s model diffraction peak at 2θ at 38.09° and 64.45° confirmed the crystalline nature of AgNPs. The obtained PXRD pattern of AgNPs confirmed the complete reduction of Ag^+ ions due to the

ripe fruit shell extract of *Terminalia Catappa*. The HR-TEM images of prepared AgNPs divulged the surface morphology, shape, and size of nanoparticles.

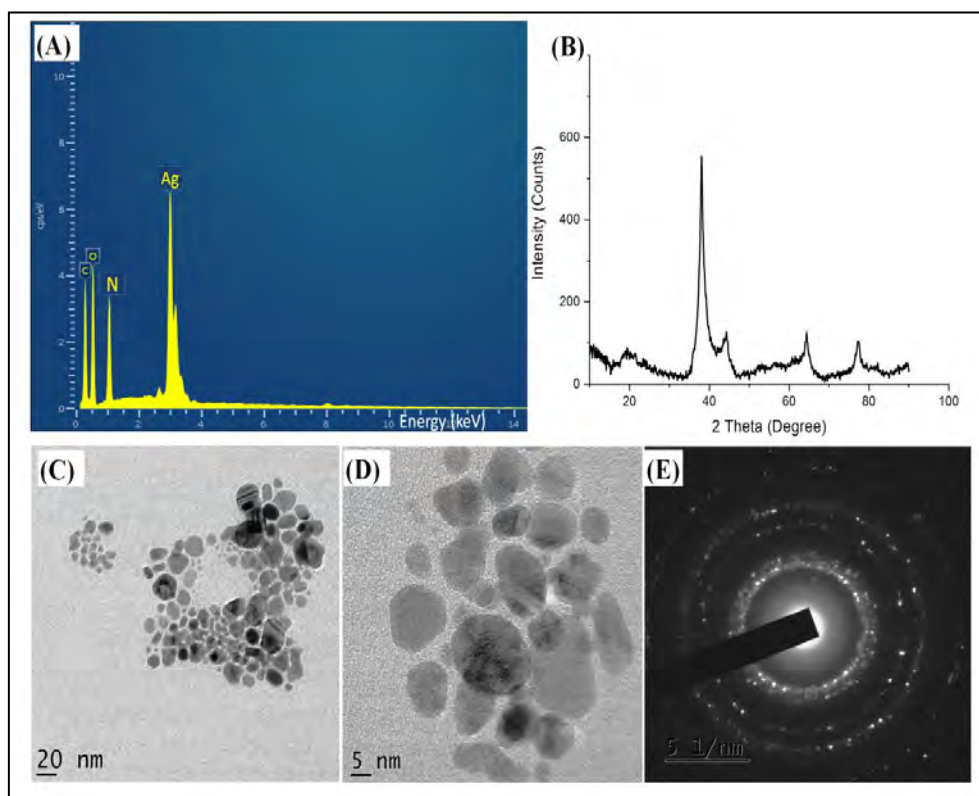


Figure 5.4: (A) EDAX spectra of green synthesized AgNPs; (B) diffractogram of green synthesized AgNPs; (C and D) HR-TEM images of AgNPs; (E) SAED pattern of AgNPs. The HR-TEM images of AgNPs (**Figure 5.4.C** and **5.4.D**) and the SAED pattern of AgNPs (**Figure 5.4.E**). The obtained HR-TEM images indicated that the morphology of the synthesized AgNPs is spherical with polydispersed in solution [48]. The AgNPs size range was found to be 14.36 nm to 21.80 nm whereas the apparent spherical rings in the SAED pattern reveal its polycrystalline property. In this work, XPS analysis was used to investigate the composition and oxidation state of the AgNPs. In brief, the typical survey spectrum of the green synthesized AgNPs revealed the presence of Ag, C, N, and O (**Figure 5.5.A**). Principally, the existence of silver (Ag) metal was confirmed due to the occurrence of the strong signal of Ag3d (~496.8 eV). Moreover, the presence of carbon (C) was confirmed due to the C1s peak obtained at ~284.3 eV of binding energy. It assured that the capping and stabilizing of the AgNPs by phytoconstituents present fruit shell extract. The XPS spectrum of oxygen (O) was found at ~531.2 eV of binding energy. **Figure 5.5.B** shows the Ag 3d high-resolution XPS spectrum. The Ag3d3/2 and Ag3d5/2 peaks are separated into two sets at 368.21 eV/368.89 eV and 366.93 eV/367.47 eV, respectively.

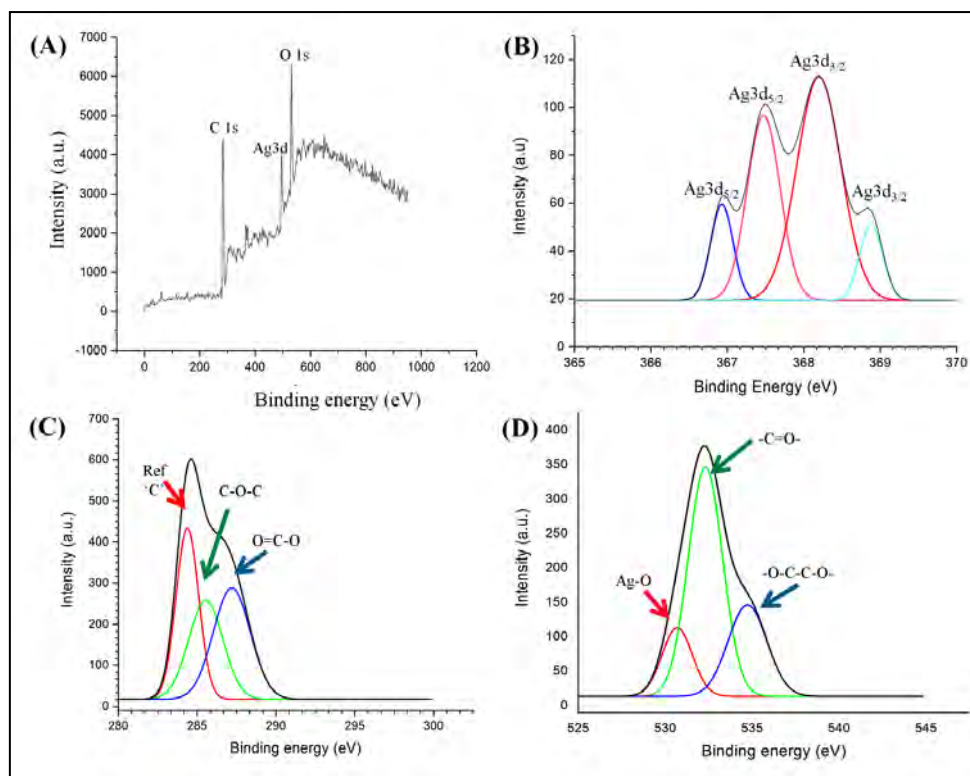


Figure 5.5: XPS spectra of AgNPs (A) survey spectrum; (B) Ag3d; (C) C1s and (D) O1s. Metallic ‘Ag’ is responsible for the peaks at 367.47 eV and 368.89 eV. In these spectra, loss characteristics are detected on the stronger binding energy edge of each ‘Ag’ metal spin-orbit component. Moreover, the spectrum peak in the C1s is related to various identical peaks with binding energies of 284.29 eV, 285.57 eV, and 288.14 eV. Possibly, these peaks are ascribed to the C1s (**Figure 5.5.C**) such as carboxyl carbon ($-\text{O}-\text{C}=\text{O}$), and carbon ($-\text{C}-\text{O}$). The peak of O1s has also been deconvoluted into two bands as shown in **Figure 5.5.D**. Herein, the peak at the lower energy side (530.54 eV) can be ascribed to the O1s core peak of O^{2-} bound to metal (Ag^+). Notably, the other peak located at 532.35 eV should possibly be attributed to the oxygen (O) in the carboxyl functional group ($-\text{C}=\text{O}-$) that bounds to the AgNPs surface. The peak at 534.74 eV existed which maybe because of the $-\text{CH}_2-\text{O}-\text{CH}_2$ backbone. Overall, the XPS analysis confirmed the synthesis of AgNPs using extract-containing biomolecules.

5.1.3. Characterization of LbL (AgNPs-CS-PSS-CS) assembly

In this part, the deposition of the ‘CS’ and ‘PSS’ layers of AgNPs was checked using an increased average diameter of coated AgNPs. In brief, the size of green synthesized AgNPs and prepared LbL assembly was measured using Nanoplus 3 (**Figure 5.6.A**). Initially, the coating of ‘CS’ on the surface of AgNPs (AgNPs-CS) showed an 89.4 nm average diameter (PDI: 0.267) that somewhat increased as compared to uncoated AgNPs (55.6 nm, PDI: 0.279). After that, the AgNPs-CS-PSS and AgNPs-CS-PSS-CS

assembly showed a rise in diameter of LbL assembly with respective 'PSS' and 'CS' layer deposition. Particularly, the average particle size of AgNPs-CS-PSS and AgNPs-CS-PSS-CS was found to be 111.1 nm (PDI: 0.222) and 129.7 nm (PDI: 0.424), respectively. In this, coating of 'CS' and 'PSS' on the surface of AgNPs resulted in a rise in the actual diameter of assembly. The successful deposition of cationic polymer (CS) and anionic polymer (PSS) on the surface of green synthesized AgNPs was confirmed through zeta potential analysis (**Figure 5.6.B**). Initially, the zeta potential of the prepared AgNPs solution was found to be -28.34 mV. The zeta potential of 'CS' and 'PSS' was found to be +36.39 mV and -31.58 mV, respectively confirming their cationic and anionic nature. Interestingly, the initial coating of AgNPs using 'CS' (AgNPs-CS) was shown a positive surface zeta potential of +29.01 mV confirming the deposition of the cationic 'CS' layer. Then, the deposition of an anionic layer of 'PSS' on the surface of AgNPs-CS developed the AgNPs-CS-PSS assembly that showed the negative zeta potential of about -21.74 mV, which confirmed the successful deposition of 'PSS' on the cationic layer. Finally, the deposition of the third layer of polymer (CS) on the surface of AgNPs-CS-PSS has demonstrated the zeta potential of about +33.47 mV that assures the formation of 'CS' coating on the surface of AgNPs-CS-PSS assembly. Herein, the zeta potential of 'CS' and 'PSS' within the acceptable range helps to stabilize the AgNPs. Mainly, the final assembly containing cationic amino surface functional groups on the surface of CS offers the immobilization of Anti- $A\beta$ antibodies via activation of carboxyl functional groups. Herein, the adsorptions of the CS offer plenty of amine group (NH_2) that get interact with PSS electrostatically. Overall, particle size analyses and zeta potential measurements revealed the depositing of CS and PSS on the surface of green synthesized AgNPs, as well as the successful production of LbL assemblies. The ATR FT-IR analysis was performed to confirm the synthesis of LbL assembly. Firstly, the ATR FT-IR spectra of green synthesized AgNPs showed strong intense peaks at 3340 cm^{-1} and 3430 cm^{-1} that confirmed the presence of hydroxyl (O-H) and amine (N-H) functional groups (**Figure 5.6.C**). Concisely, it confirmed the presence of polyphenolic compounds, proteins, and amino acids in the extract. Moreover, the intense peak at 1682 cm^{-1} confirmed the occurrence of the amide I band whereas the peak at 1350 cm^{-1} assured the existence of the amide I band and -C-N- stretching. Possibly, the band of amide I was linked to the carbonyl group stretch mode (C=O) connected to the amide bond [49]. The characteristic peaks of 4 % CS were found at 2960 cm^{-1} and 2880 cm^{-1} confirming the presence of $-\text{CH}_3$, and $-\text{CH}_2$ stretching whereas O-H and N-H stretching overlapped at

3420 cm^{-1} . Moreover, stretching vibration at 1658 cm^{-1} confirmed the presence of C=O whereas N-H bending was observed at 1539 cm^{-1} . The C–O stretching for the primary and secondary hydroxyl group was obtained at 1030 cm^{-1} and 1085 cm^{-1} , respectively. The ATR FT-IR spectra of PSS disclosed the C–H stretching at 2921 cm^{-1} . In addition, benzene ring in-plane bending and skeleton vibration were obtained at 1010 cm^{-1} and 1140 cm^{-1} . The intense peak at 1065 cm^{-1} confirmed the presence of sulphonate (SO_3) functionality. In the case of the LbL approach, these abovementioned functional groups were retained in LbL assembly. The formation of the CH layer on the AgNPs surface alters the wavelength whereas it masks the functional groups. Therefore, it resulted in a change in peak intensity. The existence of C–O stretching for the primary O-H and secondary O-H was obtained at 1032 cm^{-1} and 1078 cm^{-1} , respectively. Similarly, deposition of PSS on AgNPs-CH resulted in changes in peak intensity wherein an intense peak at 1068 cm^{-1} confirmed the presence of SO_3 functionality. The ATR FT-IR spectra of the final assembly of AgNPs-CH-PSS-CH illustrated the broad peak for -OH, -NH whereas the intense peak for C=O, C-O, and $-\text{SO}_3$ assured the successful development of LbL assembly on the surface of green synthesized AgNPs using CS and PSS.

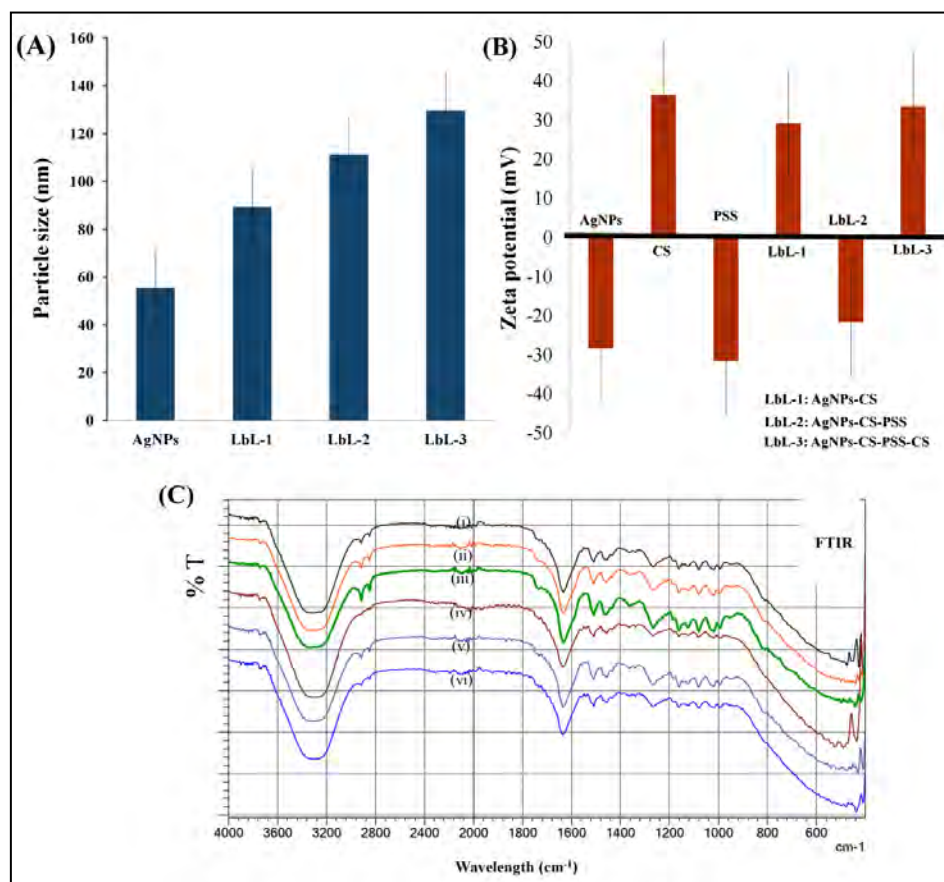


Figure 5.6: (A) Particle size of LbL assembly ($n = 3$); (B) Zeta potential of AgNPs-CS-PSS-CS assembly ($n = 3$); (C) ATR FT-IR spectra of green synthesized AgNPs (i), CS (ii), PSS (iii), AgNPs-CS (iv), AgNPs-CS-PSS (v), and AgNPs-CS-PSS-CS (vi).

For further confirmation, HR-TEM was employed to observe the surface morphology of AgNPs and LbL assembly including AgNPs-CS, AgNPs-CS-PSS, and AgNPs-CS-PSS-CS. HR-TEM images of green synthesized AgNPs (**Figure 5.7.A**) showed smooth and spherical surface morphology with particle sizes ranging from 14.2 nm to 25.15 nm (Average diameter: 18.22 nm). **Figure 5.7.B.** demonstrates the coating of CH on the surface of AgNPs which resulted in the noticeable changes in the surface morphology of AgNPs. Herein, the rough and coarse surface morphology was found after the initial coating of CH. In addition, the average diameter of AgNPs-CH was found to be 29.02 nm.

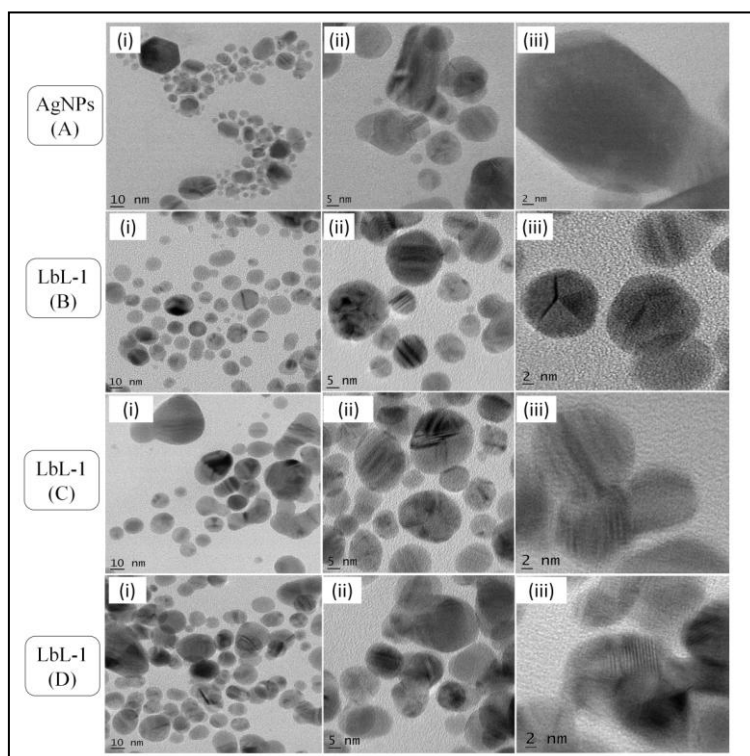


Figure 5.7: HR-TEM images of green synthesized AgNPs (A: i, ii, and iii); AgNPs-CS (B: i, ii, and iii), AgNPs-CS-PSS (C: i, ii, and iii), and AgNPs-CS-PSS-CS (D: i, ii, and iii).

Figure 5.7.C depicts the morphology of AgNPs-CS-PSS. In this case, deposition of the second layer of PSS on the surface of AgNPs-CS resulted in noticeable changes as compared to the previous layer of CS. The non-uniform and rough texture that has existed after the coating of PSS offers proof of the formation of the anionic polymeric layer. Herein, the AgNPs-CS-PSS particle size range was found to be 24.12 nm to 40.01 nm (Average diameter: 33.85 nm). The final layer of CS on the surface of AgNPs-CS-PSS-CS has exhibited the formation of an analogous surface morphology with AgNPs-CS that provides

evidence for the formation of the third layer of CS on the surface of AgNPs-CH-PSS (**Figure 5.7.D**). In this assembly, the particle size range was found to be 35.08 nm to 69.12 nm whereas the average diameter was found to be 48.84 nm. Overall, HR-TEM images confirmed the development of polyelectrolyte (cationic and anionic polymers) layers on the surface of green synthesized AgNPs.

5.2. Approach II

In this study, the GO nanosheets were produced by adopting an earlier documented process. Then, it was analyzed through numerous *in vitro* spectroscopical characterizations. After this, *Colocasia esculenta* stem extract was chosen as the reducing agent for the formation of green-made AuNPs. Having followed that, the AuNPs-PAH-PSS-PAH as an LbL polyelectrolyte assembly was formed and then preferred to affinity bioreceptor localization using carbodiimide chemistry. Additionally, GO@LbL-AuNPs-Anti-Tau SPR biosensor was adopted for Tau-441 sensing as an exceptionally responsive and specific affinity biosensing probe. Subsequently, the anti-interference possibility and real-time analysis were achieved by adopting a produced GO@LbL-AuNPs-Anti-Tau SPR-based affinity biosensor.

5.2.1. Characterization of green synthesized AuNPs

In this study, adequate characterizations of green synthesized AuNPs were performed to verify the creation of a stable and pure form of nano-dimension-based AuNPs. Primarily, the formation of AuNPs was studied relying on the variations in the color of the reaction mixture. **Figure 5.8** depicts the UV Vis absorption spectra of AuNPs with stem extract (A) 3 % v/v, (B) 5 % v/v, (C) 7 % v/v, and (D) 9 % v/v. After this confirmation, the AuNPs were subjected to additional characterizations such as UV Vis spectroscopy, ATR FT-IR spectroscopy, HR-TEM analysis, XPS analysis, SEM-EDAX analysis, and so on. In brief, **Figure 5.9.A** showed the images of *Colocasia Esculenta* stem extract (I), chloroauric acid solution (II), and green synthesized AuNPs (III). The inclusion of purified *Colocasia Esculenta* stem extract to chloroauric acid leads to a color shift from pale yellow to ruby red [50] during 4 h of reaction time that was an absence in extract and chloroauric acid. According to the literature, interacting electromagnetic fields resulted in a cumulative oscillation of free conduction electrons that provide intense color. These are acknowledged as surface plasmon resonances. **Figure 5.9.B** shows the UV-Vis spectra of concentrated *Colocasia Esculenta* stem extract (I), chloroauric acid solution (5 mM) (II), and green synthesized AuNPs (III). In the case of extract, it exhibited absorption peaks at 271.5 nm and 343.5 nm, which may be because of the existence of different phytochemicals. UV Vis spectra of prepared 5 mM chloroauric acid were found at 263 nm and 364.5 nm confirming

the presence of a pure form of chloroauric acid. Finally, the formation of AuNPs using stem extract and chloroauric acid was confirmed using UV Vis spectra. Here, synthesized AuNPs displayed an absorption (surface plasmon resonance) band at 539 nm. In this, AuNPs exhibited wide plasmon bands, preceded by an absorption tail approaching the longer wavelength zone[51].

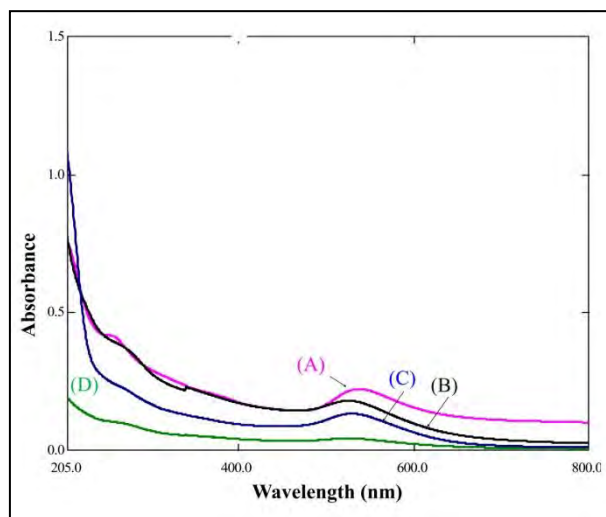


Figure 5.8: UV absorption spectra of AuNPs with *Colocasia Esculenta* stem extract (A) 3 % v/v, (B) 5 % v/v, (C) 7 % v/v, and (D) 9 % v/v

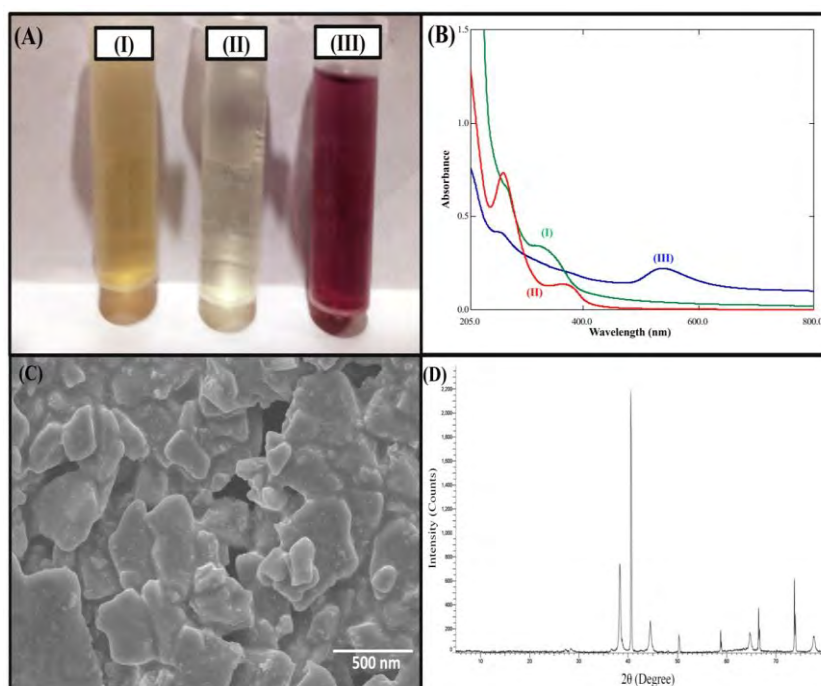


Figure 5.9: (A) Images of stem extract of *Colocasia Esculenta* (I), 5 mM chloroauric acid solution (II), and green synthesized AuNPs (III). (B) UV Vis absorption spectrum of concentrated *Colocasia Esculenta* stems extract of (I), chloroauric acid solution (5 mM) (II), and green synthesized AuNPs (III). (C) SEM image of synthesized AuNPs showing irregular, polyhedral morphology with a 500 nm scale bar. (D) XRD pattern of synthesized AuNPs showing a sharp peak at $2\theta \approx 38^\circ$ and several smaller peaks at higher angles, indicating crystalline structure.

and green synthesized AuNPs (III). (C) SEM image of green synthesized AuNPs. (D) The diffractogram of green synthesized AuNPs.

As a result, it demonstrated the effective green synthesis of AuNPs utilizing *Colocasia esculenta* stem extract as a reducing agent, stabilizing agent, and capping agent for gold ions. The surface morphology of developed AuNPs is seen in **Figure 5.9.C**. It depicts the smooth surface morphology with various forms of AuNPs such as spherical, rod, polygonal, etc.[52]. Furthermore, there is no aggregation of green-made AuNPs in SEM images, implying high stability due to the presence of stabilizing and capping agents in the extract. The diffractogram of eco-friendly formed AuNPs is displayed in **Figure 5.9.D**. It demonstrated the high-intensity diffraction peak from the range of ($2\theta = 30^\circ$ - 80°).[53] In short, it showed high peak intensities at 38.33° , 40.66° , 44.55° , 50.26° , 58.70° , 64.77° , 66.60° , 73.90° , and 77.8° , which proved the crystalline structure of green made AuNPs. As well, there was no extra high-intensity peak in the diffractogram of AuNPs was obtained, indicating the excellent purity of AuNPs produced using a greener method [54]. The mean particle size, as well as PDI of the eco-friendly produced AuNPs, were determined to be 52.12 nm and 0.29, respectively (**Figure 5.10.A**). Finally, the PDI and particle size of AuNPs validated their uniform dispersion in water. The zeta potential of AuNPs produced using the extract was -22.72 mV (**Figure 5.10.B**), indicating colloidal stability. Overall, the *Colocasia Esculenta* stem extract containing biomolecules acts as a stabilizing agent for AuNPs.[55]

The possible functional groups of biomolecules involved in the capping and reduction of AuNPs were identified using ATR FT-IR spectroscopy. **Figure 5.10.C-(I)** depicts the ATR FT-IR spectra of the stem extract of *Colocasia Esculenta*. In brief, the major stretching vibrations appeared at 3000 cm^{-1} to 3600 cm^{-1} , which denotes the existence of the 'O-H' stretching vibrations, which denotes the occurrence of functional groups comprising the 'O-H' stretch. The intense peak stretching at 1300 cm^{-1} and 1700 cm^{-1} specify the occurrence of 'C-O' and 'C=O' in the prepared stem extract. Furthermore, peaks at 1600 cm^{-1} and 1550 cm^{-1} assured the occurrence of amide linkages of the proteins present in the stem extract of *Colocasia Esculenta*. As well, the peak at 1050 cm^{-1} assured the presence of 'C-OH' and 'C-O-C' stretching vibrations. The 'C-N' stretching was obtained at 1380 cm^{-1} , which validates the existence of amine functionality in the *Colocasia Esculenta* stem extract. **Figure 5.10.C-(II)** shows the ATR FT-IR spectrum of green synthesized AuNPs. In brief, a peak at 1720 cm^{-1} was obtained due to the carboxylic (C=O) stretching vibrations mode because of the 'COOH' functionality in the extract bound to the AuNPs. The peak at 1315 cm^{-1} validates the existence of 'C-O' in AuNPs. The occurrence of amide bonds I and II were obtained at 1610

cm^{-1} and 1570 cm^{-1} , which showed the shifting toward the higher frequency as compared to the plain stem extract. Notably, it may be because of the capping and reduction of AuNPs in the presence of biomolecules in the stem extract of *Colocasia Esculenta*. In addition, the 'C-H' bond stretching was observed in the region of 2932 cm^{-1} as well as 2914 cm^{-1} in stem extract. Interestingly, the 'C-H' bond from the stem extract was divided into two vibrations namely 2912 cm^{-1} and 2822 cm^{-1} in ATR FT-IR of AuNPs confirming the change in transmittance which may be the formation of AuNPs. The EDAX confirmed the presence of % element composition in produced AuNPs. The EDAX spectrum of green-produced AuNPs is shown in **Figure 5.10.D**. In summary, it demonstrated a significant signal for 'Au', 'O', 'C', and 'N' wherein % wt was found to be 22.97 %wt, 18.14 %wt, 30.64 %wt, and 21.9 %wt, respectively. In addition, it showed the existence of chlorine (Cl) with 6.35 %wt because of AuCl_4^- a small fraction. Concisely, it proved the existence of 'Au', 'O', 'N', and 'C' in green-produced AuNPs.

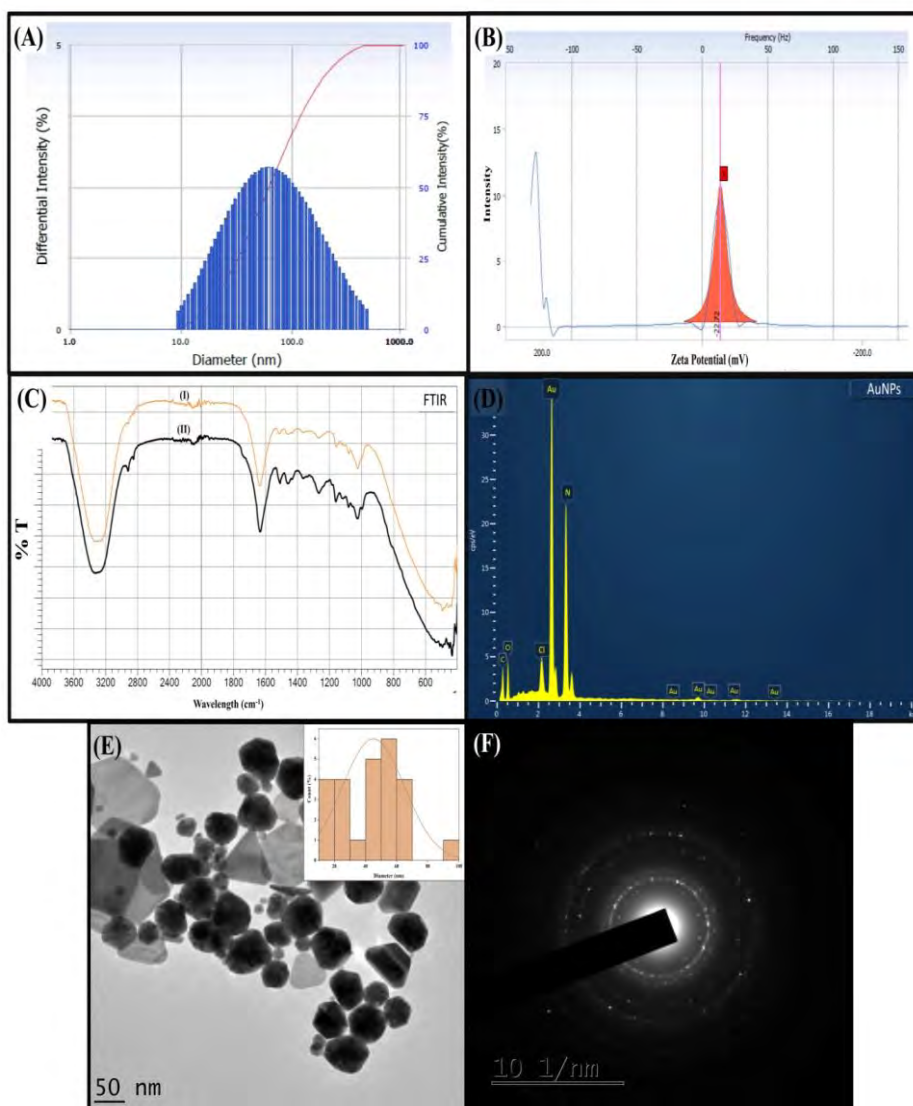


Figure 5.10.: (A) Particle size and (B) Zeta potential analysis of green synthesized AuNPs. (C) ATR FT-IR spectra of stem extract of *Colocasia esculenta* (I) and green synthesized AuNPs (II). (D) EDAX spectrum of obtained AuNPs. (E) HR-TEM images of AuNPs. (F) SAED pattern of green-made AuNPs.

The HR-TEM was used to analyze the size, particle distribution, and structure/shape of the green-produced AuNPs [35], as shown in **Figure 5.10.E**. In summary, the mean diameter of the AuNPs was determined to be within nanometer size, with a spherical particle form and some hexagonal and triangular patterns [52]. Furthermore, the uniform dispersion of produced AuNPs in a medium is substantiated by the HR-TEM, which revealed no aggregation due to the capping of AuNPs by biomolecules contained in the extract. The average particle size of AuNPs was found to be 45.08 nm ($N = 25$; Software name: ImageJ). As a result, it ensured that the green method successfully produced randomly oriented nanosized, stable, and monodispersed AuNPs. The SAED pattern proved the crystalline architecture of AuNPs [35]. The SAED pattern of produced AuNPs is shown in **Figure 5.10.F**. It exhibited the round luminous rings in the SAED model of AuNPs, revealing the crystalline characteristic of AuNPs [51]. A review of the literature indicated that the XPS spectrum offered facts on the surface of the substrate comprising elements such as metal ions, carbon, nitrogen, oxygen, and so on. Here, the XPS spectrum of green-produced AuNPs is shown in **Figure 5.11**. In summary, it gives precise insights into the chemical composition and structure of gold (Au), carbon (C), nitrogen (N), and oxygen (O) in the produced nanosized material AuNPs using the green method. **Figure 5.11.A** depicts the survey scan pattern of green synthesized AuNPs for elements primarily 'Au4f_{7/2}', 'C1s', 'N1s', and 'O1s' with binding energies of 82 eV, 283 eV, 423 eV, and 530 eV, respectively. **Figure 5.11.B** represents the deconvoluted spectra of 'C1s'. It exhibits three binding energy levels for 'C-C', 'C-N', and 'C=O' at 284.06 eV, 285.32 eV, and 286.40 eV, accordingly. **Figure 5.11.C** illustrated the high core-level spectra of 'Au4f'. Here, it indicates peaks with binding energies of 81.38 eV and 86.18 eV for 'Au 4f_{7/2}' and 'Au 4f_{5/2}', respectively, which verified the appearance of AuNPs in formed nanoparticles. In the instance of the 'O1s' high core level spectra (**Figure 5.11.D**), it reveals two peaks at 532.6 eV and 533.73 eV as binding energy, which is attributable to the existence of 'C=O' and 'C-O', individually. **Figure 5.11.E** illustrated the XPS core level spectrum of 'N1s'. It yields one peak with a binding energy of 400 eV, which is allocated to the 'N-C' bonding. As a result, it signifies that no more impurities were present in the produced AuNPs. In a sense, it ensured that 'Au', 'N', 'C', and 'O' were abundant in eco-friendly formed AuNPs [56].

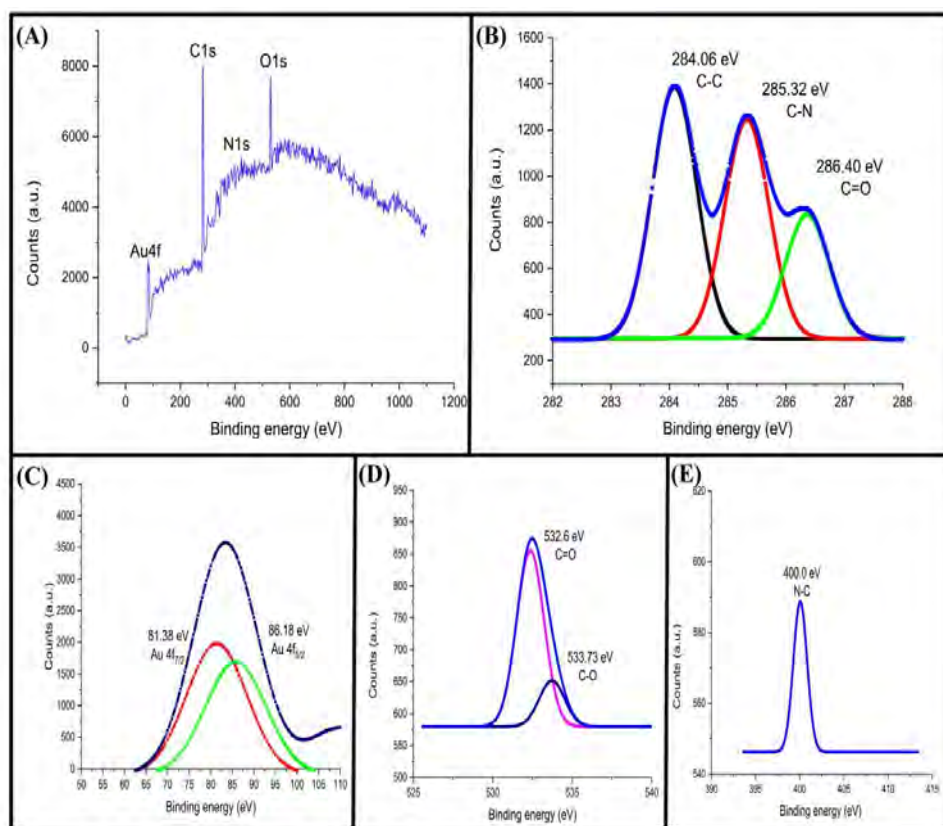


Figure 5.11: (A) Survey scan spectrum of green obtained AuNPs. XPS core level spectrum of (B) C1s, (C) Au4f, (D) O1s, (E) N1s

5.2.2. Characterizations of LbL assembly

The zeta potentials of freeze-dried AuNPs, PAH, PSS, AuNPs-PAH (LbL-1), AuNPs-PAH-PSS (LbL-2), and AuNPs-PAH-PSS-PAH (LbL-3) are depicted in **Figure 5.12.A**. In summary, zeta potential testing of polyelectrolyte (PAH/PSS)-coated AuNPs revealed the occurrence of cationic polyelectrolyte (PAH) or anionic polyelectrolyte (PSS) outer layer in the proposed LbL assembly. Herein, the zeta potential of AuNPs, PAH, and PSS was found to be -24.55 ± 0.20 mV, $+40.33 \pm 0.07$ mV, and -21.48 ± 0.15 mV, respectively. In the case of LbL assembly, the zeta potential of AuNPs-PAH, AuNPs-PAH-PSS, and AuNPs-PAH-PSS-PAH was obtained to be $+37.02 \pm 0.06$ mV, -11.61 ± 0.49 mV, and $+23.14 \pm 0.11$ mV, respectively. It implies that the zeta potential changes in response to changes in the outer layer of the LbL arrangement. In summary, the positive zeta potential of PAH as an out layer of LbL assembly is revealed in the presence of amine functionality, whereas the negative zeta potential of PSS as an exterior coating of LbL assembly is noted due to the presence of SO_3^- [57]. Overall, it demonstrated the effective deposition of polyelectrolytes (specifically PAH and PSS) on the surface of AuNPs as part of an LbL assembly. It also ensured the creation of

a stable form of LbL assembly in a solvent system. Moreover, it played an advantageous role in subsequent antibody binding on the surface of the LbL assembly.

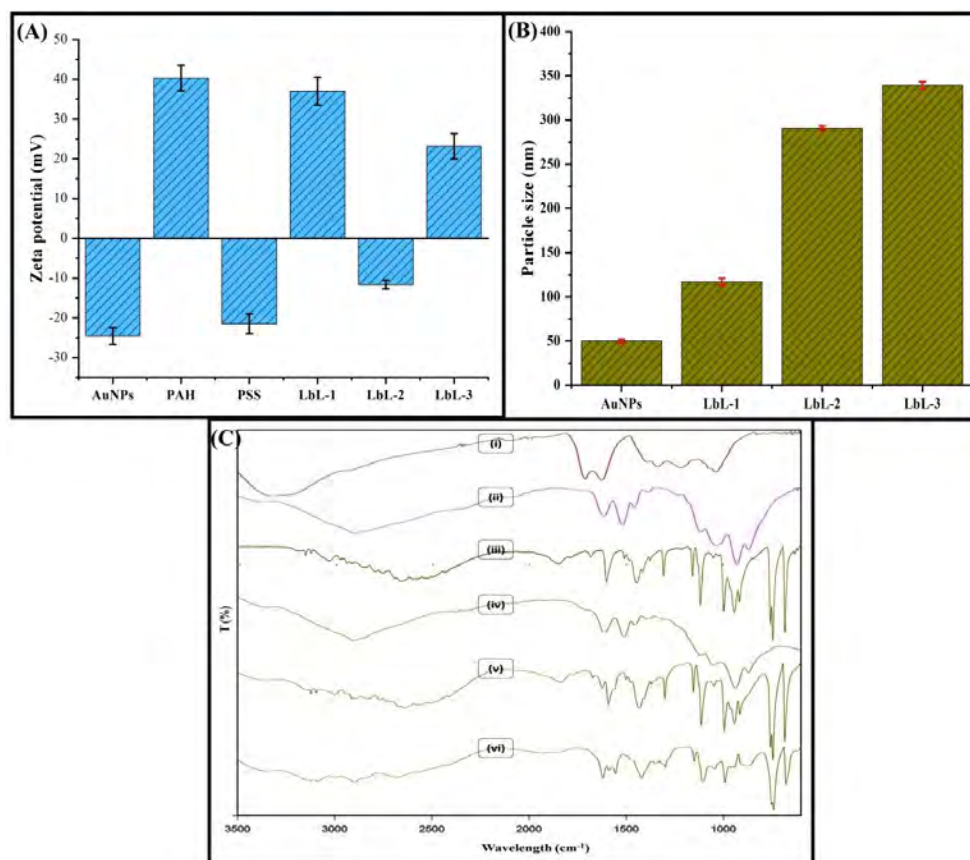


Figure 5.12: Zeta potential analysis of obtained AuNPs, PAH, PSS, AuNPs-PAH (LbL-1), AuNPs-PAH-PSS (LbL-2), and AuNPs-PAH-PSS-PAH (LbL-3). (B) Particle size analysis green obtained AuNPs, AuNPs-PAH (LbL-1), AuNPs-PAH-PSS (LbL-1), and AuNPs-PAH-PSS-PAH (LbL-1). (C) ATR FT-IR spectra of green synthesized (i) AuNPs, (ii) PAH, (iii) PSS, (iv) AuNPs-PAH, (v) AuNPs-PAH-PSS, and (vi) AuNPs-PAH-PSS-PAH.

The particle size assessment of freeze-dried AuNPs, AuNPs-PAH, AuNPs-PAH-PSS, and AuNPs-PAH-PSS-PAH is presented in **Figure 5.12.B**. In general, the particle size and PDI of lyophilized AuNPs were 50 nm and 0.30, accordingly. It verified that nanosized AuNPs were distributed throughout the solvent system. In the case of LbL assembly, the particle size and PDI of AuNPs-PAH were revealed to be 117.10 nm and 0.29, respectively, which represents the rise in the mean particle size of AuNPs following the deposition of the PAH layer. Likewise, AuNPs-PAH-PSS and AuNPs-PAH-PSS-PAH had average particle sizes of 291 nm and 339.2 nm with PDI values of 0.27 and 0.20, respectively. The enhanced mean diameter of polyelectrolyte-coated AuNPs ensured the formation of PSS and PAH layers. Ultimately, particle size analysis ensured the formation of LbL assemblies and the homogeneous dispersion of constructed nanosized LbL assemblies in a solvent system

without aggregating. After this confirmation, the freeze-dried AuNPs-PAH-PSS-PAH was validated using SEM-EDAX analysis to ensure the exact average diameter of each LbL assembly. The chemical compositions of the constructed LbL framework on the outside of green-produced AuNPs were confirmed using ATR FT-IR spectroscopy. **Figure 5.12.C** showed the ATR FT-IR spectrums of AuNPs, PAH, PSS, AuNPs-PAH, AuNPs-PAH-PSS, and AuNPs-PAH-PSS-PAH. In summary, the ATR FT-IR spectra of AuNPs displayed the peak for 'C=O' stretching vibrations at 1720 cm^{-1} , with the existence of 'C-O' verified by the peak intensity at 1315 cm^{-1} . The occurrence of NH_2 functionality (amide bond I and amide bond II) was verified by the peaks at 1590^{-1} , while 'C-H' bond stretching was confirmed by the peaks at 2832 cm^{-1} and 2914 cm^{-1} [51]. The existence of 'N-H' group vibrations is indicated by the appearance of peaks in the ATR FT-IR spectra of PAH between $3440\text{-}3415\text{ cm}^{-1}$. Peaks at $1615\text{-}1519\text{ cm}^{-1}$ were related to '-NH' asymmetric vibrations (protonated - NH_3^+), whereas the peak at 2905 cm^{-1} was ascribed to asymmetric 'C-CH₂' vibrations [29]. ATR FT-IR spectrum of PSS indicates 'C-H' stretching vibrations at 2930 cm^{-1} , whereas benzene ring vibrations (in-plane skeleton and in-plane bending vibrations) are found at 1153 cm^{-1} and 1113.12 cm^{-1} , respectively. The existence of ' SO_3^- ' (sulphonate group) in PSS was confirmed by the peak at 993.14 cm^{-1} . Overall, it ensured the presence of sulphonate functional groups in a PSS [24]. The ATR FT-IR spectra of AuNPs-PAH reveal peaks at $1619\text{-}1514\text{ cm}^{-1}$ that correspond to the '-NH' asymmetry of PAH. In the instance of the AuNPs-PAH-PSS ATR FT-IR spectrum, a peak at 992.45 cm^{-1} verified the presence of ' SO_3^- ' (sulphonate group) of PSS, whilst peaks at $1620\text{-}1593\text{ cm}^{-1}$ were associated with the '-NH' asymmetry of PAH. Similarly, the peaks at 993.50 cm^{-1} and $1625\text{-}1520\text{ cm}^{-1}$ verified the emergence of AuNPs-PAH-PSS-PAH. Overall, the peak related to PAH and PSS ensured the development of LbL assembly on surface of AuNPs [29].

5.3. Approach III

For the first time, the CS-alginate nanobioconjugate and GO carbon 2D backbone-layered affinity SPR optical biosensor was predicted to be used for exceptionally sensitive and selective BACE-1 assessment. First, green-synthesized, stable, and nanosized Pt-NPs were successfully used as plasmonic nanomaterials, whereas non-plasmonic GO nanosheets were created via the modified hummers method. The LbL assembly was then built for the first time for SPR biosensors, using cationic and anionic coating polymers 'CS' and 'SA', respectively.

5.3.1. Characterizations of green synthesized Pt-NPs

Figure 5.13.A shows the UV Vis absorption spectra of *Terminalia catappa* L. leaves extract. Here, the extract exhibited absorption peaks near about 266.5 nm and 368.5 nm that ascribed to π - π^* and n- π^* transition, respectively. **Figure 5.13.B** revealed the ATR FT-IR of *Terminalia catappa* L. leaves extract. It shows the peak at 3192.77 cm^{-1} , 2891.90 cm^{-1} -2820.28 cm^{-1} , 1706.01 cm^{-1} , 1598.64 cm^{-1} , 1317.87, and 1170.42 cm^{-1} that confirmed the overlapping of -OH/-NH₂ functional groups, C-H stretching, C=O stretching, N-H bending, C-O (carboxylic) stretching, and C-O (alcohol) stretching vibrations, respectively. **Figure 6.13.C** depicted the Zeta potential of *Terminalia catappa* L. leaves extract. It shows a negative zeta potential (- 16.05 mV) that may be because of the carboxylic functionality present in the extract. **Figure 5.13.D** disclosed the UV Vis absorption spectra with different concentrations of leaves extract of *Terminalia Catappa*. Here, the addition of different concentrations of extract offers the reduction in peak intensity of H₂PtCl₆*6H₂O. As a result, it revealed that the 4 %v/v of the extract completely reduced the platinum ions and synthesized the Pt-NPs.

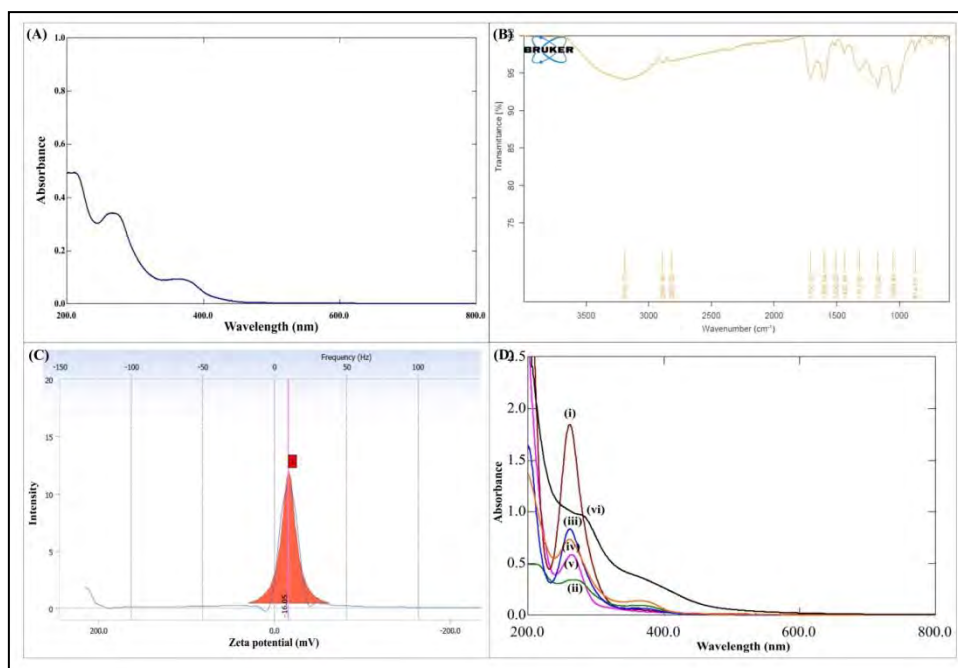


Figure 5.13.: (A) UV absorption spectra and (B) ATR FT-IR of *Terminalia catappa* L. leaves extract. (C) Zeta potential of *Terminalia catappa* L. leaves extract. (D) UV Vis absorption spectra of (i) H₂PtCl₆*6H₂O, (ii) leaves extract of *Terminalia Catappa*, green synthesized Pt-NPs with *Terminalia catappa* L. leaves extract (iii) 0.5 % v/v, (iv) 1% v/v, (v) 1.5 % v/v, and (vi) 2 % v/v.

Figure 5.14.A explained the visual changes in the color of 5 mM of H₂PtCl₆*6H₂O after the addition of leaves extract of *Terminalia Catappa*. In brief, the addition of extract into the

$\text{H}_2\text{PtCl}_6 \cdot 6\text{H}_2\text{O}$ solution turns the light yellow (Pt^{4+}) to yellowish brown (Pt^{2+}). After the completion of 5 h, the color of the mixture turns to dark yellowish-brown (Pt^0) assured the green synthesis of Pt-NPs.[58, 59] The UV Vis absorption spectrum (**Figure 5.14.B**) of $\text{H}_2\text{PtCl}_6 \cdot 6\text{H}_2\text{O}$ indicates at 261.5 nm that the Cl^- ions and Pt^{4+} ions are involved in a ligand-to-metal charge transfer (LMCT) exchange. The extract exhibited absorption peaks at 266.5 nm and 368.5 nm that ascribed to $\pi\text{-}\pi^*$ and $\text{n-}\pi^*$ transition, respectively.[59] Hence, it confirmed the several phytochemicals present extract of *Terminalia Catappa* leaves. Subsequently, an absorption band at 283 nm was seen in the UV Vis spectra of produced Pt-NPs. As well, the peak intensity of $\text{H}_2\text{PtCl}_6 \cdot 6\text{H}_2\text{O}$ was significantly lowered and shifted towards the longer wavelength with the addition of extract. It might be due to the reduction of ' Pt^{4+} ' ions to ' Pt^0 '. Here, bioactive compounds present in the extract plays the role of stabilizing and reducing agent for 'Pt' ions. As a result, it substantiated the effective green synthesis of Pt-NPs. The average particle size and PDI of the green-produced Pt-NPs were estimated to be 102.2 nm and 0.187, accordingly (**Figure 5.14.C**). As a result, it validated the assembly of nanosized Pt-NPs with homogeneous distribution in aqueous conditions adopting the green approach. The zeta potential of the Pt-NPs was determined to be -23.84 mV, indicating that the nanoparticles were stable in aqueous environments (**Figure 5.14.D**). It showed a negative zeta potential that because of the existence of a phytochemical with a negative charge that functions as a capping agent for Pt-NPs. This negative zeta potential caused electrostatic repulsion in nanoparticles, which helped to limit aggregation and hence increased the stability of Pt-NPs in aqueous conditions. ATR FT-IR analysis was used to confirm the probable biomolecules in an extract that led to the reduction and stabilization of Pt-NPs. Because of the overlapping of -OH/-NH₂ functional groups, the leaf extract of *Terminalia Catappa* exhibited a significant spike at 3192.77 cm^{-1} . Moreover, the band at 2891.90 cm^{-1} and 2820.28 cm^{-1} confirmed the occurrence of C-H stretching. The existence of C=O stretching, N-H bending, C-O (carboxylic) stretching, and C-O (alcohol) stretching vibrations were indicated by the appearance of peaks at 1706.01 cm^{-1} , 1598.64 cm^{-1} , 1317.87, and 1170.42 cm^{-1} , respectively. As an outcome, it reveals the emergence of biomolecules with carboxylic, hydroxylic, or amine functionality that can lead to the reduction of Pt^{4+} ions and develop the Pt-NPs [**Figure 5.14.E(i)**]. **Figure 5.14.E(ii)** demonstrates the change in peak intensity following the green synthesis of Pt-NPs. There are minimal variations in peak intensity following the green synthesis of Pt-NPs in this study. The existence of C=O stretching, N-H bending, C-O (carboxylic) stretching, and C-O (alcohol) stretching vibrations were indicated by the appearance of peaks at 1709.58 cm^{-1} , 1595.90 cm^{-1} , 1326.32 cm^{-1} and

1170.38 cm^{-1} , respectively. Moreover, the peaks at 2954.25 cm^{-1} and 2897.78 cm^{-1} confirmed the slight alteration of C-H stretching due to interaction with 'Pt' ions. The peak intensity at 3172.14 cm^{-1} assured the presence of -OH/-NH₂ (overlapping) stretching in green-made Pt-NPs. As well, the change in ATR FT-IR transmittance validated the production of Pt-NPs. Finally, an extract comprising phytochemicals with the aforementioned carboxy, hydroxyl, and amine functional groups can be liable for the reduction of Pt⁴⁺ into Pt⁰ and the development of stable Pt-NPs.[58, 60]

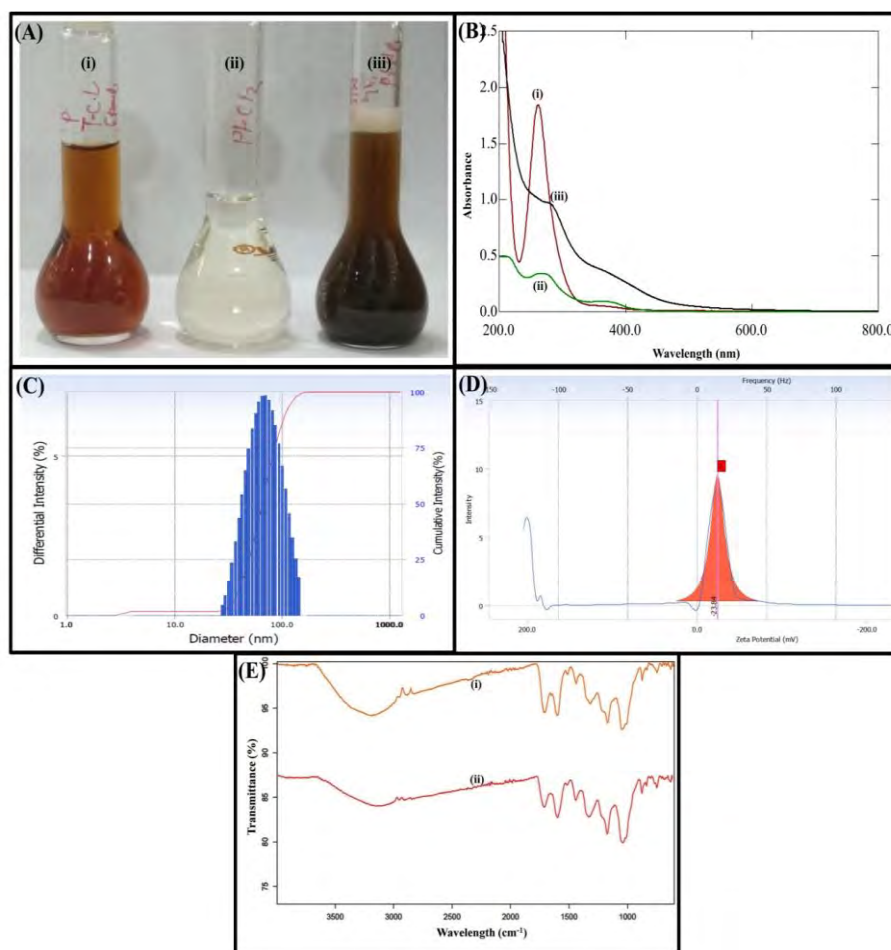


Figure 5.14: (A) Photographs of *Terminalia Catappa* leaves extract (i), platinum chloride (ii), and green synthesized Pt-NPs (iii). (B) UV Vis absorption spectrum of (i) H₂PtCl₆*6H₂O, (ii) leaves extract of *Terminalia Catappa*, and (iii) green synthesized Pt-NPs. (C) Particle size analysis of green synthesized PtNPs. (D) Zeta potential of green synthesized Pt-NPs. (E) ATR FT-IR spectrum of leaves extract of *Terminalia Catappa* (i) and green synthesized Pt-NPs (ii).

The crystalline nature of green-produced Pt-NPs was assessed using PXRD analysis (**Figure 5.15..A**). In brief, it proved the intense peak at $2\theta = 12.67^\circ, 17.97^\circ, 21.52^\circ, 25.04^\circ, 28.11^\circ, 31.77^\circ, 36.25^\circ, 42.49^\circ, 45.52^\circ, 46.46^\circ, 52.05^\circ, 58.80^\circ,$ and 65.09° that assured the synthesis

of crystalline Pt-NPs using the green method.[60] The SEM analysis demonstrated smooth surface morphology with a decent organization (**Figure 5.15.B**). In addition, it depicted several Pt-NPs forms such as rectangular, hexagonal, and cubic. Overall, SEM analysis confirmed the synthesis of Pt-NPs using the leaf extract of *Terminalia Catappa*. [61]

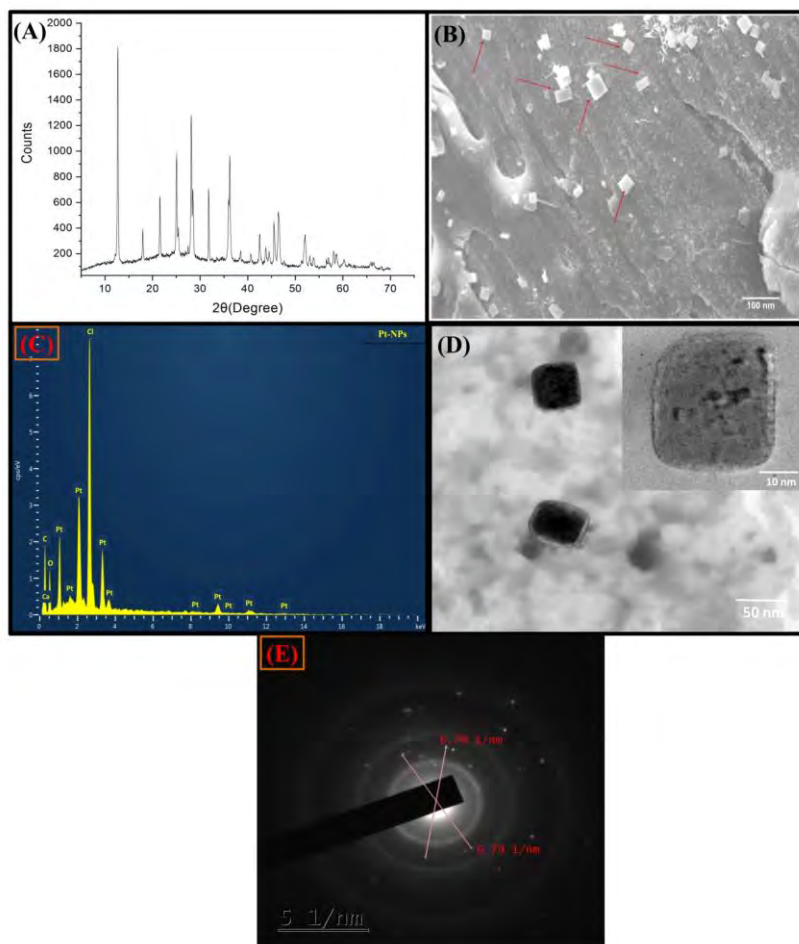


Figure 6.15: (A) Diffractogram of green synthesized Pt-NPs. (B) SEM images of green-produced Pt-NPs. (C) EDAX spectrum of green-made Pt-NPs. (D) HR-TEM images of green synthesized Pt-NPs. (E) SAED pattern of green-made Pt-NPs

The platinum (Pt^{4+}), carbon (C), and oxygen (O) % wt compositions were revealed to be 24.76 wt%, 54.25 wt%, and 16.61 wt%, respectively (**Figure 5.15.C**). In this case, the inclusion of carbon, and oxygen, guaranteed that these groups are accountable for the capping and stabilizing action in the synthesis of Pt-NPs. Besides this, the chlorine and calcium were found to be negligible (3.68 wt% and 0.7 wt%, respectively), which might be because of PtCl_2 and DDW.[62] Since the capping compounds in the extract offered electrostatic repulsion, it ensured homogeneous dispersion of nanoparticles.[63] Here, the HR-TEM images demonstrated the designed Pt-NPs in rectangular shapes (**Figure 5.15.D**). Overall, the results demonstrated the synthesis and stability of nanosized Pt-NPs without agglomeration.

The SAED pattern showed bright circular spots that confirmed the crystalline nature of Pt-NPs (**Figure 5.15.E**). Overall, HR-TEM and SAED analysis confirmed the synthesis of nanosized, uniformly distributed crystalline Pt-NPs using the green method. made Pt-NPs. The XPS survey scan spectrum of the green-produced Pt-NPs is depicted in **Figure 5.16.A**. Carbon (C1s), oxygen (O1s), nitrogen (N1s), and platinum (Pt4f) were found to be the most abundant components in green-made Pt-NPs. **Figure 5.16.B** illustrated the high-resolution deconvolution spectrum of 'Pt4f'. In this case, binding energies at 72.50 eV and 77.90 eV were attributed to $\text{Pt}^0 4f^{7/2}$ and $\text{Pt}^0 4f^{5/2}$, respectively. The characteristic peaks for 'Pt' atoms at the surface were determined to be 72.50 eV and 76.07 eV. The characteristic peaks for zerovalent 'Pt' atoms at bulk NPs were found to be 75.10 eV and 77.90 eV. The deconvolution high-resolution spectrum of 'C1s' were obtained at 283.67 eV, 284.58 eV, 285.57 eV, and 286.92 eV (**Figure 5.16.C**). It may be due to the presence of characteristic peaks of C-C, C-N, C=O, and C=C, respectively. **Figure 5.16.D** depicted the deconvolution high-resolution spectra of 'O1s', which revealed binding energies of C=O and C-O at 532.77 eV and 531.37 eV, respectively. **Figure 5.16.E** represented the high-resolution deconvolution spectrum of 'N1s'. Because of the amine functionality, the binding energy was found at 400 eV. Overall, it ensured that the resulting Pt-NPs were Pt^0 rather than Pt^{2+} or Pt^{4+} . The conversion of Pt^{4+} to Pt^0 by direct reduction of an oxidized 'Pt' species utilizing *Terminalia Catappa* leaf extract [40].

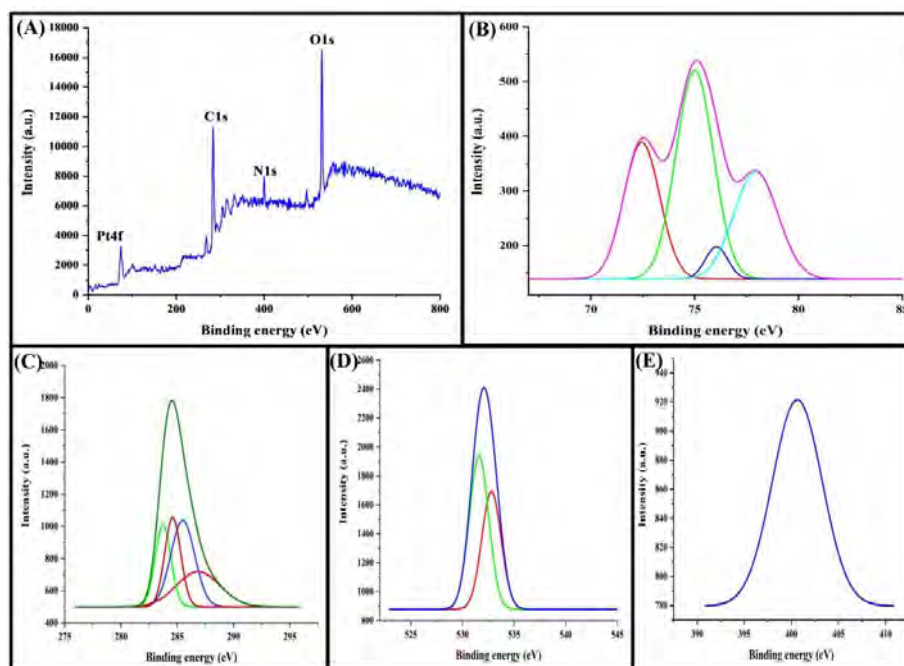


Figure 5.16: (A) XPS survey scan spectrum of green-made Pt-NPs. Deconvulated spectrum of (B) Pt4f, C1s (C), O1s (D), and N1s (E).

5.3.2. Development of CS-SA-CS@Pt-NPs LbL assembly

Figure 5.17.A displays the zeta potential of produced LbL assemblies. In summary, the zeta potential of green-prepared Pt-NPs was obtained to be -22.35 mV, indicating the stability and negative surface potential of green-manufactured nanoparticles. The 'CS' solution zeta potential was found to be + 33.92 mV whereas the SA solution zeta potential was found to be - 57.56 mV, respectively. The initial layer of 'CS' on the surface of Pt-NPs creates the CS@Pt-NPs wherein the zeta potential was found to be + 18.77 mV. It denotes amine (NH₂)-containing cationic 'CS' deposition on the top of negatively charged green-made Pt-NPs. On the contrary, the zeta potential of SA-CS@Pt-NPs was found to be -21.73 mV. Notably, the second layer of anionic 'SA' on CS@Pt-NPs displays a shift in zeta potential from positive to negative, signifying that the 'SA' layer on previously positively charged CS@Pt-NPs was successfully coated. Finally, the zeta potential of CS-SA-CS@Pt-NPs was obtained to be +31.87 mV. In conclusion, by a change in the zeta potential of Pt-NPs-based LbL assemblies with corresponding polymeric layers, the complete adsorption of 'CS' and 'SA' on the face of green-produced Pt-NPs was proven. Moreover, the zeta potentials of all assemblies were close to (+/-) 30 mV, confirming the strong aqueous stability of the intended LbL assemblies. Additionally, the occurrence of NH₂ functions on the top of the 'CS', which is an exterior layer of the CS-SA-CS@Pt-NPs assembly, contributed to the positive zeta potential. In this case, the NH₂ groups of the 'CS' play a key role in the carbodiimide-based immobilization of antibodies. The particle size and PDI of lyophilized Pt-NPs in an aqueous media were 102.2 nm and 0.18, respectively (**Figure 5.17.B**). The particle size of CS@Pt-NPs was estimated to be 165.6 nm, and the PDI value was confirmed to be 0.18. The deposition of cationic 'CS' caused a change in the size of the average hydrodynamic diameter of negatively charged Pt-NPs. Likewise, SA-CS@Pt-NPs and CS-SA-CS@Pt-NPs were determined to be 216.9 nm (PDI; 0.16) and 280.1 nm (PDI; 0.19), respectively. The shift in average particle size of CS@Pt-NPs was caused by the deposition of anionic 'SA' and subsequently cationic 'CS'.

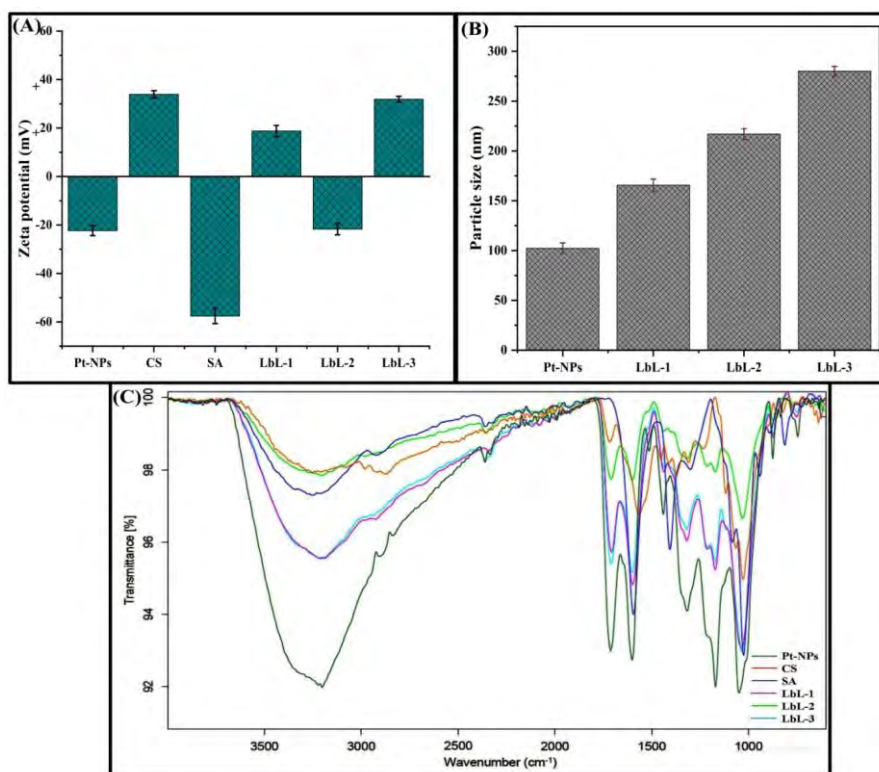


Figure 5.17: (A) Zeta potential of Pt-NPs, CS, SA, and CS@Pt-NPs, SA-CS@Pt-NPs, and CS-SA-CS@Pt-NPs. (B) Particle size analysis of Pt-NPs, CS@Pt-NPs, SA-CS@Pt-NPs, and CS-SA-CS@Pt-NPs. (C) ATR FT-IR spectrum of Pt-NPs, CS, SA, and CS@Pt-NPs, SA-CS@Pt-NPs, and CS-SA-CS@Pt-NPs.

ATR FT-IR analysis (**Figure 5.17.C**) was undertaken to verify the surface functionality of the intended LbL assemblies. The ATR FT-IR spectrum of Pt-NPs showed the existence of C=O stretching, N-H bending, C-O (carboxylic) stretching, and C-O (alcohol) stretching vibrations indicating the appearance of peaks at 1712.08 cm⁻¹, 1602.25 cm⁻¹, 1440.98 cm⁻¹ and 1170.59 cm⁻¹, respectively. Moreover, the band at 2902.27 cm⁻¹ and 2834.41 cm⁻¹ confirmed the slight alteration of C-H stretching due to interaction with ‘Pt’ ions. The peak intensity at 3205.04 cm⁻¹ assured the presence of -OH/-NH₂ (overlapping) stretching in green-made Pt-NPs. The ATR FT-IR spectrum of ‘CS’ shows the peaks at 3251.60 cm⁻¹, 3079.67 cm⁻¹, 2980.78 cm⁻¹ to 2867.08 cm⁻¹, 1716.79 cm⁻¹, 1568.01 cm⁻¹, 1372.77 cm⁻¹, and 1027.95 cm⁻¹ that assured the presence of NH₂ /OH overlapping, aromatic CH stretching, alkanes CH stretching, amide C=O, amine (-NH) bending, and C-O, respectively. The ATR FT-IR spectrum of SA demonstrated the peaks at 3251.11 cm⁻¹, 2917.55 cm⁻¹, 1593.67 cm⁻¹, 1405.31 cm⁻¹, and 1025.48 cm⁻¹ that assured the presence of OH functional group stretching, C-H stretching (alkanes), asymmetric stretching mode of -COONa groups, symmetric stretching mode of -COONa, and C-O-C stretching in glycoside bonds, respectively. In the

case of the ATR FT-IR spectrum of CS@Pt-NPs, the peaks at 3185.70 cm^{-1} , 2896.62 cm^{-1} , 1708.88 cm^{-1} , 1597.93 cm^{-1} , 1317.22 cm^{-1} , 1171.77 cm^{-1} , and 1035.72 cm^{-1} , assured the functionality of CH and Pt-NPs present in LbL assembly. In addition, the peaks present in Pt-NPs showed a reduction of % transmittance after the deposition of the cationic CS layer on the top of Pt-NPs. The ATR FT-IR peak of SA-CS@Pt-NPs displayed peaks at 3207.32 cm^{-1} , 1712.17 cm^{-1} , 1599.25 cm^{-1} , 1317.45 cm^{-1} , 1171.80 cm^{-1} , and 1032.28 cm^{-1} that ascribed the presence of SA, CS, and Pt-NPs. Here, the % transmittance of SA-CS@Pt-NPs was found to be less than the CS@Pt-NPs layer that because of SA anionic layer deposition on the surface of the CS layer. Finally, the ATR FT-IR spectrum of CS-SA-CS@Pt-NPs depicted the peaks at 3210.49 cm^{-1} , 2895 cm^{-1} , 1714.50 cm^{-1} , 1598.58 cm^{-1} , 1317.80 cm^{-1} , 1172.10 cm^{-1} , and 1034.92 cm^{-1} that are identical to the CS@Pt-NPs, and SA-CS@Pt-NPs. Here, the % transmittance of CS-SA-CS@Pt-NPs was found to be almost identical to the first CS-based CS@Pt-NPs assembly. Overall, it assured the synthesis of 'CS' and 'SA' deposited LbL assembly on the surface of green-made Pt-NPs.

The diffractogram of CS-SA-CS@Pt-NPs revealed a decline in peak intensity, which might be due to the cationic 'CS' and anionic 'SA' coating on the exterior of the Pt-NPs (**Figure 5.18.A**). As per **Figure 5.18.B**, the surface morphology of CS-SA-CS@Pt-NPs was found to be smoother than that of green synthesized Pt-NPs. It may be because of the deposition of 'CS' and 'SA'. As well, it assured the alteration dimension within the nano-size range. Overall, it confirmed the synthesis of CS-SA-CS@Pt-NPs for the immobilization of bioreceptors.

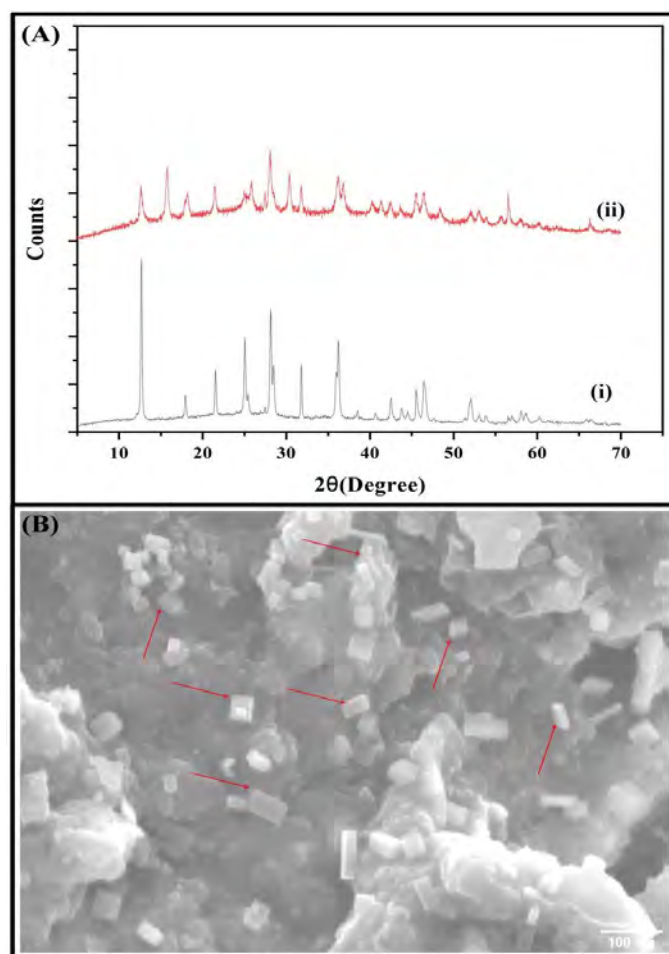


Figure 5.18: (A) Diffractogram of green synthesized Pt-NPs (i), and CS-SA-CS@Pt-NPs (ii).
(B) SEM images of CS-SA-CS@Pt-NPs.

6. Statistical Analysis

6.1. Part I

6.1.1. Detection of $A\beta_{1-42}$ using GO@AgNPs-Anti- $A\beta$ SPR biosensor

In this step, the design of high sensitive GO@AgNPs-Anti- $A\beta$ SPR biosensor was reported using GO, and LbL assembly of AgNPs-CS-PSS-CS. The immobilization of anti- $A\beta$ antibodies on the surface of AgNPs-CS-PSS-CS was achieved by mixing AgNPs-CS-PSS-CS and monoclonal anti- $A\beta$ antibodies followed by physical adsorption. It develops the bonding among amino groups of AgNPs-CS-PSS-CS containing CS and carboxyl group of anti- $A\beta$ antibody that resulted in AgNPs-CS-PSS-CS@anti- $A\beta$ conjugates. The zeta potential of AgNPs-CS-PSS-CS@anti- $A\beta$ conjugate was found to be + 29.01 mV confirming the immobilization of antibody on the surface of AgNPs-CS-PSS-CS. After that, the immobilization of the GO nanosheet on the surface of the amine-modified 'Au' coated SPR sensor chip was achieved by carbodiimide chemistry using EDC/NHS. Herein C-terminal carboxylic functional groups were activated and then condensed with a surface group of the

sensor chip. The addition of BSA after immobilization of antibody AgNPs-CS-PSS-CS@anti- $A\beta$ conjugates offers the blocking of a free surface group on the GO nanosheet. As depicted in **Figure 6.1.A** and **Figure 6.1.B**, the signal of the SPR biosensor enhanced as the concentration of $A\beta_{1-42}$ peptide raised from 2 fg/mL to 400 ng/mL. In this, SPR signal response and logarithmic value of ' $A\beta_{1-42}$ ' peptide concentration exhibited the linear relationship wherein the regression equation was found to be $Y = 30.64 * \log A\beta \text{ (fg)} + 13.38$ and regression coefficient (R^2) was found to be 0.9833 (**Figure 6.1.C**). In the case of the regression equation, 'Y' depicts the response from the SPR biosensor, and 'C' indicates the concentration of $A\beta$. Moreover, the LOD was calculated using the equation of $3SD/\text{slope}$ (SD: standard deviation, $n = 3$). As a result, the LOD was found to be $1.21 \pm 0.08 \text{ fg/mL}$. Herein, it confirmed that the application of GO and LbL assembly in GO@AgNPs-Anti- $A\beta$ SPR boosted the sensitivity towards the $A\beta$ peptide. Furthermore, it provides a wide linear range that may be because of the combined approach of non-plasmon GO, plasmonic AgNPs, LbL assembly, and affinity bioreceptors in SPR biosensors. Primarily, when GO was used as a carrier for immobilization. It is advantageous to develop maximal antibody conjugation. Surprisingly, the edge of the GO nanosheet was coarse and had a lot of oxygen functionality. Thus, it has a greater surface area and a better immobilization ability. The assembly of GO nanosheets on the surface-modified 'Au' layer of a sensor chip demonstrated good stability after washing with PBS buffer and other solvents, as evidenced by a small change in the system's resonant angle. The dense AgNPs modified by polyelectrolyte (LbL assembly) offer a fresh platform with plentiful binding sites and oriented anti- $A\beta$ immobilization. For sense, an exceptional bioconjugate strategy was preferred for sensing of $A\beta$ peptide wherein AgNPs-CS-PSS-CS@anti- $A\beta$ conjugate enlarges the mass transfer on the sensing chip surface. It helps to boost the refractive index of the fabricated sensing chip and consequently, it furnishes an amplified response signal. In addition, 'Au' coating and high mass density AgNPs-CS-PSS-CS@anti- $A\beta$ conjugate resulted in electromagnetic coupling. It offers to boost final SPR response signals that are generated from the dielectric alteration of the metal carrier after the formation of $A\beta$ peptide-anti $A\beta$ conjugate. Therefore, the concentration of AgNPs-CS-PSS-CS@anti- $A\beta$ conjugate is playing an imperative role in sensitivity enhancement. The concentration of LbL assembly was tuned in this study, wherein raising the concentration of AgNPs-CS-PSS-CS@anti- $A\beta$ conjugate to 25 $\mu\text{g /mL}$ yields rising redshifts that are proven by resonant angle. As concentration increased, there was a substantial deposition of bioconjugate, resulting in a change in resonant angle (blue shift). Therefore, 25 $\mu\text{g /mL}$ (saturation concentration) of a developed bioconjugate was preferred as

a signal enhanced in biosensing of $A\beta$ peptide. Overall, the synergistic performance of sensor components improves the sensitivity of the SPR biosensor.

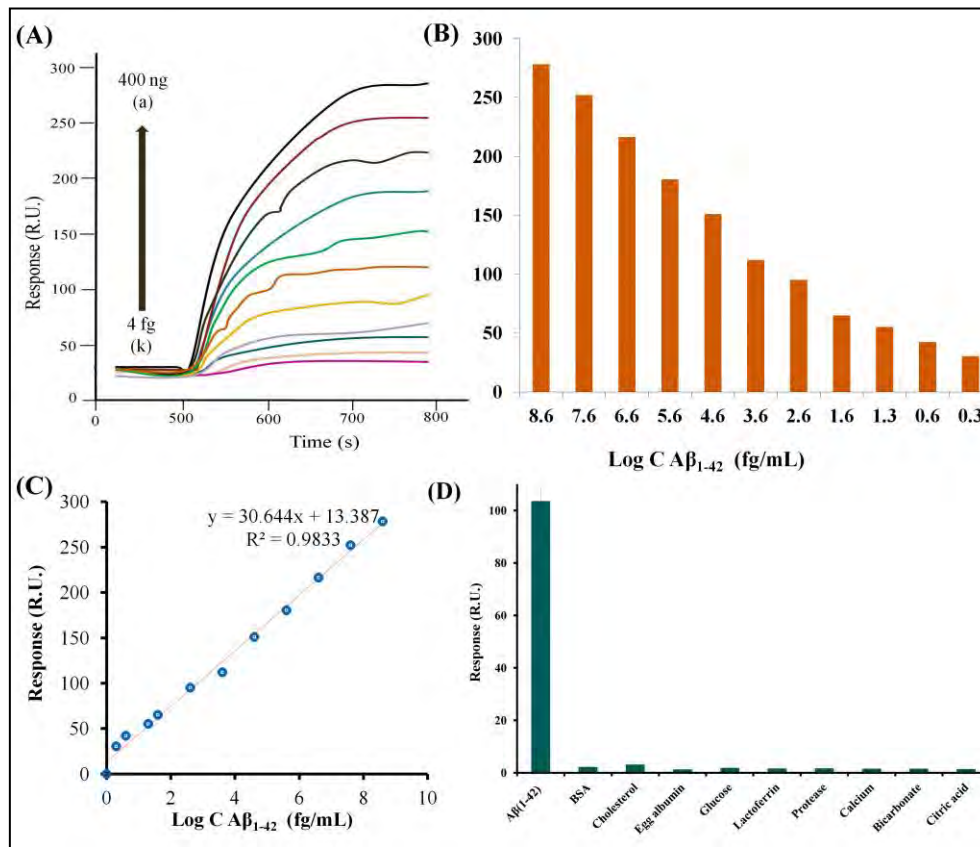


Figure 6.1: (A) Overlay of SPR sensograms and bar chart. (B) Responses showing the interaction of different concentrations of $A\beta_{1-42}$ such as 400 ng/mL, 40 ng/mL, 4 ng/mL, 400 pg/mL, 40 pg/mL, 4 pg/mL, 400 fg/mL, 40 fg/mL, 20 fg/mL, 4 fg/mL, 2 fg/mL (a to k) with immobilized with. (C) A linear relationship between SPR biosensor signal (Response) to logarithmic $A\beta_{1-42}$ concentration. (D) Selective detection of $A\beta_{1-42}$.

Finally, the analysis of $A\beta$ peptide in AD-induced animal blood, saliva, and CSF was accomplished using the GO@AgNPs-Anti- $A\beta$ SPR biosensor. At 0 days, there was no SPR signal response for samples of healthy animals' blood and saliva samples. After that, at 18 days after injection of STZ, the collected blood, saliva, and CSF samples showed 27.75 pg/mL, 8.20 fg/mL, and 89.44 pg/mL of the presence of the ' $A\beta$ ' peptide, respectively. For 21 days, blood, saliva, and CSF samples were examined using the completion of the GO@AgNPs-Anti- $A\beta$ SPR biosensor that demonstrated the significant enhancement in the SPR response unit. Herein, the CSF of AD-induced animals displayed the maximum concentration of $A\beta_{1-42}$ peptide (130.02 pg/mL) as compared to the blood (56.17 pg/mL) and saliva (69.80 fg/mL). Hence, the $A\beta$ peptide identification in AD-induced animal body fluids

using the GO@AgNPs-Anti- $A\beta$ SPR biosensor confirmed the real-time applicability of the SPR biosensor for the diagnosis of AD.

6.1.2. Anti-interference study and other analysis parameters

The selectivity of the GO@AgNPs-Anti- $A\beta$ SPR biosensors towards $A\beta_{1-42}$ peptide was measured by injecting 40 ng/mL of each interfering molecule such as proteins, enzymes metal ions, etc. The relative responses of the $A\beta_{1-42}$ peptide and other molecules over the GO@AgNPs-Anti- $A\beta$ SPR biosensors surface were measured as a response unit. As a result, the analysis confirmed that the responses assessed for $A\beta_{1-42}$ at 40 ng/mL concentrations were obtained larger as compared to the responses obtained for selected interfering substances (**Figure 6.1.D**). Interestingly, owing to affinity biotransducer (Anti- $A\beta$ antibody), the GO@AgNPs-Anti- $A\beta$ SPR biosensors furnish a high selectivity towards the $A\beta_{1-42}$ in the presence of other interfering agents. The real-time analysis of $A\beta_{1-42}$ in saliva and blood samples showed negligible interference by saliva and blood compositions. The percentage recovery of $A\beta_{1-42}$ was obtained to be 92.95 % and 98.50 % in saliva and blood samples, respectively. The % RSD was found to be 5.78 and 1.69 for spiked $A\beta_{1-42}$ in saliva and blood samples, respectively. Therefore, it confirmed that the GO@AgNPs-Anti- $A\beta$ SPR biosensor can be preferred to recognize $A\beta_{1-42}$ from real-time samples. Other important features mainly stability and reproducibility of the proposed GO@AgNPs-Anti- $A\beta$ SPR biosensor were measured. As a result, the percent RSD was 1.85 % (less than 5 %) showing that the GO@AgNPs-Anti- $A\beta$ SPR biosensor has good reproducibility. In the case of stability of GO@AgNPs-Anti- $A\beta$ SPR biosensor, % RSD was found to be 2.32 %. It indicates the acceptable stability of the GO@AgNPs-Anti- $A\beta$ SPR biosensor. In conclusion, the fabricated GO@AgNPs-Anti- $A\beta$ SPR biosensor exhibited good stability, reproducibility, high selectivity, and real-time applicability.

6.2. Part II

6.2.1. Biosensing of Tau-441 antigen

In this work, the GO@LbL-AuNPs-Anti-Tau SPR biosensor was developed employing GO nanosheets, AuNPs-PAH-PSS-PAH@Anti-Tau conjugates, and amine-functionalized Au-coated glass chip. Initially, GO nanosheets adhered to the surface of an amine-functionalized Au-coated glass chip using EDC/NHS chemistry. In this study, the increase of GO nanosheet dispersion concentration from 100 $\mu\text{g/mL}$ to 500 $\mu\text{g/mL}$ demonstrated a linear relationship with SPR response units. However, more increases in the concentration of GO proved the lack of SPR response. As a result, for the design of the predicted SPR biosensor, 500 $\mu\text{g/mL}$ of GO dispersion was considered as an optimized concentration (**Figure 6.2.A**). In this

shadow, repeat injections of optimized GO resulted in saturation, with no SPR response seen in the sensorgram. In a nutshell, it ensured that amine-functionalized sensor surface sites were completely engaged with GO nanosheets. Here, a strong connection between the activated carboxylic functionality of GO and the sensor chip's amine functional groups was established via carbodiimide chemistry. Importantly, the purpose of GO nanosheet applications in SPR biosensors was to provide a greater surface area and precise affinity that is beneficial for enhanced SPR biosensing. Moreover, the GO nanocomposite-stacking interactions, hydrogen bonding, electrostatic interaction, and especially hydrophilic affinity enhanced biomolecule sorption possibilities in SPR biosensors. Furthermore, the carboxylic functions of GO permitted the modification of the real interface features of the biosensor layer for bioreceptor adsorption via covalent banding. As a result, it aids in controlling the band gap. It also has strong biocompatibility with biomolecules.[64] Then, the AuNPs-PAH-PSS-PAH@Anti-Tau conjugate was created by combining AuNPs-PAH-PSS-PAH and an Anti-Tau rabbit monoclonal antibody. In this step, the carbodiimide chemistry was used to capture Anti-Tau rabbit monoclonal antibodies on the surface of AuNPs-PAH-PSS-PAH assemblies. Here, activated carboxylic functional groups of antibodies establish a bond with the amine functionality of AuNPs-PAH-PSS-PAH assembly.

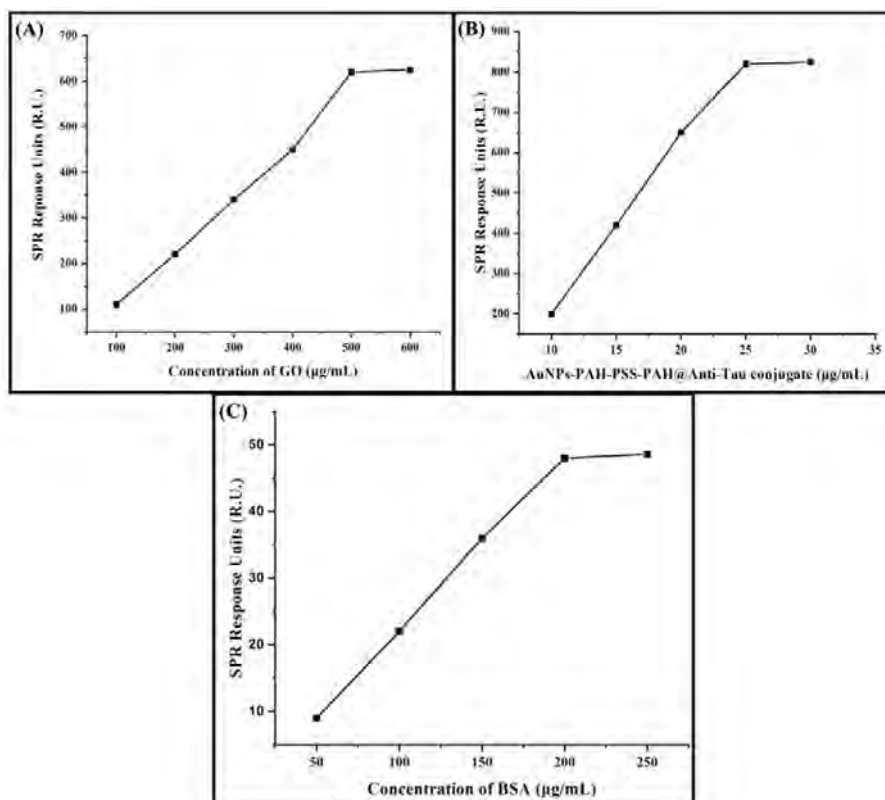


Figure 6.2: (A) Optimization of GO concentration (100 µg/mL to 600 µg/mL) for GO@LbL-AuNPs-Anti-Tau SPR biosensor construction. (B) AuNPs-PAH-PSS-PAH@Anti-Tau

conjugate concentration optimization (10 $\mu\text{g/mL}$ to 30 $\mu\text{g/mL}$). (C) BSA concentration optimization (50 $\mu\text{g/mL}$ to 250 $\mu\text{g/mL}$) as a masking agent for the development of a GO@LbL-AuNPs-Anti-Tau SPR biosensor.

As a response, the antibody and LbL assembly create a strong covalent interaction. As a corollary, it provides directed immobilization of the antibody, which aids in providing great selectivity toward the specific antigen. Furthermore, LbL assembly supplies the chemical functionality of interfacial captors, as well as regulated composition and stability. After immobilization of activated GO on the surface of the SPR sensor chip, the produced AuNPs-PAH-PSS-PAH@Anti-Tau conjugates then adhered to the outside of the activated GO nanosheet. Herein, SPR response is linearly related to the addition of 10 $\mu\text{g/mL}$ to 25 $\mu\text{g/mL}$ of prepared AuNPs-PAH-PSS-PAH@Anti-Tau conjugates (**Figure 6.2.B**). Following this validation, the optimized concentration of AuNPs-PAH-PSS-PAH@Anti-Tau conjugates (25 $\mu\text{g/mL}$) was used for the final biosensing of Tau-441 antigen. Here; it was injected in duplicates that exhibited no SPR response for the second incorporation of AuNPs-PAH-PSS-PAH@Anti-Tau conjugate. Hence, it validated the saturation of AuNPs-PAH-PSS-PAH@Anti-Tau conjugates on the face of activated GO nanosheets attached to the sensor chip surface. Interestingly, the immobilization of bioconjugates is feasible owing to the abundance of functional groups in GO, which results in rough surfaces and greater surface area. Both of these GO properties facilitated the immobilization of AuNPs-PAH-PSS-PAH@Anti-Tau conjugates in SPR biosensors. Following this step, the free group on the surface of GO was masked using BSA. In this step, the injection BSA (50 $\mu\text{g/mL}$ to 200 $\mu\text{g/mL}$) showed a slight SPR response; possibly due to the almost complete saturation of sites present in GO nanosheets by AuNPs-PAH-PSS-PAH@Anti-Tau conjugates (**Figure 6.2.C**). Further addition of BSA resulted in a no SPR response in the sensogram. As a result, the optimized concentration of BSA (200 $\mu\text{g/mL}$) was suggested for the biosensing of the Tau-441 antigen. Repeat inclusion of BSA (200 $\mu\text{g/mL}$) from the sample port in openSPR resulted in no SPR response, ensuring full masking of active carboxylic functionality. Following this validation, the detection was carried out with varied concentrations of Tau-441 antigen from fg/mL to ng/mL. **Figure 6.3.A** depicts the SPR sensorgram recording of Tau-441 antigen concentration (fg/mL) vs SPR response units (RU) using a constructed GO@LbL-AuNPs-Anti-Tau SPR biosensor. **Figure 6.3.B** showed the linear correlation wherein the SPR signal enhanced when the log concentration of Tau-441 antigen was raised from 5 fg/mL to 150

ng/mL ($R^2 = 0.997$). In this case, the SPR signal response is 'y', whereas 'x' reflects the concentration of Tau-441 antigen. Furthermore, the LOD detection was achieved to be 13.25 fg/mL based on ' $3.3\sigma/\text{slope}$ ', where standard deviation ($N = 7$) is represented by ' σ ' [$Y = 0.0726x + 0.0567$; $R^2 = 0.996$]. Hence, it assured the boost of the total sensitivity of SPR biosensors. Taken as a whole, it might be because AuNPs, LbL assembly, Au-modified glass chip, GO nanosheets, and affinity bioreceptors were used.

In summary, AuNPs comprised the high collective oscillations of their conduction electrons, which led to localized SPR. As well, AuNPs are more sensitive to changes in a system environment. In this case, linking AuNPs with L-SPR to Au films with propagating plasmons can result in a significant change in SPR reflectivity. As a result, the resonant wavelength shift rises. Furthermore, the utilization of a 2D-based GO nanosheet provides a wider surface area with high surface functionality for AuNPs-PAH-PSS-PAH@Anti-Tau immobilization. In addition, the GO promotes 'RI' by modulating surface plasmon polariton propagation. Besides, the usage of LbL assembly provides specific directions to affinity receptors whereas it increases the mass transfer on the 'Au' coated sensing exterior.

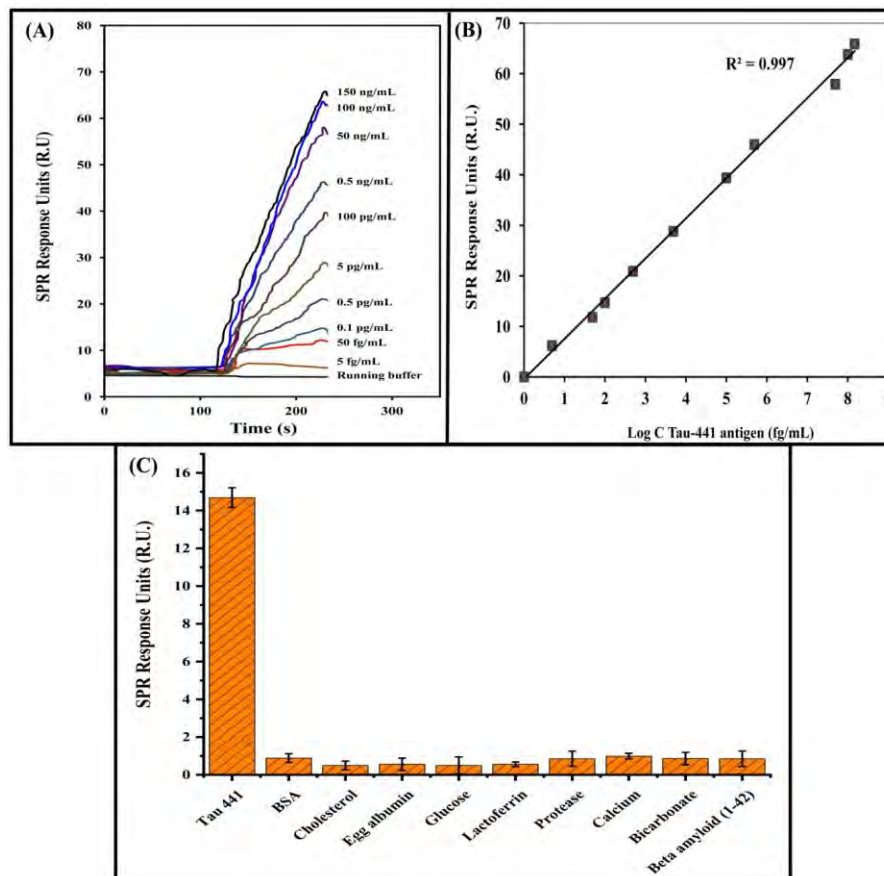


Figure 6.3: (A) SPR sensogram recording of concentration of Tau-441 antigen (5 fg/mL to 150 ng/mL) vs response (RU) using fabricated GO@LbL-AuNPs-Anti-Tau SPR biosensor.

- (B) The linear relationship between Tau-441 antigen concentrations and SPR response units.
- (C) The anti-interference potential of GO@LbL-AuNPs-Anti-Tau SPR biosensor for Tau-441 antigen in the presence of several interfering agents.

6.2.2. Selectivity, stability, and reproducibility analysis

Selectivity is one of the critical variables in biosensor technology that ensured the functioning of biosensors in the presence of numerous interfering components. In this case, the selectivity analysis for Tau-441 antigen was worked out utilizing a GO@LbL-AuNPs-Anti-Tau SPR biosensor in the existence of diverse interfering agents such as BSA, cholesterol, egg albumin, glucose, lactoferrin, protease, calcium, bicarbonate and $A\beta_{1-42}$. The selectivity aptitude of the GO@LbL-AuNPs-Anti-Tau SPR biosensor for Tau-441 antigen in the presence of other interfering molecules is demonstrated in **Figure 6.3.C**.

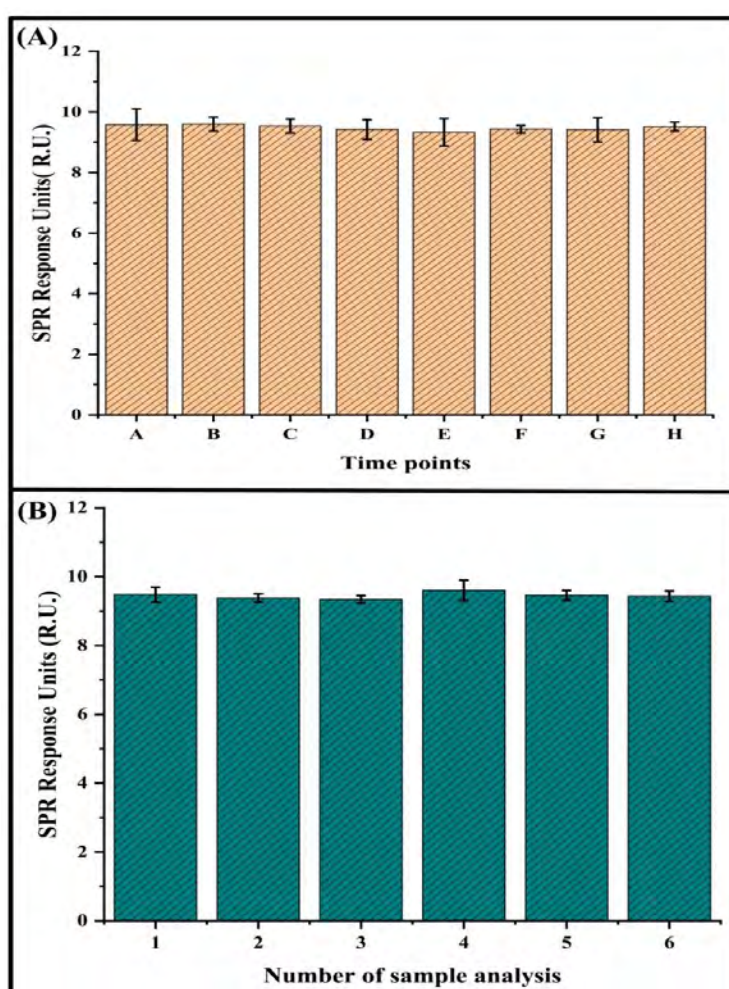


Figure 6.4: (A) Stability of the GO@LbL-AuNPs-Anti-Tau SPR biosensor for Tau-441 antigen at different time points such as 1,4,8,12,18,24,36, and 48 h. (B) Reproducibility of the GO@LbL-AuNPs-Anti-Tau SPR biosensor for Tau-441 antigen (N: 6).

In essence, the absence of Tau-441 antigen in samples suggests no SPR response, whereas the occurrence of Tau-441 antigen signifies an SPR response. In the case of interfering agents, there is no/minimal response for interfering samples BSA, cholesterol, egg albumin, glucose, lactoferrin, protease, calcium, and bicarbonate. As well, the intended SPR biosensor resulted in no SPR response after the incorporation of $A\beta_{1-42}$ from the samples port. As a result, it ensured that the suggested affinity GO@LbL-AuNPs-Anti-Tau SPR biosensor can differentiate Tau-441 antigen from other interfering agents owing to their high selectivity. Other analytical characteristics measured were the stability (N = 8) and reproducibility (N = 6) of the affinity AuNPs-PAH-PSS-PAH@Anti-Tau biosensor. **Figure 6.4.A** confirmed the stability of the GO@LbL-AuNPs-Anti-Tau SPR biosensor for Tau-441 antigen at different time points such as 1,4,8,12,18,24,36, and 48 h. **Figure 6.4.B** disclosed the reproducibility of the GO@LbL-AuNPs-Anti-Tau SPR biosensor for Tau-441 antigen (N = 6). In summary, the GO@LbL-AuNPs-Anti-Tau SPR biosensors showed a % RSD of 2.61 % (SD: 2.62) and 2.52 % (SD: 2.49) for stability and reproducibility, respectively. Here, the % RSD was found to be less than 5% which confirmed the good stability and reproducibility in an analysis of Tau-441 antigen using affinity AuNPs-PAH-PSS-PAH@Anti-Tau biosensor.

6.2.3. Spiked sample analysis

In brief, it showed a % recovery of 95.40 % and % RSD of 1.50 % for the spiked levels of Tau-441 antigen (50 fg/mL) in saliva. Similarly, blood samples showed 97.60% and % RSD for 1.47 % of Tau-441 antigen concentration (50 fg/mL). Here, % RSD was found to be less than 5% for both spiked sample analyses. Therefore, the % recovery of Tau-441 antigen in spiked samples demonstrated the potential reliability of the GO@LbL-AuNPs-Anti-Tau SPR biosensor in detecting Tau-441 antigen in clinical samples. Overall, it established the GO@LbL-AuNPs-Anti-Tau SPR biosensor's high specificity for Tau-441 antigen in complex samples.

6.2.4. Tau-441 antigen biosensing in AD-induced animals using GO@LbL-AuNPs-Anti-Tau SPR biosensor

To ensure the practicability of the GO@LbL-AuNPs-Anti-Tau SPR biosensor, the antigen Tau-441 was detected in AD-induced rats. In short, there was no SPR response found for the Tau-441 antigen on 0 days, indicating the lack of tau protein in CSF, blood, and saliva. It confirmed the healthy condition of selected animals. After 18 days of analysis, the concentration of tau protein in the blood, CSF, and saliva was determined to be 206.24 fg/mL, 590.44 fg/mL, and 147.61 fg/mL, respectively. Here, the SPR response for tau protein assured the progression of AD disease in rats. Finally, SPR response was found to be high

after 21 days when compared to the initial and 18-day studies. In concisely, the tau protein concentration in blood and saliva was 338.47 fg/mL and 264.69 fg/mL, respectively. As well, tau protein was obtained to be 1.141 pg/mL in CSF samples. Overall, the examination of clinical samples for the detection of tau protein in AD-induced rats confirmed the practical application of GO@LbL-AuNPs-Anti-Tau SPR biosensor.

6.3. Part III

6.3.1. Immunoassay of BACE-1 antigen using Anti-BACE-1-LbL@Pt-NPs-GO-SPR biosensor

The surface of an NH₂ functionalized 'Au' coated SPR biosensor was ornamented with GO nanosheets. As well, the carboxylic functionality of the GO nanosheets was triggered using carbodiimide chemistry. As a response, it aids in the formation of strong amide bonds between the sensor chip's NH₂ functionality and the activated carboxylic activity of GO nanosheets. Using EDC/NHS chemistry, the produced Anti-BACE-1@CS-SA-CS@Pt-NPs bioconjugates were immobilized on the surface of GO nanosheets. In this, BSA covered the leftover free-activated carboxylic groups of GO nanosheets. Lastly, the SPR response of the Anti-BACE-1-LbL@Pt-NPs-GO-SPR biosensor was achieved for diverse concentrations of BACE-1 to demonstrate responsiveness. It displayed sensitivity for a wide range of BACE-1 concentrations ranging from 150 ng/mL to 5 fg/mL (**Figure 6.5.A**). Surprisingly, an increase in BACE-1 concentration led to an improvement in the SPR response unit. Based on the linear regression equation ($y = 13.79x + 3.030$) and correlation coefficient ($R^2 = 0.9936$), the developed Anti-BACE-1-LbL@Pt-NPs-GO-SPR biosensor has a linear concentration range of 150 ng/mL (3.06 pM) to 5 fg/mL (0.1 aM) (**Figure 6.5.B**). The LOD was determined to be 5.63 fg/mL (0.11 aM, SD: 1.045, and slope: 0.6125), with the linear regression equation being $y = 0.6125x + 0.1886$ and the correlation coefficient being $R^2 = 0.9966$. As well, the LOQ was found to be 17.06 fg/mL (0.35 aM). Notably, the Anti-BACE-1-LbL@Pt-NPs-GO-SPR biosensor was discovered to be particularly sensitive to the lowest concentration of BACE-1 in pH 7.4 PBS. In addition, it provides a wider linear range for BACE-1 detection than previously reported electrochemical and fluorescence-based biosensors. Fascinatingly, the combined benefits of green-produced plasmonic Pt-NPs, non-plasmonic GO nanosheets, Au-coated SPR sensor chip, and affinity bioreceptor-adorned LbL assembly may justify the gain in sensitivity of SPR biosensors. Curiously, the use of Pt-NPs in SPR biosensors provide great chemical stability, dielectric constant, and reflectivity. Because of the change in the refractive index of the sensing medium, Pt-NPs exhibited remarkable responsiveness in

resonance wavelength alterations. Interestingly, both 'CS' and 'SA' have been commonly used in the biomedical field due to their biocompatibility and surface modification capabilities. Here, CS and SA were utilized to create LbL assemblies based on their electrostatic interaction. To enhance the functionality of the biosensor, the exterior layer of the CS-SA@Pt-NPs LbL assembly was coated with an amine-terminated 'CS'. This 'CS' coating provided ample sites for the immobilization of antibodies via carboxylic terminals, ensuring their orientation in a specific direction. As a benefit, the 'CS' and SA-based LbL assembly techniques offered a softer attachment surface on the solid Pt-NPs. It facilitates the direct immobilization of Anti-BACE-1 that avoids denaturation and maintains bio-functionality. This approach was also responsible to improve the surface orientation of the bioreceptors, thereby enhancing binding affinity. Additionally, coating metal nanoparticles with polyelectrolytes provided better dispersion stability in a solvent system, preventing agglomeration. Therefore, by employing the 'CS' and 'SA' mediated LbL assembly, the design of the biosensor offered improved sensitivity, selectivity, and other key factors necessary for the rapid analysis of biomarkers in a given sample. Moreover, the utilization of GO nanosheets contributed to the enhancement of SPR response. Here, GO nanosheets were primarily used for the immobilization of developed biotransducers consisting of anti-BACE-1 and Pt-NPs in large quantities. It was because of their higher surface area and abundant carboxylic surface activity of GO nanosheets. In this case, GO's carboxylic functionality promotes strong binding to proteins with amine activity as well as high biocompatibility.[65] Moreover, the addition of GO nanosheets increases the electromagnetic field, resulting in an amplified SPR response. Furthermore, the association between the amine functionality of the 'Au' coated sensor chip and the activated carboxylic functionality of GO nanosheets relates to the stability of affinity biosensors in aqueous environments, which also contributes to the improvement of SPR biosensor sensitivity. Moreover, the high bio-affinity between anti-BACE-1 and activated GO nanosheets allows for high BACE-1 detection employing SPR-based biosensors. In addition, the highly specific detection of BACE-1 antibody and antigen may minimize non-specific interaction with other system counterparts. The subsequent modification with GO immobilization aids in increasing the thickness of the 'Au' layer. As an outcome, it aids to raise the refractive index of the sensor chip's 'Au' film, so augmenting the SPR signal. Overall, the inclination for nanomaterials such as carbon-based materials and Pt-NPs can accelerate electron transfer and amplify the electric field around the SPR probe surface. As a result, combining nanostructures in SPR sensors can increase sensitivity.

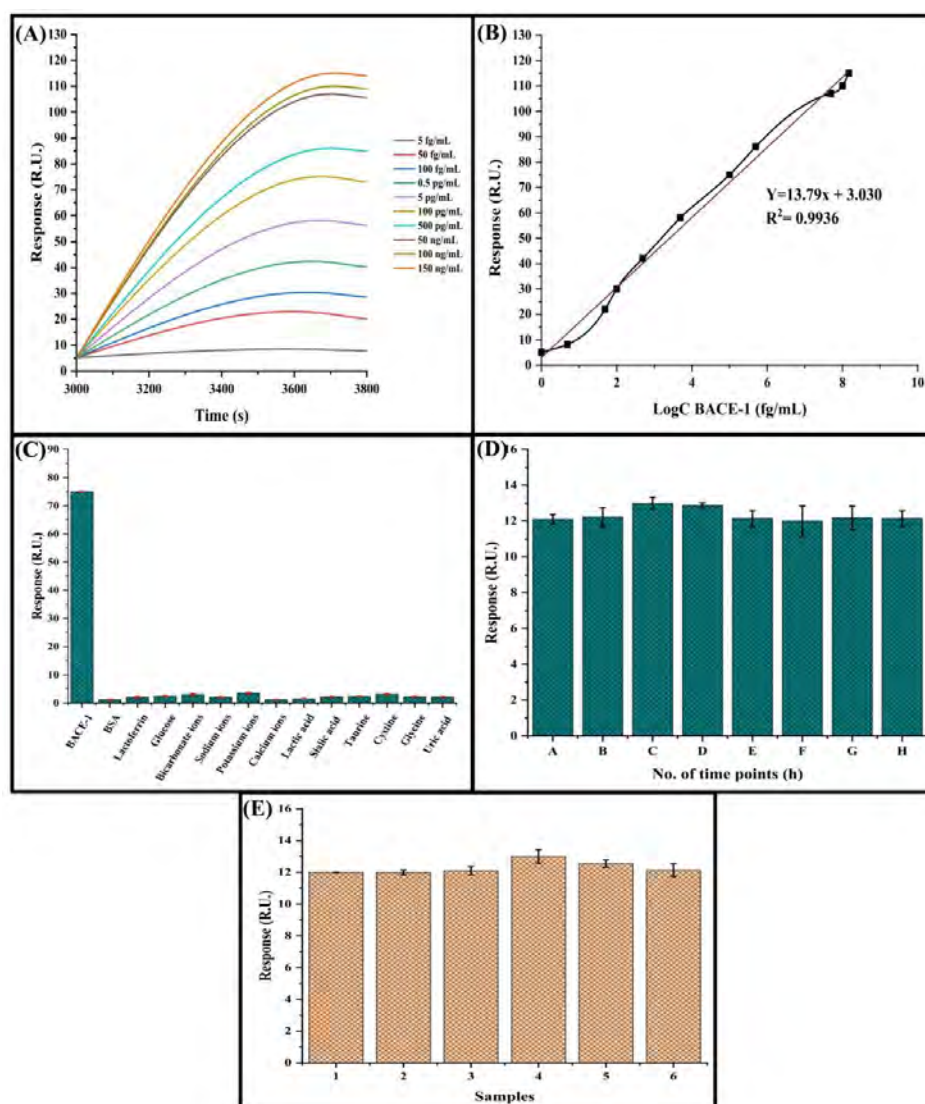


Figure 6.5: (A) SPR sensogram of BACE-1 concentration vs SPR response using fabricated Anti-BACE-1-LbL@Pt-NPs-GO-SPR biosensor for detection of BACE-1 antigen. (B) Graphical presentation of linearity involved in concentrations of BACE-1 and SPR response using Anti-BACE-1-LbL@Pt-NPs-GO-SPR biosensor. (C) Selectivity analysis of Anti-BACE-1-LbL@Pt-NPs-GO-SPR biosensor towards BACE-1 antigen. (D) Stability analysis of Anti-BACE-1-LbL@Pt-NPs-GO-SPR biosensor at different time points from A to h (1, 2, 6, 8, 12, 18, 20, and 24 h). (E) Reproducibility analysis of Anti-BACE-1-LbL@Pt-NPs-GO-SPR biosensor (N = 6).

6.3.2. Selectivity study, spiked sample, stability, and reproducibility analysis of BACE-1 protein

In this step, Anti-BACE-1-LbL@Pt-NPs-GO-SPR biosensor selectivity to BACE-1 antigen was revealed utilizing various interfering agents. **Figure 6.5.C** depicts the SPR response for each interfering agent individually, as well as a known concentration of BACE-1 and a

combination of interfering agents and BACE-1. At this point, the SPR responses for interfering agents were revealed less significant than the BACE-1. Furthermore, the SPR response from BACE-1 in a mixture of interfering agents proves the high selectivity of the Anti-BACE-1-LbL@Pt-NPs-GO-SPR biosensor towards BACE-1 in the presence of several interfering substances with minimum influence. As a result, the Anti-BACE-1-LbL@Pt-NPs-GO-SPR biosensor developed demonstrated remarkable selectivity for BACE-1 antigen in a complex sample. In summary, the recovery rate of BACE-1 in saliva samples was found to be 97.44 %, respectively. In this case, the % RSD was determined to be 1.10 % (% RSD < 5, SD: 0.163), respectively. Similarly, the recovery rate for BACE-1 in blood-spiked samples was found to be 95.48 %, respectively. In this, the % RSD was determined to be 3.86 % (% RSD < 5, SD: 0.572), respectively. As a result, the good selectivity of envisaged Anti-BACE-1-LbL@Pt-NPs-GO-SPR biosensors for BACE-1 in complicated clinical samples was established. It also supports that the Anti-BACE-1-LbL@Pt-NPs-GO-SPR biosensor may be utilized to capture BACE-1 in clinical samples. **Figure 6.5.D** explained the stability of Anti-BACE-1-LbL@Pt-NPs-GO-SPR biosensors at different time points. Consequently, it exhibited a % RSD of 3.14 %, indicating that the biosensor was stable (% RSD < 5, SD: 3.11) under testing circumstances for up to 24 h. Moreover, the developed Anti-BACE-1-LbL@Pt-NPs-GO-SPR biosensor was assessed for reproducibility utilizing a BACE-1 concentration of 20 fg/mL and their signal response. **Figure 6.5.E** illustrates the reproducibility of the proposed developed Anti-BACE-1-LbL@Pt-NPs-GO-SPR biosensor. The % RSD recorded was 3.27 % (% RSD < 5, SD: 3.23), proving the reproducibility of the Anti-BACE-1-LbL@Pt-NPs-GO-SPR biosensor. Essentially, the Anti-BACE-1-LbL@Pt-NPs-GO-SPR biosensor was found to be stable and reproducible for detecting BACE-1 antigen.

7. Discussion

Alzheimer's disease (AD), along with its associated clinical conditions like Parkinson's disease dementia, has brought about the exploration of potential diagnostic avenues focused on identifying beta-amyloid1-42 ($A\beta$ 1-42). Unfortunately, existing techniques for detecting the core biomarker $A\beta$ 1-42 in Alzheimer's disease are plagued by issues of poor sensitivity and selectivity. In response, we have developed a novel surface plasmon resonance (SPR) biosensor utilizing a layer-by-layer (LbL) assembly approach, incorporating graphene oxide (GO) surface-decorated chitosan (CS), which addresses these challenges and offers highly sensitive and selective $A\beta$ 1-42 recognition. In our approach, we began by synthesizing stable

nanosized silver nanoparticles (AgNPs) using an environmentally friendly method. Graphene oxide (GO) was then derived from graphite flakes using a modified version of the well-established Hummers method. The LbL assembly was designed using CS and polystyrene sulphonate (PSS) to create a layer on the AgNPs surface (AgNPs-CS-PSS-CS). Subsequently, anti-A β antibodies were immobilized on this assembly (AgNPs-CS-PSS-CS@anti-A β). The amine functionality of CS provided numerous sites for the immobilization of anti-A β antibodies, ensuring specific targeting, high selectivity, and optimal antibody immobilization. The biosensor fabrication process involved immobilizing the synthesized GO onto a gold-coated sensor chip with an amine modification, using carbodiimide chemistry. This was followed by the immobilization of AgNPs-CS-PSS-CS@anti-A β on the activated GO surface. The unique attributes of the LbL assembly contributed to enhanced selectivity towards A β peptide. The utilization of an affinity biotransducer featuring a combination of plasmonic and non-plasmonic nanomaterials further boosted sensitivity and selectivity. As a result, we achieved a linearity range of 2 fg/mL to 400 ng/mL and a limit of detection (LOD) of 1.21 fg/mL for A β 1-42 antigens. Furthermore, our designed SPR biosensor was put to the test in analyzing A β 1-42 in rats induced with Alzheimer's disease, validating its real-time applicability. In conclusion, the GO surface-decorated AgNPs-CS-PSS-CS@anti-A β -mediated SPR biosensor introduces a new and innovative approach for remarkably sensitive and selective A β detection.

Furthermore, the objective of this study is to develop a straightforward, label-free, rapid, highly sensitive, and selective 2D carbon backbone graphene oxide (GO) patterned surface plasmon resonance (SPR) mediated affinity biosensor for monitoring Tau-441. The process began with the creation of non-plasmonic nanosized GO using a modified Hummers method, while green-synthesized gold nanoparticles (AuNPs) underwent a layer-by-layer (LbL) design involving anionic and cationic polyelectrolytes. Rigorous spectroscopic assessments were performed to validate the successful synthesis of GO, AuNPs, and the LbL assembly. Subsequently, the Anti-Tau rabbit antibody was immobilized onto the designed LbL assembly through carbodiimide chemistry. The constructed affinity GO@LbL-AuNPs-Anti-Tau SPR biosensor underwent a series of analyses, including sensitivity, selectivity, stability, repeatability, and spiked sample assessments. The results exhibited a wide concentration range of 150 ng/mL to 5 fg/mL and an impressively low detection limit of 13.25 fg/mL. The exceptional sensitivity of this SPR biosensor is attributed to the synergistic effect of plasmonic AuNPs and non-plasmonic GO. Notably, the biosensor demonstrated remarkable selectivity for Tau-441 even in the presence of interfering substances, likely due to the

effective immobilization of the Anti-Tau rabbit on the LbL assembly surface. Moreover, the biosensor exhibited high stability and repeatability across measurements. The practical utility of the GO@LbL-AuNPs-Anti-Tau SPR biosensor was confirmed through analyses of spiked samples and samples from animals induced with Alzheimer's disease (AD). These assessments validated the biosensor's reliability and its potential for Tau-441 detection. In conclusion, the developed GO@LbL-AuNPs-Anti-Tau SPR biosensor presents a sensitive, selective, stable, label-free, rapid, and minimally invasive alternative for diagnosing Alzheimer's disease. The biosensor's capabilities and performance suggest its potential as a valuable tool in future AD diagnostics.

Chitosan (CS) and sodium alginates (SA) have emerged as promising materials for the development of layer-by-layer (LbL) assemblies in pharmaceutical dosage form design due to their versatile properties. Recently, the utilization of unique LbL assemblies in biosensor development has led to enhanced performance in detecting target analytes. Beta (β)-site amyloid precursor protein-cleaving enzyme 1 (BACE-1) stands as a critical biomarker for Alzheimer's disease (AD) and necessitates sensitive and selective identification for early-stage diagnosis. In this study, a novel approach was employed to create CS-SA-platinum nanoparticles (Pt-NPs) LbL-based nanobioconjugate, which was then applied to a carbon backbone-layered affinity surface plasmon resonance (Anti-BACE-1-LbL@Pt-NPs-GO-SPR) biosensor for highly sensitive and selective BACE-1 detection. Initially, the LbL nanobioconjugate was synthesized by incorporating cationic 'CS' and anionic 'SA' onto the surface of green-synthesized Pt-NPs. The amino groups of 'CS' provided a favorable platform for immobilizing anti-BACE-1, preserving the bio-functionality of the bioreceptors and ensuring specific orientation. Additionally, synthesized graphene oxide (GO), known for its advantageous properties in biosensors, was selected as the non-plasmonic nanomaterial. The resulting biosensor exhibited a low limit of detection (LOD) of 5.63 fg/mL and a wide linear detection range spanning from 5 fg/mL to 150 ng/mL for BACE-1. Notably, the biosensor demonstrated remarkable selectivity and real-time analysis capability in spiked samples, showcasing its practical applicability for BACE-1 detection in complex specimens. Consequently, the utilization of antibody-immobilized CS-SA-coated Pt-NPs nanobioconjugate on the GO surface offered several advantages, particularly exceptional sensitivity and superb specificity. Overall, the biosensor, which featured CS and SA-coated Pt-NPs bioconjugate decorated on GO layers, holds immense potential for highly sensitive, selective, rapid, and label-free BACE-1 detection in clinical samples.

8. Impact of the research in the advancement of knowledge or benefit to mankind

Currently, the prevalence of Alzheimer's disease is on the rise, particularly in the growing aging population. Unfortunately, Alzheimer's remains incurable and poses a significant challenge due to our limited understanding of the disease. According to the World Health Organization, there are currently over 55 million individuals worldwide living with Alzheimer's disease. Notably, the Alzheimer's Association's annual report indicated that the COVID-19 pandemic led to a 17% increase in Alzheimer's and dementia-related deaths globally in 2020. Moreover, Alzheimer's Disease International (ADI) reports that more than 41 million people with dementia worldwide remain undiagnosed. In India, accurate and comprehensive reports on Alzheimer's and its impact are lacking. Available information mainly covers prevalence, distribution, risk factors, treatments, and diagnosis of the disease. Various hospitals and agencies have published data indicating that over 4 million Indians are afflicted by Alzheimer's, a concerning and substantial health issue. Projections suggest that the number of dementia and Alzheimer's patients in India may reach around 7.5 million by 2030. Notably, economic studies have predicted a three-fold increase in dementia and Alzheimer's-related expenditures in India, potentially reaching INR 147 billion by 2030. Alzheimer's disease progresses slowly and gradually worsens over the years, affecting multiple areas of the brain. This progression leads to severe complications such as malnutrition, dehydration, restlessness, depression, infections, agitation, and bowel problems. Despite the advancements in medical research and healthcare facilities, a definitive diagnosis platform and cure for Alzheimer's remain elusive. Limited research groups in India are dedicated to Alzheimer's diagnosis, despite its severity. Physicians, often aided by specialists such as neurologists, neuropsychologists, geriatricians, and geriatric psychiatrists, employ a range of tests and technologies to aid in diagnosis. These include analyzing medical history, conducting physical examinations, and utilizing techniques like computerized tomography, magnetic resonance imaging, and positron emission tomography. However, the effectiveness of these methods is still a subject of ongoing research. Existing diagnostic options are often costly for patients and lack guaranteed accuracy in Alzheimer's diagnosis. This situation not only affects Alzheimer's patients but also places financial strain on their families. Direct expenses, including doctor fees and medical costs, can significantly impact a family's economic well-being, which has broader implications for India's developing economy. Thus, addressing these challenges highlights the need for a reliable and early-stage Alzheimer's detection platform that can enhance patients' quality of life and economic conditions. Despite medical advancements, there are currently no established methods to prevent or cure

Alzheimer's disease at its early stages. Given the gradual and prolonged progression of the disease, urgent efforts are required to develop novel therapeutic approaches that effectively delay its advancement. Additionally, the increased life expectancy due to improved global health over the past century has contributed to a higher prevalence of Alzheimer's disease. This underscores the importance of developing new point-of-care diagnosis and prevention strategies. Unfortunately, one of the major challenges in Alzheimer's disease management is late diagnosis. Therefore, specific and dependable approaches are urgently needed to either prevent or delay the progression of the disease.

Taking into account the aforementioned information about Alzheimer's disease in India, we have developed a socioeconomically viable and effective diagnostic tool for the early detection of Alzheimer's. Alzheimer's disease (AD) is a prominent neurological disorder characterized by progressive brain cell degeneration, resulting in memory loss, cognitive decline, and eventually dementia. Furthermore, AD involves a multifaceted pathway, leading to molecular changes as the disease progresses. Despite various diagnostic techniques, conventional methods often lack sensitivity and specificity in detecting AD biomarkers. However, recent advancements in recognizing AD biomarkers using bioconjugates and receptor-based approaches have shown promise in enhancing sensitivity and selectivity at the molecular level. Unfortunately, techniques employed for detecting core AD biomarkers such as beta-amyloid1-42 ($A\beta$ 1-42), Tau-441, and Beta (β)-site amyloid precursor protein-cleaving enzyme 1 (BACE-1) suffer from issues of poor sensitivity and selectivity. To address these challenges, we adopted three distinct approaches: In the first approach, we designed a surface plasmon resonance (SPR) biosensor using a layer-by-layer (LbL) assembly of graphene oxide (GO) and chitosan (CS) for the highly sensitive and selective recognition of $A\beta$ 1-42. The amine functionality of CS facilitated the immobilization of anti- $A\beta$ antibodies, offering specific direction, high selectivity, and optimal antibody attachment. The LbL assembly's unique features improved selectivity toward the $A\beta$ 1-42 peptide. By utilizing a combination of plasmonic and non-plasmonic nanomaterials as an affinity biotransducer, we enhanced sensitivity and selectivity. This resulted in a linear detection range of 2 fg/mL to 400 ng/mL for $A\beta$ 1-42 antigens, with a limit of detection (LOD) of 1.21 fg/mL. The application of the designed SPR biosensor was validated by analyzing $A\beta$ 1-42 levels in Alzheimer's disease-induced rats. In the second approach, we developed a simple, label-free, and highly sensitive two-dimensional (2D) carbon-based SPR biosensor for monitoring Tau-441. Non-plasmonic nanosized graphene oxide (GO) was synthesized using a modified Hummers method, and gold nanoparticles (AuNPs) were synthesized via a green route. These materials were then

integrated into an LbL design using anionic and cationic polyelectrolytes. The resulting biosensor demonstrated a wide concentration range (150 ng/mL to 5 fg/mL) and an impressively low LOD of 13.25 fg/mL. The exceptional sensitivity of this biosensor was attributed to the combination of plasmonic AuNPs and non-plasmonic GO. The presence of interfering molecules did not compromise the selectivity for Tau-441 due to effective immobilization of Anti-Tau rabbit on the LbL assembly surface. In the third approach, we employed chitosan (CS) and sodium alginates (SA) to create an LbL assembly, utilizing platinum nanoparticles (Pt-NPs) as a nanobioconjugate to enhance sensitivity and selectivity in BACE-1 detection. This biosensor achieved a LOD of 5.63 fg/mL and a broad linear range (5 fg/mL to 150 ng/mL). Real-time analyses of spiked samples further validated its practical utility in complex scenarios. The inclusion of antibody-immobilized CS-SA coated Pt-NPs nanobioconjugate on the GO surface offered advantages like extreme sensitivity and exceptional specificity. In conclusion, the LbL assembly-decorated GO layered SPR biosensors we have developed offer highly sensitive, selective, rapid, and label-free detection of A β 1-42, Tau 441, and BACE-1. These approaches hold promise for advancing Alzheimer's disease diagnosis and management, potentially making a significant impact on early-stage detection and patient outcomes.

In the future, we anticipate that the innovative LbL-based SPR biosensor concept, characterized by its high sensitivity, stability, reproducibility, selectivity, label-free operation, and rapid response, will serve as a competitive alternative for quantifying A β 1-42, Tau 441, and BACE-1 in clinical samples. Furthermore, this biosensor has the potential to be valuable not only for diagnosing clinical dementia but also for detecting dementia associated with Parkinson's disease. We are looking forward to the practical implementation of the described SPR-assisted biosensor for the identification of A β 1-42 in clinical samples. Based on our findings, we hold the hopeful expectation that the SPR biosensor chip we have developed will offer a safe and practical solution for the early detection of Alzheimer's disease. Essentially, our proposed SPR biosensor provides a non-invasive, user-friendly, cost-effective, label-free, rapid, highly sensitive, and remarkably selective means of diagnosing Alzheimer's at an early stage. To the best of our knowledge, this represents a pioneering global effort in employing such an innovative technique for the early diagnosis of Alzheimer's disease. We believe that our work will instill confidence among fellow researchers and clinicians that this SPR biosensor has the potential to significantly enhance the quality of life for patients while alleviating their economic burdens. In essence, the

proposed GO-based SPR biosensor signifies a modest stride toward addressing the challenges posed by Alzheimer's disease.

8. Literature references

- [1] S. Nangare, P. Patil, Nanoarchitected bioconjugates and bioreceptors mediated surface plasmon resonance biosensor for in vitro diagnosis of Alzheimer's disease: Development and future prospects, *Critical Reviews in Analytical Chemistry* 52(5) (2022) 1139-1169.
- [2] M. Yang, X. Yi, J. Wang, F. Zhou, Electroanalytical and surface plasmon resonance sensors for detection of breast cancer and Alzheimer's disease biomarkers in cells and body fluids, *Analyst* 139(8) (2014) 1814-1825.
- [3] S. Nangare, P. Patil, Prevalence, distribution, treatment, and modern methods for in vitro diagnosis of Alzheimer's disease in India: Challenges and future prospective, *Thai Journal of Pharmaceutical Sciences* 46(2) (2022).
- [4] X. Zuo, H. Dai, H. Zhang, J. Liu, S. Ma, X. Chen, A peptide-WS 2 nanosheet based biosensing platform for determination of β -secretase and screening of its inhibitors, *Analyst* 143(19) (2018) 4585-4591.
- [5] F. Qu, M. Yang, A. Rasooly, Dual signal amplification electrochemical biosensor for monitoring the activity and inhibition of the Alzheimer's related protease β -secretase, *Analytical chemistry* 88(21) (2016) 10559-10565.
- [6] M.L. Hemming, J.E. Elias, S.P. Gygi, D.J. Selkoe, Identification of β -secretase (BACE1) substrates using quantitative proteomics, *PloS one* 4(12) (2009) e8477.
- [7] S. Ucci, P. Cicatiello, S. Spaziani, A. Cusano, Development of custom Surface Plasmon Resonance Au biosensor for liver cancer biomarker detection, *Results in Optics* 5 (2021) 100193.
- [8] S. Nangare, P. Patil, Chitosan mediated layer-by-layer assembly based graphene oxide decorated surface plasmon resonance biosensor for highly sensitive detection of β -amyloid, *International Journal of Biological Macromolecules* 214 (2022) 568-582.
- [9] A. Rezabakhsh, R. Rahbarghazi, F. Fathi, Surface plasmon resonance biosensors for detection of Alzheimer's biomarkers; an effective step in early and accurate diagnosis, *Biosensors and Bioelectronics* 167 (2020) 112511.
- [10] S.N. Nangare, P.O. Patil, Affinity-based nanoarchitected biotransducer for sensitivity enhancement of surface plasmon resonance sensors for in vitro diagnosis: a review, *ACS Biomaterials Science & Engineering* 7(1) (2020) 2-30.
- [11] J. Dey, A. Roberts, S. Mahari, S. Gandhi, P.P. Tripathi, Electrochemical detection of Alzheimer's disease biomarker, β -secretase enzyme (BACE1), with one-step synthesized reduced graphene oxide, *Frontiers in Bioengineering and Biotechnology* 10 (2022).
- [12] J. Zhang, Y. Sun, B. Xu, H. Zhang, Y. Gao, H. Zhang, D. Song, A novel surface plasmon resonance biosensor based on graphene oxide decorated with gold nanorod-antibody conjugates for determination of transferrin, *Biosensors and Bioelectronics* 45 (2013) 230-236.
- [13] Q. Wang, J.-Y. Jing, B.-T. Wang, Highly sensitive SPR biosensor based on graphene oxide and staphylococcal protein a co-modified TFBG for human IgG detection, *IEEE Transactions on Instrumentation and Measurement* 68(9) (2018) 3350-3357.
- [14] N.-F. Chiu, T.-Y. Huang, H.-C. Lai, K.-C. Liu, Graphene oxide-based SPR biosensor chip for immunoassay applications, *Nanoscale Research Letters* 9(1) (2014) 1-7.

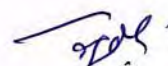
- [15] H. Vahed, E. Ghazanfari, Sensitivity enhancement of a nanocomposite-based fiber optics sensor with platinum nanoparticles, *Optica Applicata* 49(1) (2019).
- [16] S. Zeng, K.-T. Yong, I. Roy, X.-Q. Dinh, X. Yu, F. Luan, A review on functionalized gold nanoparticles for biosensing applications, *Plasmonics* 6(3) (2011) 491-506.
- [17] S. Nangare, P. Patil, Nanoarchitected bioconjugates and bioreceptors mediated surface plasmon resonance biosensor for in vitro diagnosis of Alzheimer's disease: Development and future prospects, *Critical Reviews in Analytical Chemistry* (2020) 1-31.
- [18] M.M. Barsan, C.M. Brett, Recent advances in layer-by-layer strategies for biosensors incorporating metal nanoparticles, *TrAC Trends in Analytical Chemistry* 79 (2016) 286-296.
- [19] W. Wu, X. Yu, J. Wu, T. Wu, Y. Fan, W. Chen, M. Zhao, H. Wu, X. Li, S. Ding, Surface plasmon resonance imaging-based biosensor for multiplex and ultrasensitive detection of NSCLC-associated exosomal miRNAs using DNA programmed heterostructure of Au-on-Ag, *Biosensors and Bioelectronics* 175 (2021) 112835.
- [20] R. Antiochia, P. Bollella, G. Favero, F. Mazzei, Nanotechnology-based surface plasmon resonance affinity biosensors for in vitro diagnostics, *International journal of analytical chemistry* 2016 (2016).
- [21] K. Shah, N.K. Sharma, V. Sajal, Simulation of LSPR based fiber optic sensor utilizing layer of platinum nanoparticles, *Optik* 154 (2018) 530-537.
- [22] B. Masereel, M. Dinguizli, C. Bouzin, N. Moniotte, O. Feron, B. Gallez, T. Vander Borgh, C. Michiels, S. Lucas, Antibody immobilization on gold nanoparticles coated layer-by-layer with polyelectrolytes, *Journal of Nanoparticle Research* 13 (2011) 1573-1580.
- [23] B. Snopok, Y.G. Goltsov, E. Kostyukevich, L. Matkovskaja, Y.M. Shirshov, E. Venger, Self-assembled multilayer superstructures as immobilization support for bioreceptors, *Sensors and Actuators B: Chemical* 95(1-3) (2003) 336-343.
- [24] L.H. Chen, X.M. Ang, C.C. Chan, M. Shailender, B. Neu, W.C. Wong, P. Zu, K.C. Leong, Layer-by-layer (chitosan/polystyrene sulfonate) membrane-based Fabry-Perot interferometric fiber optic biosensor, *IEEE Journal of Selected Topics in Quantum Electronics* 18(4) (2012) 1457-1464.
- [25] W. Suginta, P. Khunkaewla, A. Schulte, Electrochemical biosensor applications of polysaccharides chitin and chitosan, *Chemical reviews* 113(7) (2013) 5458-5479.
- [26] X. Yang, M. Zhang, Z. Chen, Y. Bu, X. Gao, Y. Sui, Y. Yu, Sodium alginate micelle-encapsulating zinc phthalocyanine dye-sensitized photoelectrochemical biosensor with CdS as the photoelectric material for Hg²⁺ detection, *ACS Applied Materials & Interfaces* 13(14) (2021) 16828-16836.
- [27] S. Amirthalingam, J. Rangasamy, Chitosan-based biosensor fabrication and biosensing applications, *Chitosan for Biomaterials III: Structure-Property Relationships* (2021) 233-255.
- [28] B. Masereel, M. Dinguizli, C. Bouzin, N. Moniotte, O. Feron, B. Gallez, T. Vander Borgh, C. Michiels, S. Lucas, Antibody immobilization on gold nanoparticles coated layer-by-layer with polyelectrolytes, *Journal of Nanoparticle Research* 13(4) (2011) 1573-1580.
- [29] Z. Zhao, Q. Li, J. Gong, Z. Li, J. Zhang, A poly (allylamine hydrochloride)/poly (styrene sulfonate) microcapsule-coated cotton fabric for stimulus-responsive textiles, *RSC advances* 10(30) (2020) 17731-17738.

- [30] S. Nangare, S. Landge, A. Patil, R. Tade, P. Deshmukh, P. Patil, Green synthesis of Fe-doped Ag-loaded reduced graphene oxide ternary nanocomposite for efficient photocatalytic degradation of toxic dyes, *Advances in Natural Sciences: Nanoscience and Nanotechnology* 12(3) (2021) 035004.
- [31] A.L. Ferreira, L.F. de Lima, A.S. Moraes, R.J. Rubira, C.J. Constantino, F.L. Leite, A.O. Delgado-Silva, M. Ferreira, Development of a novel biosensor for creatine kinase (CK-MB) using surface plasmon resonance (SPR), *Applied Surface Science* 554 (2021) 149565.
- [32] Q. Wu, N. Li, Y. Wang, Y. Xu, S. Wei, J. Wu, G. Jia, X. Fang, F. Chen, X. Cui, A 2D transition metal carbide MXene-based SPR biosensor for ultrasensitive carcinoembryonic antigen detection, *Biosensors and Bioelectronics* 144 (2019) 111697.
- [33] Y. Wang, Y. Wang, F. Wang, H. Chi, G. Zhao, Y. Zhang, T. Li, Q. Wei, Electrochemical aptasensor based on gold modified thiol graphene as sensing platform and gold-palladium modified zirconium metal-organic frameworks nanozyme as signal enhancer for ultrasensitive detection of mercury ions, *Journal of Colloid and Interface Science* 606 (2022) 510-517.
- [34] D.D. Borhade, S.N. Nangare, D.A. Patil, P.O. Patil, G.S. Patil, G.B. Patil, Preparation of pirfenidone loaded chitosan-polyvinyl alcohol-graphene oxide-based scaffold: Spectroscopical characterizations and antibacterial activity, *Journal of Drug Delivery Science and Technology* 82 (2023) 104325.
- [35] G. Suriyakala, S. Sathiyaraj, R. Babujanathanam, K.M. Alarjani, D.S. Hussein, R.A. Rasheed, K. Kanimozhi, Green synthesis of gold nanoparticles using *Jatropha integerrima* Jacq. flower extract and their antibacterial activity, *Journal of King Saud University-Science* 34(3) (2022) 101830.
- [36] T.P. Patil, A.A. Vibhute, S.L. Patil, T.D. Dongale, A.P. Tiwari, Green synthesis of gold nanoparticles via *Capsicum annum* fruit extract: Characterization, antiangiogenic, antioxidant and anti-inflammatory activities, *Applied Surface Science Advances* 13 (2023) 100372.
- [37] N.-F. Chiu, T.-L. Lin, C.-T. Kuo, Highly sensitive carboxyl-graphene oxide-based surface plasmon resonance immunosensor for the detection of lung cancer for cytokeratin 19 biomarker in human plasma, *Sensors and Actuators B: Chemical* 265 (2018) 264-272.
- [38] Z. Lou, J. Wan, X. Zhang, H. Zhang, X. Zhou, S. Cheng, N. Gu, Quick and sensitive SPR detection of prion disease-associated isoform (PrP^{Sc}) based on its self-assembling behavior on bare gold film and specific interactions with aptamer-graphene oxide (AGO), *Colloids and Surfaces B: Biointerfaces* 157 (2017) 31-39.
- [39] S. Nangare, S. Baviskar, A. Patil, P. Patil, Design of "Turn-Off" Fluorescent Nanoprobe for Highly Sensitive Detection of Uric Acid using Green Synthesized Nitrogen-Doped Graphene Quantum Dots, *Acta Chimica Slovenica* 69(2) (2022) 437-447.
- [40] A.S. Eltaweil, M. Fawzy, M. Hosny, E.M. Abd El-Monaem, T.M. Tamer, A.M. Omer, Green synthesis of platinum nanoparticles using *Atriplex halimus* leaves for potential antimicrobial, antioxidant, and catalytic applications, *Arabian Journal of Chemistry* 15(1) (2022) 103517.
- [41] T.A. Powar, A.A. Hajare, R. Jarag, S. Nangare, Development and Evaluation of Lyophilized Methotrexate Nanosuspension using Quality by Design Approach, *Acta Chimica Slovenica* 68(4) (2021) 861-881.
- [42] J.-S. Park, C.-M. Lee, K.-Y. Lee, A surface plasmon resonance biosensor for detecting *Pseudomonas aeruginosa* cells with self-assembled chitosan-alginate multilayers, *Talanta* 72(2) (2007) 859-862.

- [43] B. Çakıroğlu, A.B. Çiğil, A. Ogan, M.V. Kahraman, S. Demir, Covalent immobilization of acetylcholinesterase on a novel polyacrylic acid-based nanofiber membrane, *Engineering in Life Sciences* 18(4) (2018) 254-262.
- [44] P.O. Patil, S.N. Nangare, P.P. Patil, A.G. Patil, D.R. Patil, R.S. Tade, A.M. Patil, P.K. Deshmukh, S.B. Bari, Fabrication of N-Doped Graphene@ TiO₂ Nanocomposites for Its Adsorption and Absorbing Performance with Facile Recycling, *Nano Biomed. Eng* 13(2) (2021) 179-190.
- [45] F.T. Johra, J.-W. Lee, W.-G. Jung, Facile and safe graphene preparation on solution based platform, *Journal of Industrial and Engineering Chemistry* 20(5) (2014) 2883-2887.
- [46] S.N. Nangare, P.O. Patil, Green Synthesis of Silver Nanoparticles: An Eco-Friendly Approach, *Nano Biomedicine & Engineering* 12(4) (2020).
- [47] R. Chuah, S.C. Gopinath, P. Anbu, M. Salimi, A.R.W. Yaakub, T. Lakshmipriya, Synthesis and characterization of reduced graphene oxide using the aqueous extract of *Eclipta prostrata*, *3 Biotech* 10(8) (2020) 1-10.
- [48] R. Kannan, W. Stirk, J. Van Staden, Synthesis of silver nanoparticles using the seaweed *Codium capitatum* PC Silva (Chlorophyceae), *South African Journal of Botany* 86 (2013) 1-4.
- [49] K.K. Bharadwaj, B. Rabha, S. Pati, B.K. Choudhury, T. Sarkar, S.K. Gogoi, N. Kakati, D. Baishya, Z.A. Kari, H.A. Edinur, Green Synthesis of Silver Nanoparticles Using *Diospyros malabarica* Fruit Extract and Assessments of Their Antimicrobial, Anticancer and Catalytic Reduction of 4-Nitrophenol (4-NP), *Nanomaterials* 11(8) (2021) 1999.
- [50] M. Singh, R. Kalaivani, S. Manikandan, N. Sangeetha, A. Kumaraguru, Facile green synthesis of variable metallic gold nanoparticle using *Padina gymnospora*, a brown marine macroalga, *Applied Nanoscience* 3(2) (2013) 145-151.
- [51] D. Philip, Green synthesis of gold and silver nanoparticles using *Hibiscus rosa sinensis*, *Physica E: Low-Dimensional Systems and Nanostructures* 42(5) (2010) 1417-1424.
- [52] S. Satpathy, A. Patra, B. Ahirwar, M.D. Hussain, Process optimization for green synthesis of gold nanoparticles mediated by extract of *Hygrophila spinosa* T. Anders and their biological applications, *Physica E: Low-dimensional Systems and Nanostructures* 121 (2020) 113830.
- [53] K. Xin Lee, K. Shameli, M. Miyake, N. Kuwano, N.B. Bt Ahmad Khairudin, S.E. Bt Mohamad, Y.P. Yew, Green Synthesis of Gold Nanoparticles Using Aqueous Extract of *Garcinia mangostana* Fruit Peels, *Journal of Nanomaterials* 2016 (2016) 1-7.
- [54] M. Noruzi, D. Zare, K. Khoshnevisan, D. Davoodi, Rapid green synthesis of gold nanoparticles using *Rosa hybrida* petal extract at room temperature, *Spectrochimica Acta Part A: Molecular and Biomolecular Spectroscopy* 79(5) (2011) 1461-1465.
- [55] S. Vijayakumar, R. Vinayagam, M.A.V. Anand, K. Venkatachalam, K. Saravanakumar, M.-H. Wang, K. Gothandam, E. David, Green synthesis of gold nanoparticle using *Eclipta alba* and its antidiabetic activities through regulation of Bcl-2 expression in pancreatic cell line, *Journal of Drug Delivery Science and Technology* 58 (2020) 101786.
- [56] Q. Ding, Z. Kang, X. He, M. Wang, M. Lin, H. Lin, D.-P. Yang, Eggshell membrane-templated gold nanoparticles as a flexible SERS substrate for detection of thiabendazole, *Microchimica Acta* 186 (2019) 1-9.

- [57] A.-N.D. Egueh, B. Lakard, P. Fievet, S. Lakard, C. Buron, Charge properties of membranes modified by multilayer polyelectrolyte adsorption, *Journal of colloid and interface science* 344(1) (2010) 221-227.
- [58] A. Thirumurugan, P. Aswitha, C. Kiruthika, S. Nagarajan, A.N. Christy, Green synthesis of platinum nanoparticles using *Azadirachta indica*—An eco-friendly approach, *Materials Letters* 170 (2016) 175-178.
- [59] A. Olajire, G. Adeyeye, R. Yusuf, *Alchornea laxiflora* bark extract assisted green synthesis of platinum nanoparticles for oxidative desulphurization of model oil, *Journal of Cluster Science* 28 (2017) 1565-1578.
- [60] R. Venu, T. Ramulu, S. Anandakumar, V. Rani, C. Kim, Bio-directed synthesis of platinum nanoparticles using aqueous honey solutions and their catalytic applications, *Colloids and Surfaces A: Physicochemical and Engineering Aspects* 384(1-3) (2011) 733-738.
- [61] U. Jeyapaul, M.J. Kala, A.J. Bosco, P. Piruthiviraj, M. Easuraja, An eco-friendly approach for synthesis of platinum nanoparticles using leaf extracts of *Jatropha gossypifolia* and *Jatropha glandulifera* and its antibacterial activity, *Oriental Journal of Chemistry* 34(2) (2018) 783.
- [62] K. Tahir, S. Nazir, A. Ahmad, B. Li, A.U. Khan, Z.U.H. Khan, F.U. Khan, Q.U. Khan, A. Khan, A.U. Rahman, Facile and green synthesis of phytochemicals capped platinum nanoparticles and in vitro their superior antibacterial activity, *Journal of Photochemistry and Photobiology B: Biology* 166 (2017) 246-251.
- [63] Y. Zhang, S. Cheng, H. Jia, J. Zhou, J. Xi, J. Wang, X. Chen, L. Wu, Green synthesis of platinum nanoparticles by *Nymphaea tetragona* flower extract and their skin lightening, antiaging effects, *Arabian Journal of Chemistry* 16(1) (2023) 104391.
- [64] N.-F. Chiu, C.-T. Kuo, T.-L. Lin, C.-C. Chang, C.-Y. Chen, Ultra-high sensitivity of the non-immunological affinity of graphene oxide-peptide-based surface plasmon resonance biosensors to detect human chorionic gonadotropin, *Biosensors and Bioelectronics* 94 (2017) 351-357.
- [65] N.-F. Chiu, S.-Y. Fan, C.-D. Yang, T.-Y. Huang, Carboxyl-functionalized graphene oxide composites as SPR biosensors with enhanced sensitivity for immunoaffinity detection, *Biosensors and Bioelectronics* 89 (2017) 370-376.





Mr. Sopan Namdev Nangare



Chitosan mediated layer-by-layer assembly based graphene oxide decorated surface plasmon resonance biosensor for highly sensitive detection of β -amyloid

Sopan Nangare, Pravin Patil *

Department of Pharmaceutical Chemistry, H. R. Patel Institute of Pharmaceutical Education and Research, Shirpur-425405, Dist: Dhule, MS, India

ARTICLE INFO

Keywords:

Alzheimer's disease
Beta-amyloid
Chitosan
Layer-by-layer assembly
Surface plasmon resonance
Graphene oxide, silver nanoparticles

ABSTRACT

Alzheimer's disease (AD), and its consequent effect primarily clinical dementia, Parkinson's disease dementia, etc. currently bring potential avenues for diagnosis centered on identification of beta-amyloid₁₋₄₂ ($A\beta_{1-42}$). Unfortunately, techniques engaged in AD core biomarker ($A\beta_{1-42}$) detection are majorly suffering from poor sensitivity and selectivity. Thus, we fabricated graphene oxide (GO) surface decorated chitosan (CS) mediated layer-by-layer (LbL) assembly based surface plasmon resonance (SPR) biosensor for highly sensitive and selective recognition of $A\beta_{1-42}$. Briefly, silver nanoparticles (AgNPs) and GO synthesis were achieved through a greener approach. LbL assembly was designed using CS and polystyrene sulphonate (PSS) on surface of AgNPs (AgNPs-CS-PSS-CS) and then antibodies of $A\beta$ (anti- $A\beta$) were fixed on LbL assembly (AgNPs-CS-PSS-CS@anti- $A\beta$). Herein, amine functionality of CS offers a plethora of sites for anti- $A\beta$ antibody immobilization that gives specific direction, high selectivity, and an adequate amount of antibody immobilization. For fabrication, synthesized GO was immobilized on an amine-modified gold-coated sensor chip via carbodiimide chemistry followed by AgNPs-CS-PSS-CS@anti- $A\beta$ immobilization on an activated GO surface. Inimitable features of LbL assembly showed improved selectivity towards $A\beta$ peptide whereas utilization of affinity biotransducer with a combination of plasmonic and non-plasmonic nanomaterial improved sensitivity and selectivity. Consequently, linearity range and limit of detection (LOD) of $A\beta_{1-42}$ antigens were found to be 2 fg/mL to 400 ng/mL and 1.21 fg/mL, respectively. Moreover, analysis of $A\beta_{1-42}$ in AD-induced rats confirmed the real-time-applicability of the designed SPR biosensor. Hence, GO surface decorated AgNPs-CS-PSS-CS@anti- $A\beta$ mediated SPR biosensor would provide a novel approach for exceptionally sensitive and selective $A\beta$ detection.

1. Introduction

Alzheimer's disease (AD) is a progressive, and irreversible neurodegenerative disease [1]. Subsequently, continuous progress in AD results in clinical dementia [2]. Importantly, AD is defined biologically by the presence of β -amyloid ($A\beta$) plaques and tau-containing neurofibrillary tangles in the brain [3]. It causes amnesic cognitive impairment in the prototypical form and non-amnesic cognitive impairment in the less common variants [3,4]. Literature divulged that AD is perhaps the leading prevalent form of dementia among individuals over the age of 65. It affects approximately 5 million individuals in the United States (US). As the population ages, the number of AD cases in the US is expected to climb to 16 million by 2050 [5]. Conventional diagnostic methods including imaging, laboratory analysis, examination, and

initial history of the patient have been preferred to diagnose AD [5,6]. Such methods are suffering from plenteous demerits including less detection accuracy, extremely expensive, time-consuming, etc. Moreover, there is no promising treatment existed for the management of AD whereas symptomatic treatment can endow with a short period of relief. As a result, there is necessary to establish a newish solution to diagnose AD and clinical dementia at an early stage, which can contribute to the improvement of individual life [6,7].

Merely on AD phenotype, it is complicated to determine the fundamental disease process concerned in AD. Herein, assorted biomarkers might be of considerable assistance in expediting the early recognition of AD [8]. As per literature, biomarkers are quantitative signals that are expressed within a certain stage of the ailment. It renders them essential for both diagnosis and tracking therapy response [9]. In the case of AD,

* Corresponding author.

E-mail address: rxpatilpravin@yahoo.co.in (P. Patil).

<https://doi.org/10.1016/j.ijbiomac.2022.06.129>

Received 3 February 2022; Received in revised form 24 May 2022; Accepted 18 June 2022

Available online 23 June 2022

0141-8130/© 2022 Published by Elsevier B.V.



Poly(allylamine) coated layer-by-layer assembly decorated 2D carbon backbone for highly sensitive and selective detection of Tau-441 using surface plasmon resonance biosensor

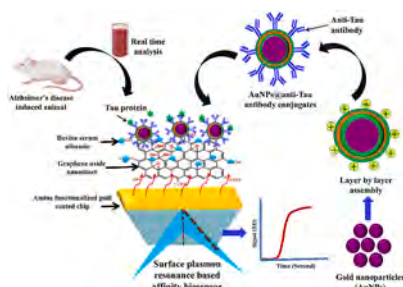
Sopan Nangare, Pravin Patil^{*}

Department of Pharmaceutical Chemistry, H. R. Patel Institute of Pharmaceutical Education and Research, Shirpur, 425405, Dhule, MS, India

HIGHLIGHTS

- The first-time layer-by-layer (LbL) approach was preferred for selective and sensitive recognition of Tau-441 antigen.
- Antibody immobilization on poly(allylamine) coated gold nanoparticles (AuNPs) LbL assembly gives affinity biotransducer.
- Graphene oxide (GO) layered surface plasmon resonance (SPR) biosensor provides detection limit up to femto-gram level.
- Spiked sample and preclinical studies assured the feasibility of GO@LbL-Au NPs-Anti-Tau SPR biosensor for Tau-441 sensing.
- Report on label-free, highly sensitive, and selective detection of Tau-441 using GO@LbL-AuNPs-Anti-Tau SPR biosensor.

GRAPHICAL ABSTRACT



ARTICLE INFO

Handling Editor: Dr. J.P. Landers

Keywords:

Tau protein
Alzheimer's disease
2D carbon backbone
Surface plasmon resonance
LbL assembly
Gold nanoparticles

ABSTRACT

The determination of clinically significant amounts of tau protein in bodily fluids is a major problem in Alzheimer's disease (AD) diagnosis. As a result, the present work aims to develop a simple, label-free, fast, highly sensitive, and selective 2D carbon backbone graphene oxide (GO) patterned surface plasmon resonance (SPR) mediated affinity biosensor for Tau-441 monitoring. Initially, non-plasmonic nanosized GO was made using a modified Hummers' method, whereas green synthesized gold nanoparticles (AuNPs) were subjected to a layer-by-layer (LbL) design employing anionic and cationic polyelectrolytes. Several spectroscopical evaluations were carried out to ensure the synthesis of GO, AuNPs, and LbL assembly. Following that, the Anti-Tau rabbit antibody was immobilized on the designed LbL assembly using carbodiimide chemistry, and various studies such as sensitivity, selectivity, stability, repeatability, spiked sample analysis, etc., were conducted using the constructed affinity GO@LbL-AuNPs-Anti-Tau SPR biosensor. As an output, it shows a broad concentration range and a very low detection limit of 150 ng/mL to 5 fg/mL and 13.25 fg/mL, respectively. The remarkable sensitivity of this SPR biosensor represents the merits of a combination of plasmonic AuNPs and a non-plasmonic GO.

^{*} Corresponding author. Department of Pharmaceutical Chemistry, H. R. Patel Institute of Pharmaceutical Education and Research, Shirpur, 425405, Dhule, MS, India.

E-mail address: rxpatilpravin@yahoo.co.in (P. Patil).

<https://doi.org/10.1016/j.aca.2023.341474>

Received 15 May 2023; Accepted 2 June 2023

Available online 3 June 2023

0003-2670/© 2023 Elsevier B.V. All rights reserved.



Platinum-alginate-chitosan nanobioconjugate decorated carbon backbone layered biosensor for highly sensitive and selective detection of BACE-1

Sopan Nangare, Pravin Patil^{*}

Department of Pharmaceutical Chemistry, H. R. Patel Institute of Pharmaceutical Education and Research, Shirpur 425405, Dist: Dhule (MS), India

ARTICLE INFO

Keywords:

β -Secretase
Chitosan
Platinum nanoparticles
Surface plasmon resonance
Alzheimer's disease
Sodium alginate
Layer-by-layer assembly

ABSTRACT

Chitosan (CS) and sodium alginates (SA) have been revealed for the design of layer-by-layer (LbL) assembly to develop pharmaceutical dosage forms owing to their versatile characteristics. Recently, the preference for unique LbL assemblies in biosensor development has offered the modified performance for detection interest analyte. Beta (β)-site amyloid precursor protein-cleaving enzyme 1 (BACE-1) is a pivotal biomarker of Alzheimer's disease (AD) and demands high sensitivity and selective identification for the early-stage diagnosis. In this work, CS-SA-platinum nanoparticles (Pt-NPs) LbL-based nanobioconjugate decorated carbon backbone-layered affinity surface plasmon resonance (Anti-BACE-1-LbL@Pt-NPs-GO-SPR) biosensor was designed for extremely sensitive and selective sensing of BACE-1. Primarily, LbL nanobioconjugate was synthesized by integrating cationic 'CS' and anionic 'SA' on the face of green-made Pt-NPs. Here, the amines of 'CS' offers a softer surface for anti-BACE-1 immobilization that leads to maintaining the bio-functionality of bioreceptors, provides the specific orientation for bioreceptors, etc. As well, the synthesized graphene oxide (GO, 2D carbon backbone) was preferred as non-plasmonic nanomaterials due to their plenty of merits in biosensors. Here, the designed biosensor provides a low detection limit (LOD) of 5.63 fg/mL and a wide linear range from 5 fg/mL to 150 ng/mL. Moreover, selectivity and real-time analyses in spiked samples exhibited their practical usefulness in complex specimens for BACE-1 detection. Hence, the decorating of antibody-immobilized CS-SA coated Pt-NPs nanobioconjugate on the face of GO has various benefits mainly extremely sensitive and superb specificity. Overall, CS and SA coated Pt-NPs bioconjugate decorated GO layered SPR biosensors can provide highly sensitive, selectivity, rapid, label-free, etc. detection of BACE-1 in clinical samples.

1. Introduction

Alzheimer's disease (AD) is a long-term, severe, irreversible, and progressing neurodegenerative health concern [1]. Since its inception, there is a tremendous demand for sensitive and specific assessment of biomarkers of particular ailments to reach an earlier diagnosis [2]. Therefore, numerous strategies for the prognosis and diagnosis of AD have been presented to date [3]. Herein, several AD biomarkers have been documented for diagnosis of AD in clinical samples mainly beta-amyloid ($A\beta$), tau protein, lactoferrin, β -Site amyloid precursor protein-cleaving enzyme 1 (BACE1), etc. [1]. Herein, BACE-1 (also referred to as Beta-secretase 1) is a critical biomarker for the timely identification of AD [4]. In recent times, it has been detected using fluorescence-based biosensors [5], electrochemical biosensors [6], quantitative proteomics [7], enzyme-linked immunosorbent assay (ELISA) [6], etc. Notwithstanding these reports on BACE-1 and other AD

biomarkers, the rapid and direct assessment of AD biomarkers in supplied clinical samples at clinically meaningful amounts remains the key rate-restricting hurdle for AD and other neurodegenerative illnesses. Since its inception, the plasmonic biosensor has offered remarkable characteristics as diagnostics for biomarker detection [8]. In the case of plasmonic biosensors, surface plasmon resonance (SPR) is a cutting-edge optical biosensor technique that detects analytes with high speed, higher sensitivity, selectivity, label free, etc. [9]. Importantly, the SPR-based technique permits the label-free identification of extremely minute amounts of a target with great accuracy and efficiency [10]. Unfortunately, to the best of our knowledge reports on the detection of BACE-1 using SPR-based biosensors are less explored.

Graphene-based carbon backbone nanostructures such as 2D non-plasmonic graphene oxide (GO) have been disclosed for the construction of upgraded SPR biosensors. Herein, SPR shifts are made possible by their optical properties [11]. Moreover, it has a large surface area,

^{*} Corresponding author.

E-mail address: rxpatilpravin@yahoo.co.in (P. Patil).

<https://doi.org/10.1016/j.ijbiomac.2023.126224>

Received 21 May 2023; Received in revised form 3 July 2023; Accepted 6 August 2023

Available online 8 August 2023

0141-8130/© 2023 Elsevier B.V. All rights reserved.